# High performance photo detection based on ultrathin semiconductor membrane

by

Zhenyang Xia

A dissertation submitted in partial fulfillment of

the requirements for the degree of

Doctor of Philosophy

(Electrical and Computer Engineering)

at the

UNIVERSITY OF WISCONSIN-MADISON

2019

Date of final oral defense: Aug 16, 2019

The dissertation is approved by the following members of the Final Oral Committee:

Zhenqiang Ma, Professor, Electrical and Computer Engineering
Zongfu Yu, Associate Professor, Electrical and Computer Engineering
Mikhail A. Kats, Associate Professor, Electrical and Computer Engineering
Jennifer Choy, Assistant Professor, Engineering Physics

# Abstract

Miniaturization of optoelectronic devices offers tremendous performance gain. As the volume of photoactive material decreases, optoelectronic performance improves, including the operation speed, the signal-to-noise ratio, and the internal quantum efficiency. Over the past decades, researchers have managed to reduce the volume of photoactive materials in solar cells and photodetectors by orders of magnitude. For example, from the very beginning, the thickness of the solar cells is around 300 μm. Up to now, the most recent thin film based solar cell is developed to just around 5 μm, while the efficiency keeps the same. The method to reduce the volume of the semiconductor materials could be grinding, chemical etching or thin film lift-off by stress defoliation. Up to now, the thin film lift-off by stress defoliation is among one of the most famous method, since the material substrate can be recycled after the thin film lift-off. By using the thin film lift-off method, materials less than 100 nm thick can be obtained, this ultrathin semiconductor material holds great promise for developing high operation speed, mechanically flexible yet still high detection efficiency photon detection devices.

However, two issues arise when one continues to thin down the photoactive layers to the nanometer scale (for example, <100 nm). First, light-matter interaction becomes weak, resulting in incomplete photon absorption and low quantum efficiency. Simple calculation can show 100 nm silicon thin film absorption over the near-infrared spectrum (from 700 nm to 1000 nm) is less than 5%. Second, it is difficult to obtain

ultrathin materials with single-crystalline quality. The thin film lift-off using stress defoliation cannot be easily applied to ultrathin semiconductor materials since it is too fragile under stress. This work introduces a method to overcome these two challenges simultaneously. It uses conventional bulk semiconductor wafers, such as Si, Ge, and GaAs, to realize single-crystalline films on foreign substrates that are designed for enhanced light-matter interaction. The semiconductor thin films are obtained from semiconductor-on-insulator wafers by the method of wet etching undercut and membrane release. We use a high-yield and high-throughput method to demonstrate nanometer-thin photodetectors with significantly enhanced light absorption based on nanocavity interference mechanism. These single-crystalline nanomembrane photodetectors also exhibit unique optoelectronic properties, such as the strong field effect and spectral selectivity. The spectral selectivity can be further exploited to develop a chip-scale, broadband spectrometer for hyperspectral imaging/sensing purposes. Later, we focus the discussion on the singe-photon avalanche photodetector using micron-meter thin semiconductor membrane. By using this ultrathin semiconductor membrane, the single photon detector we developed can be mechanically flexible.

To make a brief conclusion, the ultrathin semiconductor membrane can be used for efficient imaging/sensing purpose. The purpose can vary in different condition, whether it is for wavelength selective, hyper-spectral sensing or single-photon level imaging.

# Acknowledgements

I would sincerely thank Prof. Zhenqiang Ma for providing me this opportunity to pursue the PhD degree in the University of Wisconsin-Madison. From him, I learned not only the academic knowledge, like how to process the whole fabrication process to produce a CMOS chip, also I learned I need to work hard and efficiently to achieve academic success.

I would also like my PhD committee member for spending the time to review my thesis and related work. Most of the work in my thesis is very related to my committee professor research works. I sincerely thank them for taking their time to guide me in this research works.

My research funding is from the following grants: DoE (DE-NA0002915), AFOSR (PECASE: FA9500-09-01-0482, SBIR: FA9550-13-C-0011 and STTR: AF10-BT14 II), ONR (N00014-13-1-0183 and N00014-13-1-0226), DARPA (N00014-18-1-2032), NSF (ECCS1308520), US Endowment for Forestry and Communities (E17-21Wisconsin Alumni Research Foundation (WARF), University of Wisconsin Foundation, and Foundation Fighting Blindness (TA-RM-1016-0700-UW-GH).

Finally, I would like to thank my wife, Mrs. Chen Sun for her supporting my academic career. She is also about to obtain her PhD degree in late 2019, I hope we can live a happy life together in future. I would also thank my parents, Mr. Xiaohua Xia and Mrs. Xiaohong Hu for supporting me go to USA for academic career.

# Abbreviations

α: material absorption coefficient

*k*: material extinction ratio

η: photo detector quantum efficiency

μ: material electron/hole carrier mobility

λ: light wavelength

ω: light frequency

APD: Avalanche photodiodes

SPAD: Single-photon avalanche photodiodes

σ: semiconductor materials ionization ratio

ε: The triggering probability of a single-photon avalanche photodetector when photon is absorbed in the device and an electron/hole pair is generated

SOI: silicon on insulator

GeOI: germanium on insulator

FSI: Front side illumination

BSI: Back side illumination

# Table of Contents

## Contents

# 1 Introduction

## 1.1 Motivation

Miniaturization of electronic and optoelectronic device is the constant goal for electrical engineers, since scaling down the device size could offer better working performance (higher operation speed[1,2], lower power consumption[3–5]) and more competitive fabrication cost. Due to this reason, the past decade witnessed a rapid growth of ultrathin and atomically thin electronics and optoelectronics devices due to the advances in the development of new two-dimensional (2D) and ultrathin nano-membrane materials[6–8]. For example, the atomically thin, 2D graphene material has very high electron mobility due to its unique electronic band structure. Engineers from IBM Company have demonstrated that an ultra-fast graphene photo detector with photo response speed over 500 GHz[1]. Some other 2D material, like molybdenum disulfide ($MoS_2$), exhibit very high photo response gain[9]. Such high photo response gain can be exploited to detect single-photon level light source when the material is used as photon absorbing and silicon substrate is used as carrier transit layer[6]. Many other unique electronic, mechanical and optical properties can be found in publications, these findings pave the way for future applications such as quantum computing[10], efficient energy harvesting[11] or high-performance mechanical materials[12] for industry purpose. On the other hand, 2D versions of conventional semiconductor materials (e.g. silicene and germanene) also received great interest due to their excellent optoelectronic properties[13,14] and compatibility with current mature silicon-based electronics and

silicon complementary metal-oxide-semiconductor (CMOS) circuit processes[15–17]. Si- and Ge-based 2D or ultrathin materials are particularly attractive since they can be readily integrated with existing electronic devices/structures while other 2D materials require significant efforts to overcome this technical barrier in monolithic integration. Although these new thin film materials opened opportunities for electronics and optoelectronics, their ultrathin or atomically thin nature resulted in intrinsic limitations or challenges. For instance, in most thin-film energy harvesting/conversion applications, there is a long-existing trade-off between optical absorption and thickness of semiconductor materials. When the absorptive materials are scaled down to ultrathin (e.g. sub 50 nm) or atomically thin (e.g. sub 5 nm) dimensions, their light-matter interactions such as optical absorption, energy conversion efficiency or nonlinear optical responses are weak. Consequently, absorption enhancement strategies will introduce revolutionary advances to these ultrathin film materials/devices.

Recently, thin-film interference in lossy, ultrathin semiconductor layers received extensive research efforts due to their potential applications for integrated optical filters[18], high-efficiency ultrathin film energy harvesting devices[19], and energy conversion materials/structures[20]. For instance, 5-20 nm Ge thin films were coated on flat Au surfaces to exploit strong interference effects and achieve high absorption at resonant wavelengths in the visible to near infrared (IR) spectral region[21]. However, in this resonant absorption mechanism proposed by Kats et al[22], a large fraction of the light can penetrate into the metal reflector and obtain a large phase change, which will

inevitably introduce optical loss in the metal film. For instance, the total peak absorption of a 3.1-nm-thick Ge film on Au film is 81% at the wavelength of 488 nm with only 31% absorbed by the top Ge film. Therefore, to develop efficient energy harvesting devices, the optical absorption in the metal reflector has to be minimized. To overcome this limitation, in a recent report[23], a lossless phase compensation layer is introduced between the top ultra-thin film and metal back reflector to maintain the spectrally tunable resonant absorption condition in a planar absorptive nano-cavity. As a result, we demonstrated over 60% resonant absorption within a 1.5-nm-thick amorphous Ge film (approximately 6 atomic layers thick). Importantly, the phase-change penetration into the metal reflector with finite optical conductivity is unnecessary so that metals with better conductivity such as silver or aluminum can be used to realize the significantly enhanced absorption in ultra-thin layers instead of Au films employed in Kats et al[21]. Particularly, an ultrathin active layer is promising to significantly enhance the carrier extraction and quantum efficiency. Therefore, this architecture will enhance the light-matter interaction of ultra-thin absorbing films and overcome the limitation between the optical absorption and film thickness of energy harvesting materials. This novel optical cavity structure can greatly enhance the photo detector performance. By integrating nano-meter thick, single crystalline semiconductor thin film with this nano-cavity interference mechanism, strong absorption could be achieved. The interference mechanism could be further exploited to achieve wavelength selective absorption property to replace the current bulky,

expensive spectrometer devices. Furthermore, due to the significantly reduced volume of the active material, the thermal noise can be reduced accordingly. Importantly, due to the CMOS compatible processes, the proposed single-crystal semiconductor membrane with optical nano-cavity integration can be fabricated over large scale (e.g. wafer scale), which is superior over current 2D-material-based optoelectronic devices.

## 1.2 Background–Optoelectronic properties of semiconductor materials

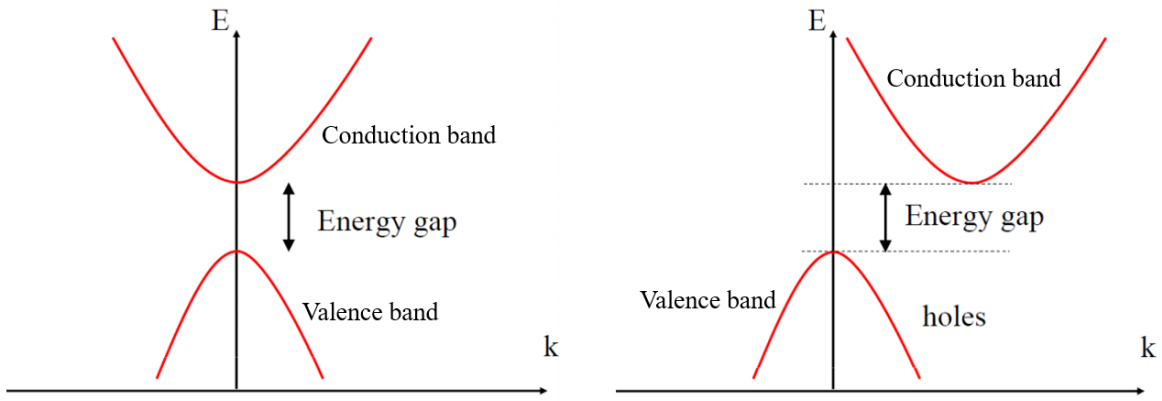


**Figure 1.1:** Bandgap structure of direct band gap semiconductors and indirect band gap semiconductors

The band gap structure is the key parameter deciding the optoelectronic property of the semiconductor. The semiconductor can only absorb the photon when the photon energy is equal or larger than the semiconductor band gap. Fig.1.1 shows two typical band gap structure, which is direct band gap and indirect band gap. The typical direct band gap materials are InP, GaAs, GaN, InAs or GaSb, the typical indirect band gap materials are Si, Ge, CdS or GaP. Compared with the direct band gap materials, the indirect band gap materials can only absorb the photon with the phonon assist. The phonon can change the momentum vector of the electron so that the photo generated

electron carriers can be excited to the conduction band and become free electrons. Therefore, theoretically, direct band gap materials show higher efficiency when absorbing the light. However, it is expensive to obtain the direct band gap materials, so silicon and germanium are two typical materials that the industry is currently using to fabricate the photo detection devices.

To quantitatively characterize the absorbing ability of a semiconductor, a figure-of-merit termed as absorption coefficient is used. The absorption coefficient determines how far into a material light of the wavelength can penetrate before it is absorbed by the semiconductor. For example, in a material with a low absorption coefficient, light is only poor absorbed, and if the material is thin enough, the material can appear transparent to the corresponding wavelength. The absorption coefficient depends on the material and also on the wavelength of light which is being absorbed.

Fig.1.2 shows the absorption coefficient of six types of semiconductor. Notice that semiconductor materials have a sharp edge in their absorption coefficient, since light which has energy below the band gap does not have enough energy to excite an electron into the conduction band from the valence band. Consequently, this light is not absorbed. When the light can be absorbed by the semiconductor, the value of the absorption coefficient is decided by the wavelength, as can be seen in Fig.1.2. The probability of absorbing a photon depends on the likelihood of having a photon and an electron to interact in a way that the electron can move from the valence band to conduction band to become a free electron carrier. For the wavelength which the photon energy is slightly

higher or equal to the band gap energy, only electrons around the valence band edge can interact with the photon, hence, the absorption coefficient is very low. As the photon energy increases, more electrons in the valence band can interact with the photon. Therefore, the absorption coefficient increases when the photon energy increases.

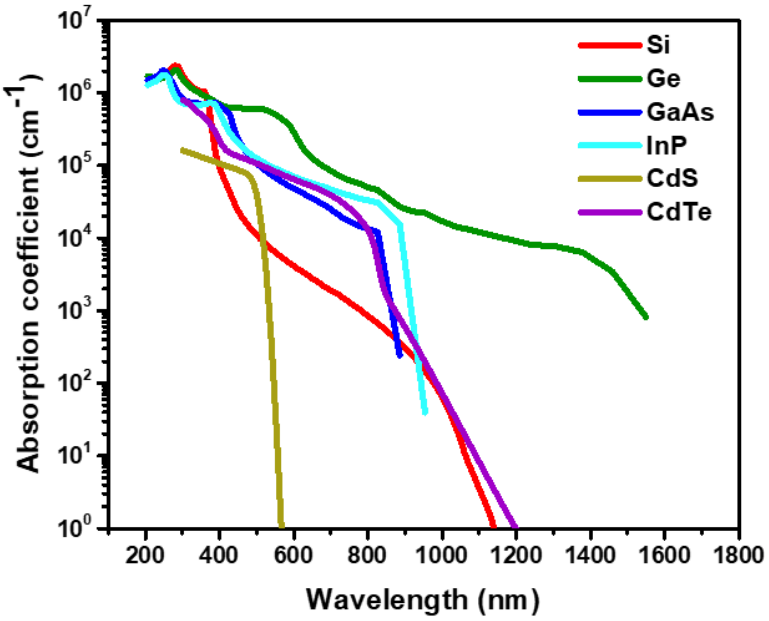


**Figure 1.2:** Absorption coefficient with six types of semiconductor in the room temperature of 300K

The absorption coefficient $\alpha$, is defined by the following equation: $\alpha = 4\pi k/\lambda$, where $\lambda$ is the light wavelength and $k$ is the material extinction coefficient. Another parameter often used to describe the absorption ability of one material is termed as absorption depth, which is defined as inverse of the absorption coefficient, which is $\alpha^{-1}$. The absorption depth describes the penetration depth at which the intensity drops to about 36% of its original intensity. The larger the absorption depth is, the weaker the material can absorb the light.

## 1.3 Background–Properties of different types of photo detector and their major applied area

The semiconductor absorbs light and convert the photon energy into free electron-hole pairs. There are several designs of photo detector to extract those electron-hole pairs, which is photoconductor, photodiode, avalanche photodiode, and single-photon avalanche photodiode.

### 1.3.1 Photoconductors

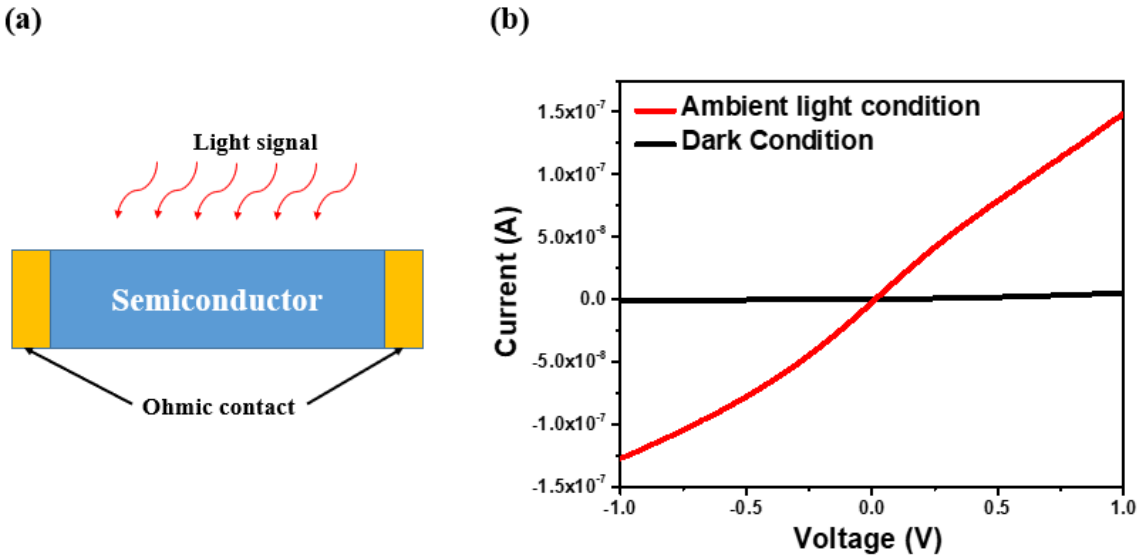


**Figure.1.3:** Schematic figure of a typical photoconductor and current-voltage response of a photoconductor under dark condition and light condition

Fig.1.3(a) shows the schematic diagram of a typical photoconductor, which is mainly composed of the absorbing semiconductor layer and the two metal electrodes for electron-hole pair collection. As the light incident on the semiconductor layer and being absorbed, free electron-hole pairs are generated in the semiconductor. More generated electron-hole pairs in semiconductor means the resistance of the semiconductor slab will drop accordingly, which results in the change of the current-

voltage behavior. Fig.1.3(b) shows the typical current-voltage behavior of a fabricated photoconductor, the current increases very significantly when the photoconductor is brought from dark condition to the ambient light condition. Because the photo sensing area is usually in the order of tens of $mm^2$ scale, the operation speed of the photoconductor is not high, typically lower than 10 MHz, since the electron-hole carrier transit time is in the order of micron-seconds. Yet the photoconductor is still commonly used in lots of area where the high-speed photo detection is not required. For example, the street-light detection, camera light meters or low-cost infrared light detectors are the most usual case where the photoconductors are being used.

### 1.3.2 Photodiodes

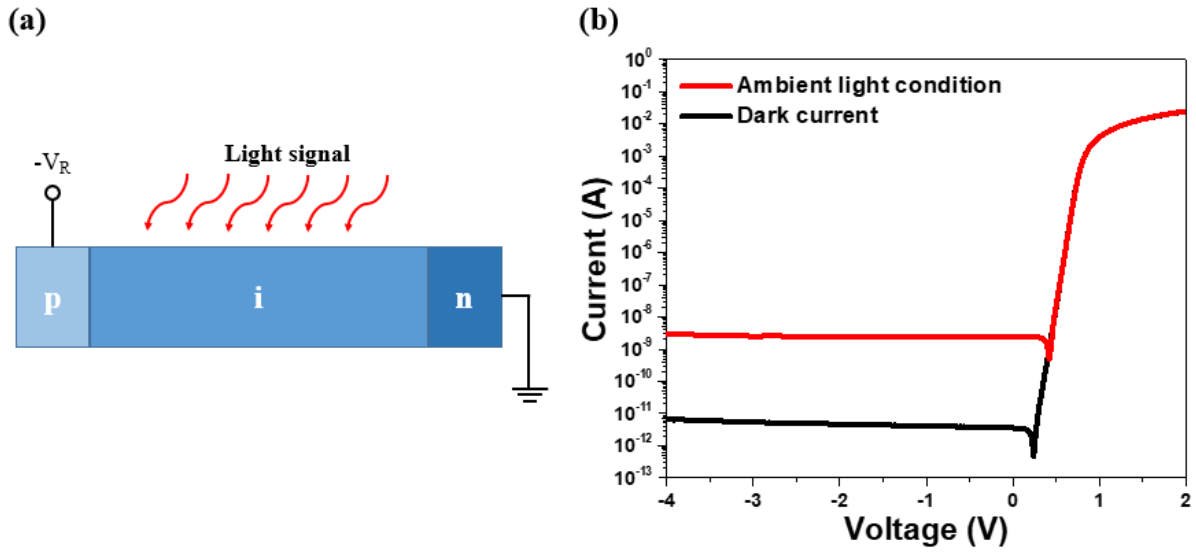


**Figure.1.4:** Schematic figure of a typical photodiode and current-voltage response of a photodiode under dark condition and light condition

A photodiode is composed of p-i-n doped region in one semiconductor slab, anode electrode and cathode electrode. Because of the doping profile, a depletion region can be formed in the semiconductor slab. The depletion region has much higher resistance

than the doped region, therefore, most voltage is biased at this depleted region. Fig. 1.4(a) shows the schematic diagram of a typical p-i-n photodiode. Reverse bias is added to the device to keep the intrinsic region depleted. Fig.1.4(b) shows the typical current-voltage behavior of the photodiode. When the reverse voltage is added, current keeps at an almost constant level, once the photon is absorbed in the intrinsic region, the electron-hole pairs can be extracted to the cathode and anode respectively and collected by the reading circuit. A typical parameter termed as the quantum efficiency is used to describe the detection efficiency of one p-i-n photodiode. Quantum efficiency is defined as the number of generated electron-hole pairs by absorbed photon divided by number of all photon incident on the device. An ideal photodiode can have close to unity quantum efficiency[24]. Therefore, for a given quantum efficiency, the photo responsivity can be calculated. The equation is as follows: $R = \eta \times \lambda/1.24\ (A/W)$, where $R$ represents photo responsivity, $\eta$ is quantum efficiency and $\lambda$ the light wavelength. Because of existence of intrinsic layer, the photodiode can operate at high speed (up to 50 GHz) (cite here). The major applications of the photodiode are for optical receivers in optical communications, photovoltaic solar cells and high sensitivity infrared photo detection.

### 1.3.3 Avalanche photodiodes

The avalanche photodiode is similar with the common photodiode, which is composed of the p-i-n doped semiconductor slab. The difference of the avalanche photodiode is the added reverse voltage bias. An avalanche photodiode works in higher

reverse voltage bias. Under higher reverse voltage bias, the photo generated free carriers will be accelerated and cause impact ionization during the carrier drift period[25,26]. Thus, the photo generated signal can be amplified during this impact ionization. Fig.1.5 (a) shows the typical current voltage behavior of an avalanche photodiode. The avalanche photo current gain can be calculated as follows: $G = (I_{ph} - I_{dark})/I_{dark}$, where the $I_{ph}$ represents the current under ambient light condition, $I_{dark}$ represents the current under the dark condition. Both the dark current and the light current increases when the reverse voltage increases. The calculated avalanche gain can be seen in Fig.1.5 (b). The typical gain for an avalanche photodiode is around 5 ~ 20. Under this avalanche gain, the photo response and the detector noise reach the optimized point. A figure-of-merit termed as the product of gain and bandwidth is used to quantify the avalanche photodiode. The highest gain and bandwidth product so far was obtained by InGaAs avalanche photodiode, which is about 424 GHz[27]. The typical application for avalanche photodiode is used as high sensitivity, high speed avalanche receiver for optical communications[28,29].

### 1.3.4 Single-photon avalanche photodiode

The single-photon avalanche photodiode can record very weak signal down to single photon level[30]. The detector works in the region called as Geiger mode. In this mode, one pair of photon-generated carrier can trigger the p-i-n junction to mA level of current. The reason is, under the Geiger mode, the impact ionization caused by one electron-hole pair can be sustained in the junction region if the voltage bias is kept the

same value, which means the current can go to infinity value. Therefore, the device needs to be quenched after the singe-photon detector is triggered. During the quenching time the device cannot detect the incoming light signal until it is fully quenched to its original state. Therefore, the quenching time is called as the dead time of the single-photon avalanche photodiode. The typical dead time of a single-photon avalanche photodiode is around 5 nano seconds[31]. A quenching circuit needs to be designed for the single-photon avalanche photodiode. To record the avalanche event, a monitoring oscilloscope is needed to record the avalanche voltage pulses. The best material used for single photon detection is silicon, since it is easy and not expensive to fabricate, low dark current and has very high impact ionization ratio compared with the other semiconductor. The silicon based single-photon avalanche photodiode is mainly for visible wavelength and near-infrared wavelength photo detection[25]. For the telecommunication wavelength, InGaAs based single-photon avalanche photodiode are generally used. However, there are usually expensive. These days the germanium on silicon single-photon avalanche photodiode is developed and this type of device can replace the InGaAs based one and offer a more cost-competitive price. The typical application for single photon avalanche photodiode is the bio-fluorescence detection[32], Light Detection and Ranging (LIDAR)[33] and none-line of sight imaging[34].

## 1.4 Background – Recent developments of photo detectors

An ideal photodetector has fast operational speed, high detection, and ultra-low noise. Yet these three factors are very difficult to achieve at the same time. For example,

the graphene-based photo conductor can reach very high operation speed (up to 500 GHz) due to its Dirac-cone electronic band structure. However, since graphene has no band gap, the dark current is very high[2], resulting in high detector shot noise, and since the graphene is atomic thin material, the absorption for each atomic layer for graphene is only about 2%[35]. To reduce the detector noise and increase the absorption efficiency, bulk silicon with anti-reflection coatings is the optimal choice[19,36]. The quantum efficiency of one recent work reaches close-to-unity value for a bulk silicon-based photodiode with black silicon anti-reflection coatings. Whereas the photo response speed is calculated only to be around 1 GHz, since the large volume photodiode photo response speed is limited by the carrier transit time. To increase the photo response speed while still keeping the dark current low, a very thin semiconductor p-i-n photodiode can be designed and fabricated[37]. As seen in the most recent work, the photodiode transient photo response is about 12 picoseconds, which corresponds to about 10GHz photo response speed.

## 1.5 Scope of the dissertation

This dissertation mainly focuses on developing high absorption efficiency, low dark current noise photo detection devices based on ultrathin semiconductor membranes. Compared with bulk semiconductor materials, thermal noise can be greatly suppressed due to the reduced volume of photo detecting material. To overcome the low absorption of the thin semiconductor membrane, we adopted several methods to increase the absorption efficiency of the semiconductor membrane, including the

integration with the external optical nano-cavity, or fabrication of inverted-pyramid structure directly in the semiconductor membrane. Both ways show the absorption efficiency can be greatly enhanced. This enhancement brings the thin film-based photo detection devices comparable with the one commercially available in the market. Since it is thin film, more functionalities can be exploited in this device system. These functionalities are the key issue we are going to discuss in this thesis, since many of the functionalities can outperform the commercial product and enable wider applications for photo detection devices. At last two chapter of the thesis, I will focus on the design and fabrication of single photon detector by using the ultrathin semiconductor membrane. The traditional single photon detector is usually made from bulky materials, while the ultrathin-based one can be made into flexible single photon detector, which is very useful for implantable bio-fluorescence detection for diseases and for retinal prothesis. The ultrathin membrane based single photon detector can be a great candidate for future advanced bio-fluorescence single photon detection or single photon imaging.

# 2 The employment of semiconductor membrane for photo detection and its unique optoelectronic properties

## 2.1 Introduction

Recently, ultrathin semiconductors (e.g. silicon (Si)/germanium (Ge) nano-membranes[38,39] and two-dimensional (2D) materials[40–42] have emerged as attractive building blocks for miniaturized optical/optoelectronic devices. To enhance the light matter interaction, thin-film interference in lossy, ultra-thin semiconductor layers received extensive research efforts[21] due to their potential applications for integrated optical filters[18], high-efficiency ultrathin-film energy harvesting devices[43], energy conversion materials/structures[44] and dynamic wave shaping meta-surfaces[45]. For instance, 1 ~ 20 nm Ge thin films were coated on flat metal films to exploit strong interference effects and achieve high absorption (i.e., 65% ~ 95%) at resonant wavelengths in visible to near infrared (IR) spectral region[23]. However, all these works are based on amorphous semiconductors, which are usually achieved by sputtering or evaporation processes. Since obtaining single crystal materials is difficult by these two above methods. Consequently, their optoelectronic device performance[22] is far inferior to those crystalline-material-based counterparts. Although single-crystalline films can be obtained through rapid melt growth (RMG)[46,47], wafer bonding[48] and/or epitaxial growth[49], each of these methods has its limitations. For example, the RMG method will introduce high temperature process flow (> 900 °C) to re-crystallize the Ge material. The wafer bonding method will require the substrate removal after the process and the

epitaxial growth needs very thick buffer layers. Fabrication of crystalline thin films on foreign substrates turns out to be critically important for ultra-thin optoelectronics. The recently emerging membrane transfer technology provides a promising way to enable the combination of crystalline thin films with foreign substrates[50]. In particular, the foreign substrate can be designed with effective photon management functionalities to greatly enhance the weak light absorption in ultra-thin materials. Here we demonstrate a new method to realize high-performance ultra-thin optoelectronic devices based on nanocavity enhanced mechanisms. Using single-crystalline semiconductor membranes on functionalized nanocavity substrates, we achieve strong light-matter interaction within nanometer-thick Ge films. While we use Ge as an example to demonstrate a high-performance photodetector, our method, however, can be applied to other semiconductors (including 2D materials[7,8] to enable the development of improved ultra-thin optical/optoelectronic devices.

## 2.2 Fabrication method of semiconductor membrane

### 2.2.1 Fabrication and characterization of the lab made GeOI wafer

We used the smart-cut process[51] to fabricate the GeOI. The process started with a p-type (gallium doped) 4-inch bulk Ge wafer. We ion-implanted a uniform H+ layer in the germanium wafer with a dose of $1\times10^{-17}$ $cm^{-2}$ and an energy of 100 KeV. A H+ peak position (RP) was carefully designed at 700 nm from the Ge surface to acquire a 400-nm-thick Ge layer after the exfoliating process. A 1-μm-thick $SiO_2$ layer on Si wafer was obtained by thermal oxidation as the buried oxide (BOX) layer. Then the Ge wafer

was flipped over. The $O_2$ plasma was used to clean both surfaces for bonding. The wafer bonding process was performed using the EVG Wafer Bonding System (EV 801) under the vacuum of $7\times10^{-5}$ mbar. After that, a two-step, low temperature annealing at 200℃ and 250℃ was carried out in a nitrogen-filled oven to achieve the exfoliation of the Ge wafer. The purpose of two temperature steps is to prevent the wafer cracking during the temperature rising process. The Ge membrane was very rough after the exfoliation and a Chemical Mechanical Polishing (CMP) process was required to polish the Ge membrane surface and thin down the Ge layer to the desired thickness (100 nm).

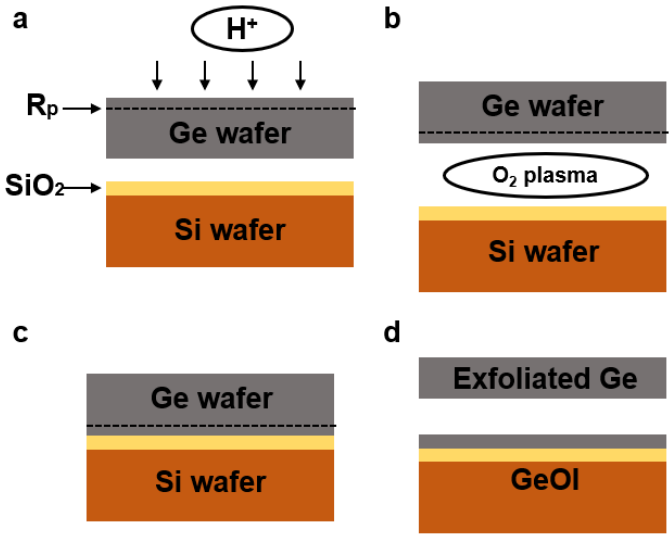


**Figure 2.1:** Smart-cut™ based process flow of the GeOI

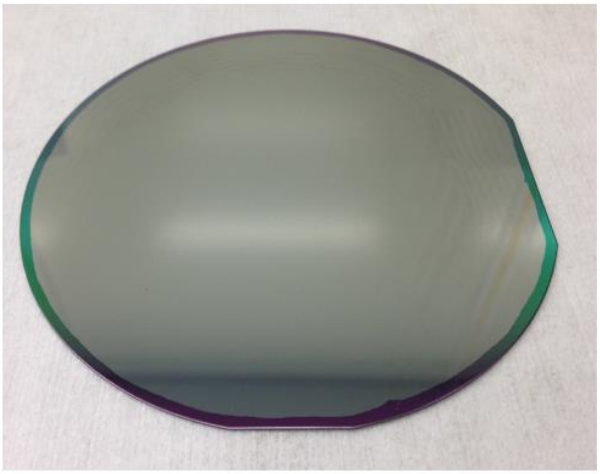

**Figure 2.2:** Lab-made 4-inch GeOI wafer.

To characterize the lab made GeOI, we used the Panalytical X'Pert MRD high resolution X-ray diffraction (XRD) to characterize the single crystallinity of the germanium membrane. Fig.2.3 shows the XRD result of the GeOI with a peak at 33.1°, confirming the singe crystallinity. The fringes on both sides of the peak are introduced by the X-ray interference with the 100-nm-thick Ge nanomembrane. The interference fringes indicate that both sides of the Ge nanomembrane are smooth and flat. We also use the Horiba LabRAM ARAMIS Raman spectroscopy to characterize the GeOI. As shown by Fig.2.2, the fabricated GeOI has the same peak location of 300.9 $cm^{-1}$ as the Ge wafer, confirming that the fabricated GeOI is stress and strain free. We then used the van der Pauw approach to measure the carrier concentration and carrier mobility of the p-type GeOI, as shown in Fig.2.5.

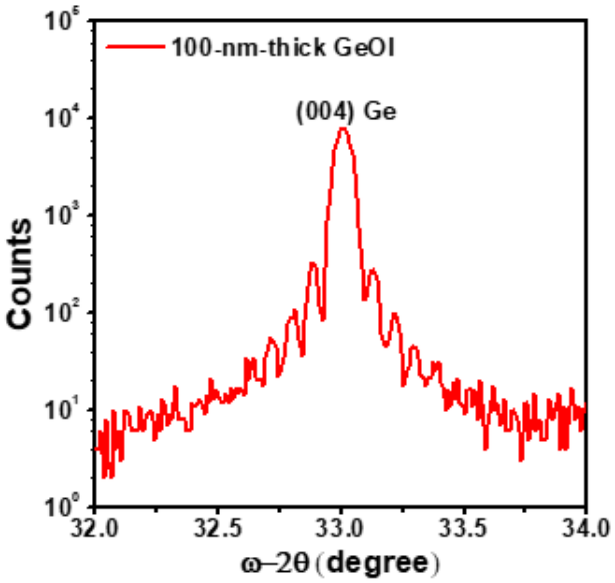


**Figure 2.3:** High resolution X-ray Diffraction (XRD) results of the 100 nm Germanium/1-μm-thick $SiO_2$/Silicon wafer.

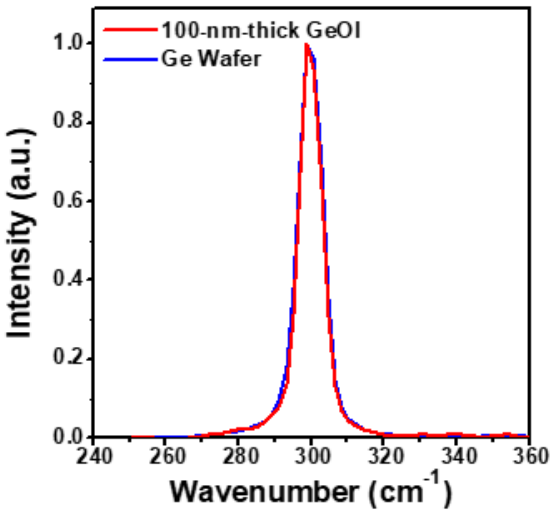


**Figure 2.4:** Raman scattering result of a fabricated GeOI wafer compared with that of a bulk germanium wafer. The same peak position indicates the GeOI is strain and stress free.

| Parameter | P-Type GeOI |
|---|---|
| **Sheet Resistance ($R_s$)** | 617.7 Ω/□ |
| **Hall Coefficient ($R_H$)** | 97.9 $m^2/C$ |
| **Carrier Mobility ($\mu_p$)** | 393 $cm^2\ V^{-1}\cdot S^{-1}$ (hole) |
| **Carrier Concentration** | $1.447\times10^{18}$ $/cm^2$ |

**Figure 2.5:** Electronic properties of p-type GeOI sample.

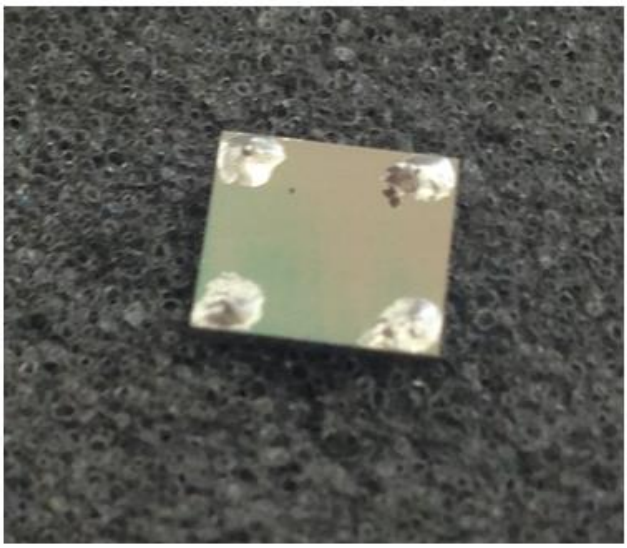

**Figure 2.6:** The GeOI sample used for the van de Pauw measurement. The silver paste is used for the

electrical contact.

### 2.2.2 Semiconductor transfer print process

In this work, we first employed the membrane transfer method[50,52] to realize the integration of crystalline semiconductor films with a foreign substrate, as shown in Fig.1a. Since transfer printing method is a quick and high yield way to print membrane to any pre-designed substrate, while the wafer bonding technique or Smart-cut$^{TM}$ method strictly require the target bonding substrate be atomically flat, otherwise the yield is very low. We started from a Ge-on-insulator (GeOI) wafer (Fig.2.2) as the source wafer. The thicknesses of the top Ge layer and the insulator layer of $SiO_2$ are 100 nm and 1 μm, respectively. The fabrication and characterization details of the GeOI wafer can be found in Fig.2.1 – 2.3. We then released the top Ge membrane using hydrofluoric acid (HF) (Fig.2.7 (a)) and transferred it onto a foreign substrate using Polydimethylsiloxane (PDMS) (Fig.2.7(b)). Finally, we used low-power dry etching to thin down the membrane to the desired thickness (Fig.2.7(d)). Fig.2.9 shows the optical microscope images of transferred Ge membrane samples. The substrate was designed to enhance the light absorption in Ge membranes. It consists of three layers: i.e., a top $Al_2O_3$ layer, a middle silver (Ag) layer and a Si substrate. The top Ge film thickness, measured by atomic force microscopy (AFM), ranges from 10 to 60 nm. These films exhibit different colors under the white light illumination because of the optical interference (Fig.1b).

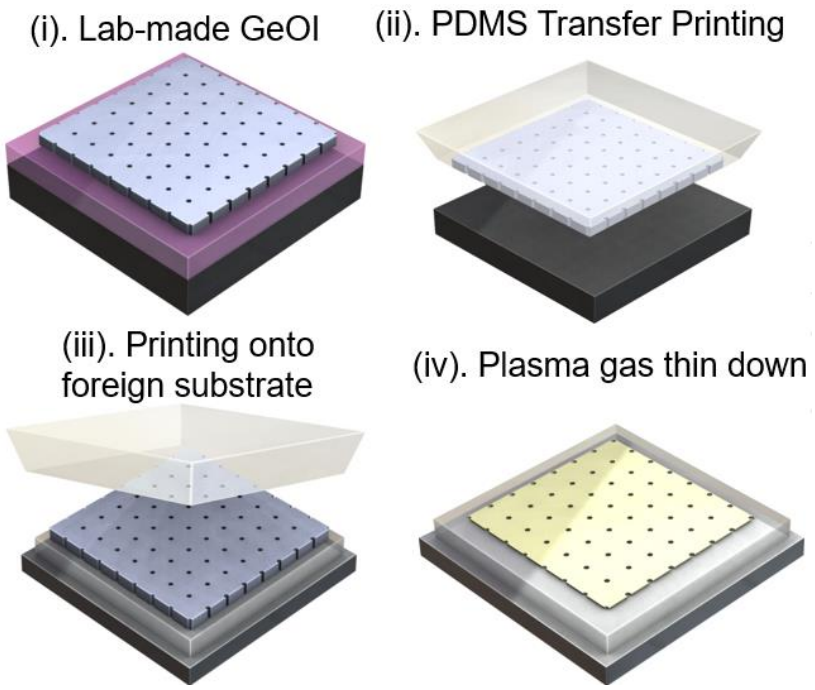


**Figure 2.7:** Schematic of the fabrication process flow of the Ge nanomembranes on foreign substrates. The lab made GeOI was used as the source wafer and the membrane transfer printing method was then employed to transfer the Ge membrane onto a foreign substrate. Subsequent thin down process was adopted to obtain the desired Ge thickness (10 ~ 60 nm).

To reveal the crystal quality of the Ge membrane, we performed high-resolution X-ray diffraction (HR-XRD) characterization. Fig.2.8 shows the (004) ω-2θ triple axis scans. A clear peak at 33.1° (red line) confirms the single crystallinity of transferred Ge membranes[53]. In comparison, we also examined an evaporated and annealed Ge film with the same thickness. In this experiment, the evaporated amorphous-Ge film was annealed at 500 ℃ to improve the crystallinity[54]. This type of poly-crystalline Ge film was typically used to fabricate Ge photodetectors on foreign substrates using low temperature processes[55]. However, no peak was observed at 33.1° for the blue line in Fig.2.8, which indicated the lack of single crystallinity. This comparison reveals the advantage of our membrane transfer method in the quality of Ge films, which is important for the performance of photodetectors. Another peak in Fig.2.8 at the angle

of 34.6° comes from the (100) Si substrate, which is observed in both samples. Fig.2.8(a) shows the Raman spectroscopy of these two samples. One can see a single peak at the wavenumber of 300.9 cm-1 for the transferred Ge membrane, which is another signature of the single-crystalline Ge film[53]. In contrast, multiple peaks were observed in the evaporated and annealed Ge film. These peaks are attributed to the Ge-$H_x$ and second order of Ge-Ge bonds formed in the annealing process[56]. Both the XRD and Raman results show excellent crystalline properties of the transferred Ge films. Next, we discuss the design of the foreign substrate to enhance the light-matter interaction within this crystalline thin film.

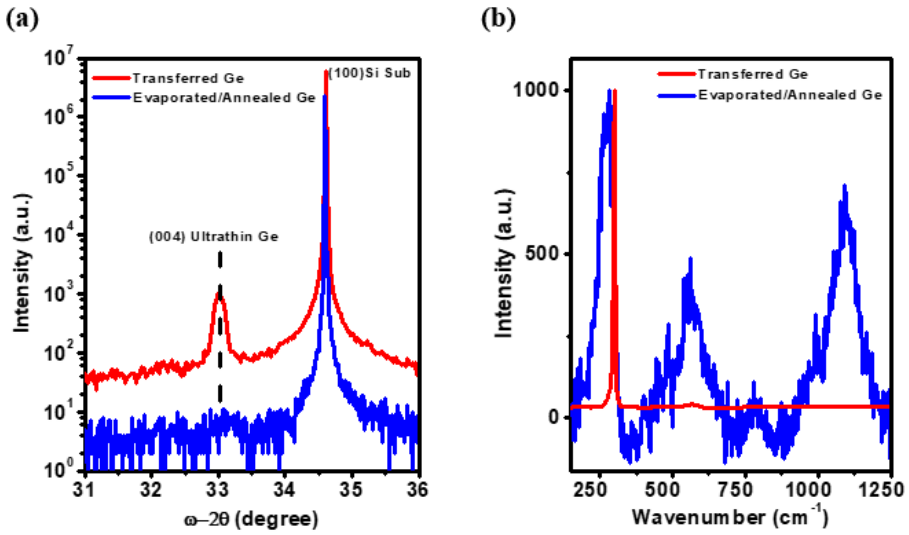


**Figure 2.8:** (a) Triple axis HR-XRD scans of our transferred crystalline ultra-thin Ge (red) and evaporated amorphous-Ge (blue) films. The thicknesses are both 20 nm. (b) Raman scattering results of the two samples. The Raman signal of the transferred Ge membrane shows the typical single peak (300.9 $cm^{-1}$) of single-crystalline Ge materials.

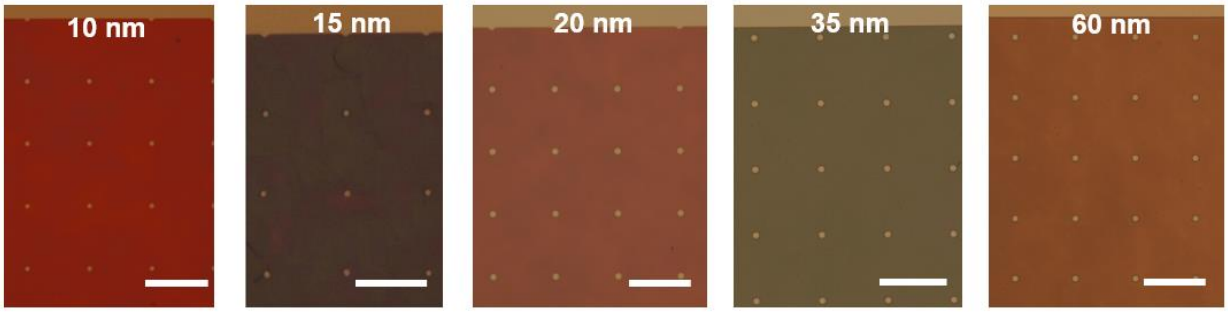


**Figure 2.9:** Optical microscope image of ultrathin Ge (10 ~ 60 nm), which is transfer-printed on $Al_2O_3$/Ag/Si substrates. The scale bar is 75 μm for all five sub-figures.

## 2.3 Optical characterization of semiconductor membrane

Predesigned foreign substrates allow us to use functionalized nanocavity structure to greatly improve the light absorption in nanometer-thin Ge films. The absorption depth of Ge varies from approximately 120 nm (at the wavelength of 700 nm) to 390 nm (at the wavelength of 900 nm), much thicker than our thin films. In this case, the absorption in a 20-nm-thick region is less than 16% in this wavelength range. To overcome this limitation of weak absorption, we use layered substrate that consists of a 220-nm-thick lossless dielectric spacer and a reflective Ag mirror to form a functionalized nanocavity structure (Fig.2.10). The function of the lossless dielectric spacer is working as a phase shifter, also the refractive index contrast between $Al_2O_3$/Ag is larger than the previous work of Au/Ge, larger refractive index make the optical loss in the metal film become less.

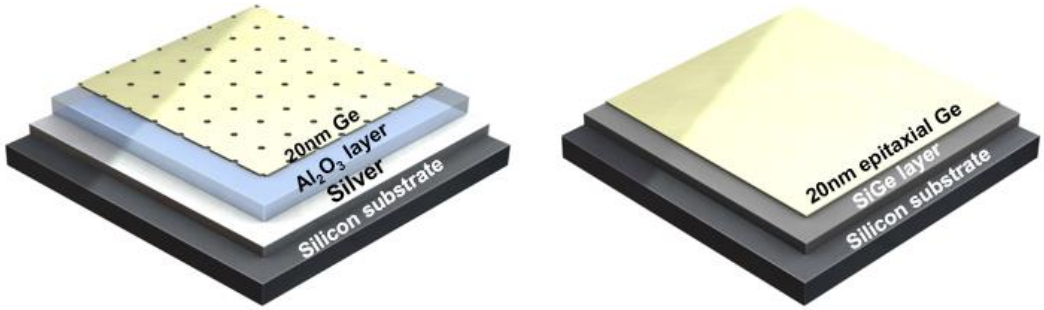

**Figure 2.10:** The schematic of ultrathin Ge (20 nm) nanomembrane on the foreign substrate. The schematic of a traditional epitaxial Ge on $Si_{0.75}Ge_{0.25}$ buffer layer/Si substrate.

As shown by the solid line in Fig.2.11, the numerical simulated absorption in a 20-nm-thick Ge membrane on a 220-nm-thick $Al_2O_3$/Ag cavity reaches 81% around the resonant wavelength of 733 nm. The spatial distribution of light absorption, obtained in a simulation based on the finite element method, shows enhanced absorption in the ultra-thin layer of Ge (Fig.2.11(c)). In contrast, the absorption in ultra-thin crystalline Ge films without photon management is weak. For example, ultra-thin crystalline Ge films can also be fabricated using epitaxial growth, as illustrated in Fig.2.11(d). But the substrate should be a SiGe buffer layer to fulfill the lattice matching condition. Under this situation, the same Ge film only absorbs less than 10% of the incident light at 733 nm, as shown in Fig.2.11(d). The spatial distribution of light absorption in this system is shown in Fig.2.11(d), with the same color map in Fig.2.11(b), showing obviously weaker absorption within the 20-nm-thick Ge film. Therefore, the foreign nanocavity substrate can significantly enhance the optical absorption within the ultra-thin crystalline film, which is highly desirable for optoelectronic devices.

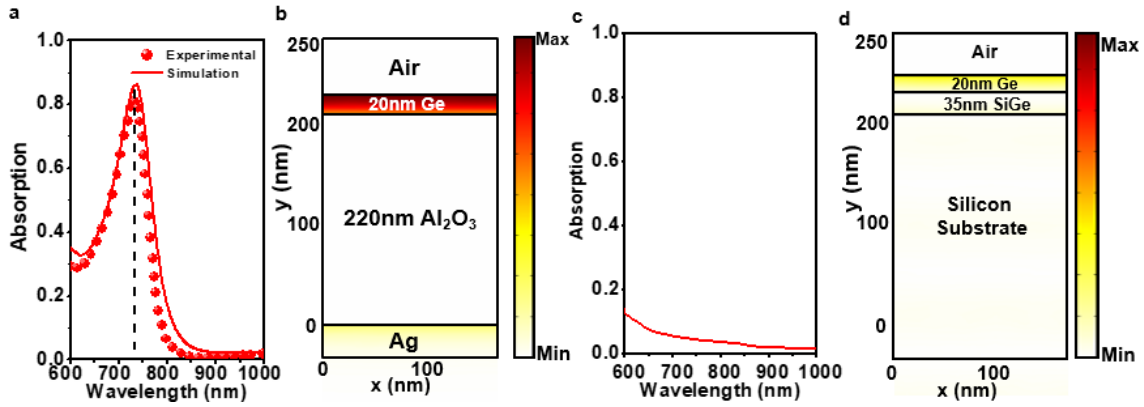


**Figure 2.11:** (a) Absorption spectra (b) Spatial distribution of the absorption for the structure (c) The spatial distribution of the absorption (d) Absorption spectra for the structure shown in (c). The color bars

in (b) and (d) use the same scale for direct comparison.

## 2.4 Optoelectronic characterization of the semiconductor membrane

The schematic of a nanocavity enhanced photodetector device and its optical microscope image are shown in Fig.2.12 (a) and (b), respectively. We first fabricated this device and measured its performance under dark and illuminated conditions. In this experiment, we placed a 17-nm-thick p-type (gallium-doped) Ge nanomembrane on a 220-nm-thick Al2O3/Ag cavity and obtained an absorption peak at 733 nm (dotted line in Fig.2.11(b)), agreeing well with the theoretical prediction (solid line in Fig.2.11 (b)). The slight difference in Ge film thickness should be attributed to the optical constant difference of this p-type Ge film. In particular, the bottom Ag film serves a dual role of mirror and gate electrode for this nanomembrane-based field-effect transistor device. By using nickel/gold (Ni/Au) as the contact electrode, we realized an Ohmic-like contact for the photoconductor, as shown by the current-voltage (I-V) sweep results in Fig.2.12(c). We repeated I-V sweep under different illumination intensities by tuning the monochromatic 733-nm light source from 42 nW to 2.45 μW. The photocurrent ($|\Delta I_{DS}|$) at the bias of 1 V can be calculated by the equation $|\Delta I_{DS}| = |I_{DS} - I_{dark}|$, where the $I_{DS}$ is the drain-source current under illumination and $I_{dark}$ is the dark current. We then plotted the photocurrent, $|\Delta I_{DS}|$, as the function of the incident power, $P_{inc}$, illuminated on the ultrathin Ge layer (25 μm × 50 μm) as shown in the inset of Fig.2.12(b). From the linear fitting of the photocurrent with the illuminated power, we can extract the photoresponsivity (R) of this device to be 0.17 A/W (i.e., $R = |\Delta I_{DS}| /$

$P_{inc}$).

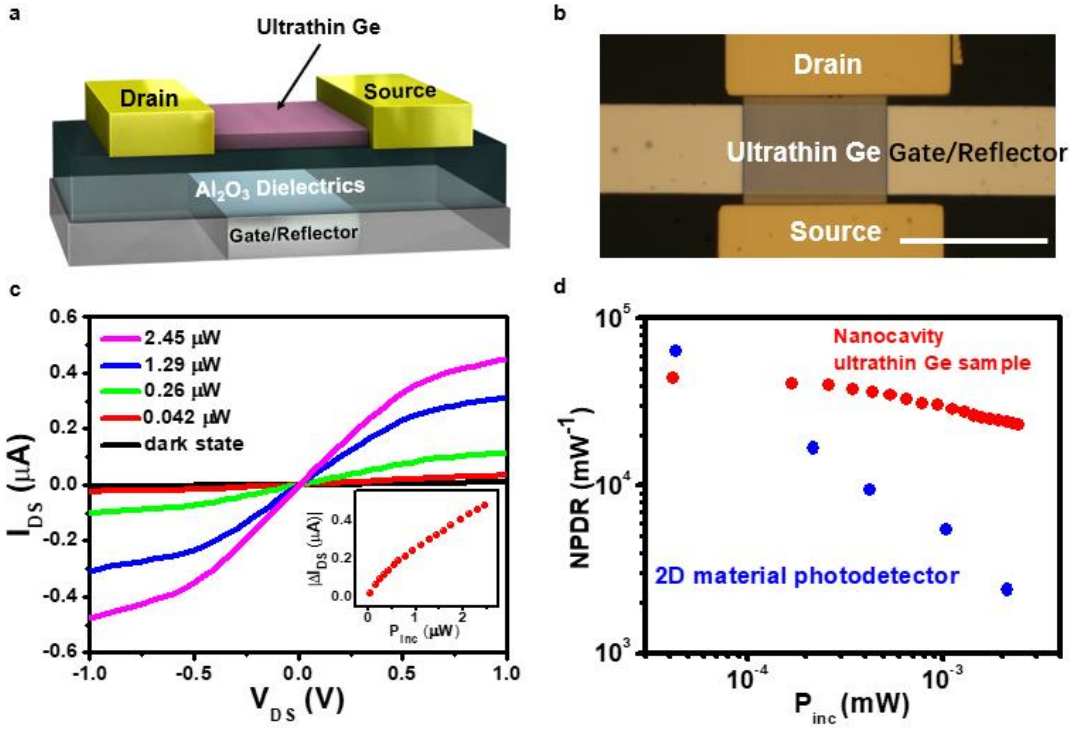


**Figure 2.12** (a) Schematic of an ultra-thin Ge photodetector on a nanocavity. (b) Optical microscope image of ultra-thin Ge photodetector. Scale bar: 50 μm. (c) The I-V curves of the p-type Ge photoconductor under dark (black curve) and illuminated (colored curves) conditions. Inset: The photocurrent shows a linear relationship with the illuminated power. (d) Calculated normalized-photocurrent-to-dark current ratio (NPDR) with the illuminated power, and its comparison with a MoS2 photodetector.

One important figure of merit for metal-semiconductor-metal (MSM) photodetectors is the normalized photo current to dark current ratio, which is expressed as: $NPDR=(|\Delta I_{DS}|/I_{dark})/P_{inc}$[57]. A larger value of this parameter indicates the better suppression of dark current without sacrificing the photoresponsivity. Considering the previously reported MSM photodetector based on Ge wafers[58], the highest reported NPDR, to our knowledge, was 3,158 $mW^{-1}$. In contrast, under the bias of 1 V, the NPDR of our device is in the range of $10^4$ $mW^{-1}$ (Fig.3d), which is over one order of magnitude higher than the previous work. In this experiment, we first investigated the stability of

the NPDR by increasing the incident power, $P_{inc}$. One can see that the NPDR of our ultrathin Ge sample (red dots) is relatively stable in the power range from 42 nW to 2.45 μW. For comparison, we also plotted the NPDR of a previously reported 2D material device based on $MoS_2$ (blue dots)[9]. This device has an NPDR with a significant change, from a value of $6.37\times10^4$ $mW^{-1}$ at the low incidence power to $2.39\times10^3$ $mW^{-1}$ (i.e., one order of magnitude lower) when the incident power reaches the μW level. This drop was attributed to the saturation of the trap states with increased light intensity. According to the relation between detectivity (D) and NPDR, which is expressed as: $D=NPDR\times(I_{dark}/2q)^{1/2}$, where the electronic charge $q=1.6\times10^{-19}$ C, this dramatic decrease of NPDR indicates a decreased detectivity of the 2D material photodetector as the optical illumination increases. However, the stable NPDR of our nanocavity sample (red dots) renders a stable detectivity in the investigated incidence power range, further demonstrating the high quality of the single crystalline Ge nanomembranes. The slightly drop of our device NPDR mainly attributes to the dry etching of the Ge thin film, in the etching process defects can be introduced.

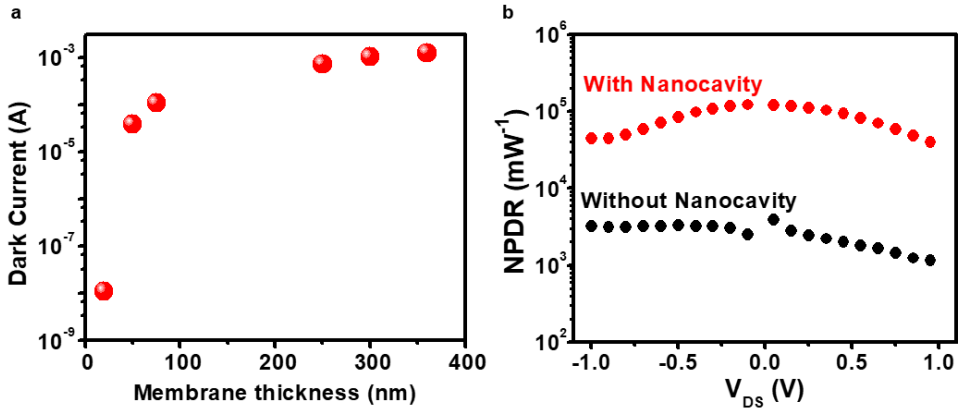


**Figure 2.13:** (a) Dark current of Ge membranes with different thicknesses. (b) NPDR comparison between the Ge photodetectors with and without nanocavity structure (GeOI based).

In addition to the stability of NPDR, the enhanced NPDR compared with previous report[57] can be attributed to two mechanisms. The first one is the suppression of the dark current, $I_{dark}$, introduced by the ultrathin Ge film. In order to verify the suppression, we fabricated photoconductors with various Ge thicknesses and measured their dark currents. As shown in Fig.2.13(a), the dark current decreases from mA to nA level as the Ge thickness reduces from 350 nm to 20 nm. Generally, ultrathin Ge nanomembranes intrinsically bring about low absorption, which limits the photocurrent, $|\Delta I_{DS}|$, and thus results in a relatively small NPDR. By introducing the foreign nanocavity, however, the absorption will be significantly enhanced, corresponding to enhanced photocurrent, which is the second reason for the improved NPDR. To better reveal the dependence of NPDR on absorption, we fabricated another photodetector constituted by a GeOI structure. The thickness of the $SiO_2$ in the GeOI sample is 1 μm. Since the thickness of the Ge film is similar to that in the nanocavity sample (i.e., 20 nm), the dark currents of the two samples were suppressed to a similar level. Fig.2.13(b) shows the comparison of NPDR between these two photodetectors. One can clearly see that, under the same bias, the nanocavity sample delivers one order of magnitude higher NPDR (i.e., ~ $4\times10^4$ $mW^{-1}$) than that of the GeOI sample (~ $3\times10^3$ $mW^{-1}$). On the respect of absorption, the absorption in the Ge layer of the nanocavity sample is 81% (see Fig.2.11), which is also one order of magnitude larger than that of the GeOI sample (6.1%, based on our simulation), demonstrating the contribution of the enhanced absorption to NPDR. Furthermore, the gate-controlled performance of the

phototransistors also takes advantage of the high absorption, as will be analyzed in the next section.

## 2.5 Absorption enhancement of semiconductor membrane integrated with optical cavity

The ultra-thin thickness, in addition to its benefit in electrical properties, also provides a new optical functionality for multi-spectral sensing because its response exhibits strong spectral tunability. To demonstrate this tunability, here we fabricated a series of nanocavity manipulated photodetectors by changing the thickness of Ge membrane on a 220nm-$Al_2O_3$/Ag cavity. Fig.2.14 shows the experimentally measured light absorption spectra of these samples.

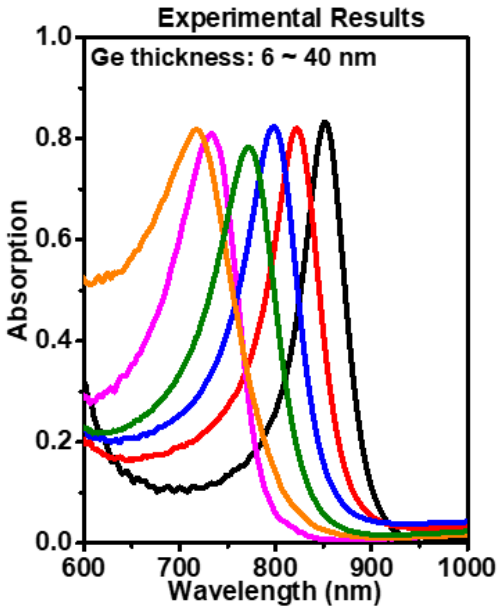


**Figure 2.14:** Absorption spectra measured by Fourier Transform Infrared spectroscopy (FTIR) of ultra-thin Ge sample, as the peak wavelength becomes larger the Ge nanomembrane thickness changes from 6 to 40 nm (the thickness increases from left to right).

As the thickness of Ge film increases from 6 to 40 nm, the wavelength of the

absorption peak changes from 715 to 862 nm, agreeing very well with numerical simulations listed in Fig.2.9. To demonstrate the spectrally tunable photoresponse, we further measured the photocurrent spectra for three photodetectors with their Ge thicknesses of 12 nm, 17 nm and 26 nm, respectively, as shown in Fig.2.15. In this experiment, a supercontinuum laser coupled with a monochromator was used as the light source. The photoresponsivity of all devices were measured under the same bias voltage of 1 V. In Fig.2.19, the simulated light absorption spectra are also plotted by solid curves, showing excellent agreement with the measured photocurrent responsivities (dots) and demonstrating the spectral tunability. Therefore, a multi-spectral ultra-thin Ge photodetector array is realizable by transferring different crystalline Ge membranes onto the predesigned nanocavity substrate.

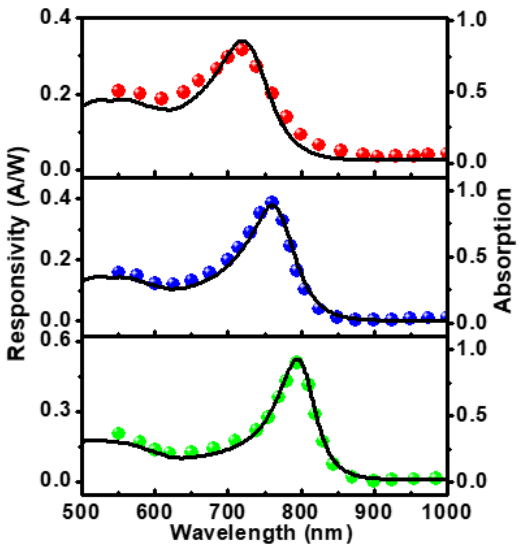


**Figure 2.15:** Left axis: photoresponsivity (A/W) results of three different samples on 220-nm-thick $Al_2O_3$/Ag substrates. The thicknesses of Ge films are (from top to bottom) 12 nm, 17 nm and 26 nm, respectively. Right axis: simulated absorption spectra of these four samples, the structure parameters are used as mentioned above, the simulation is based on full-wave Maxwell's equations.

## 2.6 Detailed performance characterization and its comparison with counterparts

To further interpret the electronic properties of the single-crystalline Ge nanomembrane transistor, we then characterized the dark drain-source current, $|I_{DS}|$, of the device with the 17-nm-thick Ge film (discussed in Fig.2.5) as the function of the gate voltage, $V_{GS}$, under $V_{DS}$ of -1 V. As shown by the dashed blue curve plotted in the log scale in Fig.2.16, the ultrathin transistor shows ambipolar behavior. By extrapolating the linear portion of the $I_{DS}$-$V_{GS}$ curve in the linear scale (red solid curve), one can extract the threshold voltage of the transistor, $V_{TH}$. Furthermore, one can estimate the hole field-effect mobility, $\mu_p$, using the equation, which is expressed as: $\mu_p=(L/W)C_{ox}^{-1}V_{DS}^{-1}(\partial I_{DS}/\partial V_{DS})$, where L and W are the Ge nanomembrane channel length and width (i.e., 25 μm and 50 μm), respectively; $C_{ox}$ is the gate capacitance per unit area of the Ge/$Al_2O_3$/Ag system (i.e., $3.647\times10^{-8}$ F/cm$^2$), determined by the expression $C_{ox}=\varepsilon_{ox}/t_{ox}=\varepsilon o\varepsilon Al2O3/tAl2O3$. Here $\varepsilon_o$ is the vacuum absolute dielectric constant (i.e., $8.85\times10^{-12}$ F⁄m), $\varepsilon_{Al2O3}$ is the relative $Al_2O_3$ dielectric constant (i.e., 8.1 for evaporated Al2O3 layer[59]) and $t_{Al2O3}$ is the thickness of the $Al_2O_3$ layer (i.e., 220 nm). As a result, the maximum $\mu_p$ of this 17-nm-thick Ge membrane transistor can be estimated to be ~148.1 cm$^2$V$^{-1}$S$^{-1}$ in the linear portion when $V_{GS}$ varies from -5 to -7.5 V (as indicated by the black line in Fig.2.16). This value is among the best reported results due to the single crystalline material quality[60–63]. Intriguingly, this nanocavity manipulated device has unique properties on its gate-controlled responses, as will be

discussed next.

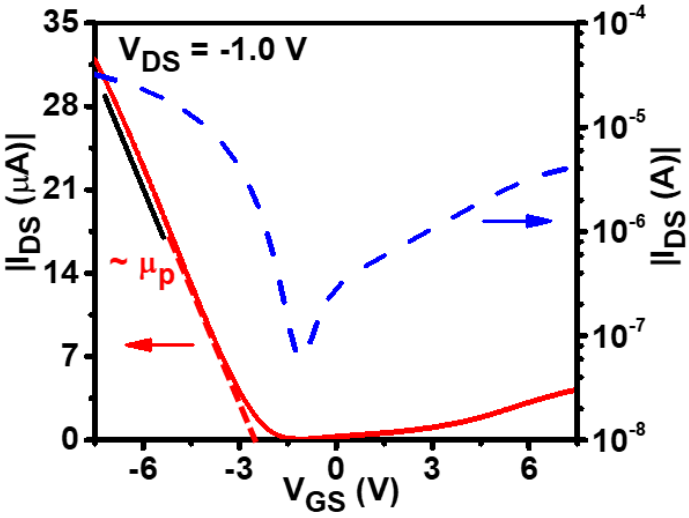


**Figure 2.16:** Transfer curves ($V_{GS}$-$I_{DS}$) of the ultrathin Ge transistor. The red curve represents the data in the linear scale, the blue dashed one represents the data in the log scale.

To reveal the gate-controlled optical response of this device, we then swept the $V_{DS}$ under different $V_{GS}$ in a steady optical incidence condition of 140.8 mW/cm$^2$. As shown in Fig.2.17 the photocurrent $|\Delta I_{DS}|$ increases as $V_{GS}$ decreases from -2 V to -6 V. Particularly, when $V_{DS}$ = -1.5 V and $V_{GS}$ = -6 V, the photoresponsivity is 4.7 A/W, which is 27.6 times larger than the responsivity of 0.17 A/W under zero gate voltage. This enhancement can be attributed to the photogating effect which plays a dominant role in many nanostructured devices, especially in nanowires[64], quantum dots[65] and 2D-material-based photodetectors[66]. However, in most aforementioned devices, the photogating effect relies on trap states in nanostructured materials, acting as localized states in the photodetecting channel. The trap-state-mediated photogating effect limits the reproducibility of the photodetector performance since the number of trap states cannot be controlled precisely in the fabrication process. Moreover, the saturation of the trap states under strong incident power usually resulted in decreased gain[67].

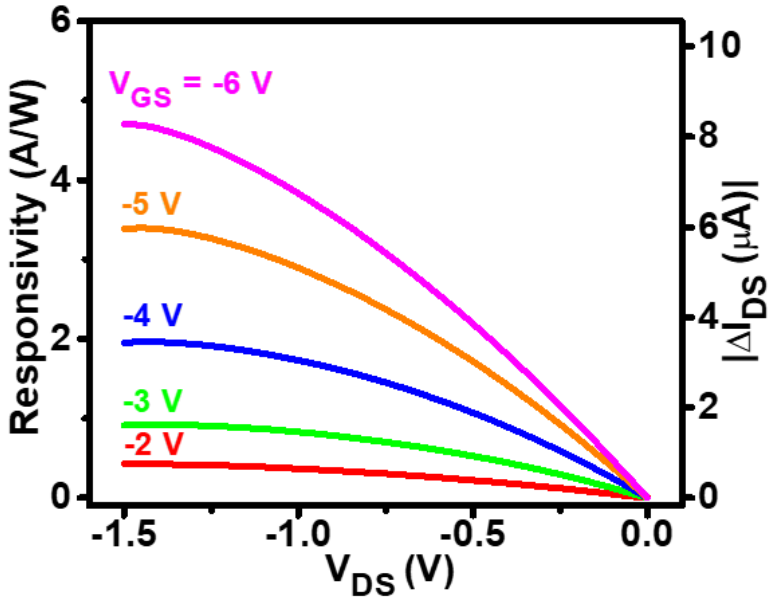


**Figure 2.17:** Photoresponsivity and VDS-IDS curves of the ultra-thin Ge phototransistor under the illumination power density of 140.8 mW/cm2. The peak photoresponsivity is 4.7 A/W.

In contrast, the photogating effect in our developed cavity-manipulated ultra-thin nanomembrane phototransistor is majorly due to the high optical absorption and corresponding photo generated carriers confined within the ultra-thin Ge films, rather than the trap states. The high absorption at the desired wavelength can be precisely controlled by tuning the thickness of either Ge or $Al_2O_3$ layers. The absorbed photons generate carriers confined in the Ge channel, and therefore, resulting in the improved photoconductivity. To reveal the photo gating effect quantitatively (i.e., $|\Delta I_{DS}| = |G_m| \times \Delta V_{TH}$[68], where $\Delta V_{TH}$ is the photon-induced change of the threshold voltage), we then analyze the relation of the photo current, $|\Delta I_{DS}|$, with the device trans-conductance $|G_m|$, ($|G_m| = |\partial I_{DS}/\partial V_{GS}|$) which can be extracted from Fig.2.17 as shown in the lower panel of Fig.2.18. In this experiment, we swept the gate voltage $V_{GS}$ under $V_{DS}$ at -1 V, and extracted $|\Delta I_{DS}|$ resulted from $\Delta V_{TH}$ under different optical illumination conditions, as shown by the curves in the upper panel of Fig.2.18. One can see that these $|\Delta I_{DS}|$-$V_{GS}$

curves are consistent with the $|G_m|$-$V_{GS}$ curve, confirming that the gate controlled photo current results from the photo gating effect[68].

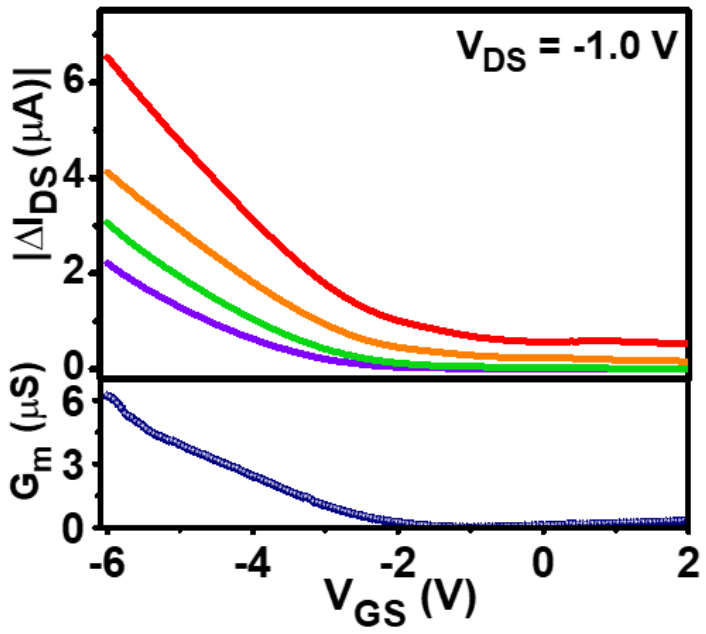


**Figure 2.18:** (Upper panel) Ultrathin Ge transistor photocurrent (|ΔIDS|) as a function of VGS under various power conditions: 3.36 mW/cm2 (purple), 20.8 mW/cm2 (green), 140.8 mW/cm2 (orange) and 343.2 mW/cm2 (red), respectively. (Lower panel) Trans-conductance (|Gm|) of ultrathin Ge transistors.

In addition, the photo gating effect expression (i.e., $|\Delta I_{DS}| = |G_m| \times \Delta V_{TH}$) shows that with a given $V_{GS}$, a bigger change of threshold voltage, $\Delta V_{TH}$, leads to a larger photo current, $|\Delta I_{DS}|$. To compare our device with a typical phototransistor based on epitaxial-grown high-quality III-V materials with similar photo gating effects, which does not rely on trap states either), we extracted the $\Delta V_{TH}$ of both devices in Fig.2.19. One can see that the $\Delta V_{TH}$ of our single crystalline Ge-membrane-based device (red dots) are three orders of magnitude larger than those of the III-V phototransistors (blue dots). According to the empirical equation to describe the photo-gating-induced $\Delta V_{TH}$ (i.e., $\Delta V_{TH}=(nkT/q) \times \ln[1+(\eta q P_{inc})/(I_{dark} h\upsilon)]$), one can relates the incident power ($P_{inc}$) with $\Delta V_{TH}$, as shown by the red curve in Fig.2.19. Here, n is an empirical constant for

fitting (n=8.94 obtained by the least squares method), k is the Boltzmann constant (1.38×10-23 J/K), T is the temperature (300 K), h is the Planck constant (6.63×10-34 J·s) and υ is the frequency of light (4.09×1014 Hz, corresponding to 733 nm). The excellent fitting confirms that the large $\Delta V_{TH}$ is contributed by the strong absorption (η) due to the nanocavity, and the effective suppression of dark current ($I_{dark}$) owing to the ultrathin Ge channel. As a result, the ultra-thin-Ge-based phototransistor can generate a stronger signal than traditional III-V based device with a similar trans-conductance. This enhanced photocurrent holds promise in improving the performance of thin film photodetectors, especially as pixels of sensor arrays and imagers are increasingly miniaturized[69]. Intriguingly, the absorption enhancement resonance can be manipulated by controlling the nanocavity structure, which will enable the development of new multi-spectral sensing on the same chip.

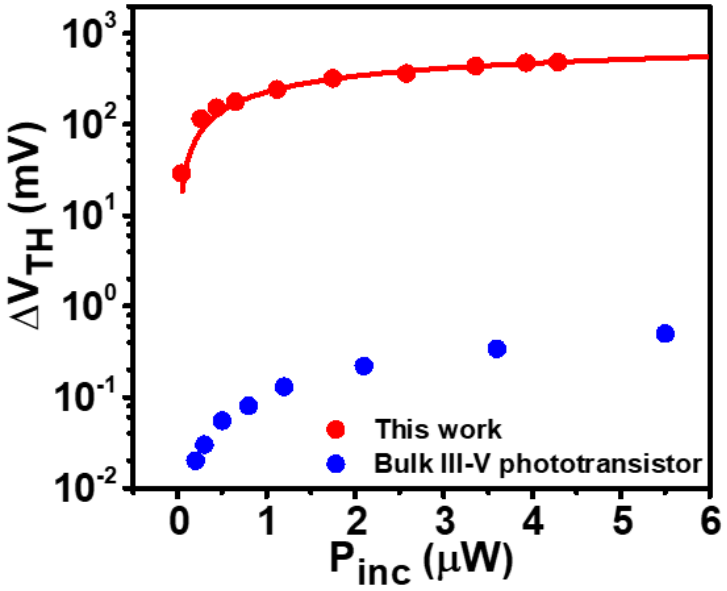


**Figure 2.19:** Comparison of threshold voltage change ($\Delta V_{TH}$) of the ultrathin Ge phototransistor with that of the epitaxial based III-V phototransistor. The measured $\Delta V_{TH}$ values are obtained by subtracting the threshold voltages extracted from the $V_{GS}$-$I_{DS}$ curves under the illuminated and the dark conditions.

The solid curve is plotted using the empirical equation for $\Delta V_{TH}$.

## 2.7 Conclusion

In summary, we developed a nanocavity-enhanced single-crystalline Ge nanomembrane photodetector. The fabrication processes successfully thinned down the Ge films to as thin as 10 nm and maintained the single-crystal material quality of nanomembranes. The photoresponsivity could reach up to 4.7 A/W, resulting from the enhanced absorption and gate modulation. Due to the significantly reduced volume of the active material, the dark current was reduced significantly. Along with the increased photocurrent due to the enhanced optical absorption within Ge nanomembranes, the NPDR as high as ~$10^5$ $mW^{-1}$ was realized. The NPDR of our device also exhibited a better stability under stronger incident power than that of 2D material devices, mainly due to the great material quality of the single crystalline Ge nanomembranes. Furthermore, by characterizing the gate-controlled performance, the device physics of this ultra-thin film photodetector were analyzed showing obvious photo gating effect. The enhanced absorpiton and confinement of the carriers lead to a large change of threshold voltage and thus enhanced photoconductivity. By integrating the Ge membranes (10 ~ 30 nm) with predesigned nanocavities, we demonstrated spectrally tunable thin-film phototransistors. Importantly, due to the CMOS compatible processes, the proposed single-crystal Ge memebrane ultra-thin-film transistors can be fabricated over large scale (e.g. wafer scale), which is superior over current 2D-material-based optoelectronic devices and can be a competivite building block for the next generation functional electronic/optoelectronic circuit.

# 3 Broadband spectrometers based on single crystalline semiconductor nano-membrane

## 3.1 Introduction

These days the hyper-spectral imager is playing more and more important roles for professional imaging purposes such as terrain inspection, industrial/agricultural product examination, security inspection as well as identifying materials for proper trash disposal. What the hyper-spectral imaging differs from the visible light imaging is the hyper-spectral imaging covers broader band wavelength of electromagnetism spectrum so it can tell more chemicals across the electromagnetism spectrum. The structure of the hyper-spectral imaging is mainly composed of light entrance slit, the collimating lens, the newton light prism as well as the photo sensing array for imaging reconstruction. The key structure for hyper-spectral imaging is the newton light prism. As Sir. Isaac Newton invented this light prism in 1672, this light prism structure is still being widely used in the area of hyper-spectral imaging. The principle of the light prism is based on conventional ray optics, since different wavelength of light has different values of refractive index in one material, the refracted light angle is different. Therefore, the refracted light from the light prism can travel to free space in different angles and is shown as different colors. However, the light prism is too bulky, making the hyper-spectral imager device heavy and big, which limits this application to today's smart phone or other portable devices. Therefore, it is necessary to reinvent the light prism to make the device compact and portable.

The function of spectrometer is achieved by the combination of grayscale optical cavity and group IV semiconductor nanomembranes. Group IV semiconductor nanomembrane such as silicon and germanium membrane are defined as 2D array of photon sensing pixels and integrated on the same optical cavity. Since the optical cavity is composed of the light reflector, the gradient thickness of optical spacer and the gradient thickness of the anti-reflective coating layer, each photon sensing pixel has its own unique photo response fingerprint over the spectrum (from 400 nm to 1600nm). We demonstrate by integrating 100 silicon photon sensing pixels and 100 germanium photon sensing pixels on the optical cavity, since silicon has high detection efficiency over the visible wavelength[19] and germanium has high detection efficiency[70,71] over the near infrared wavelength, we can recover both the visible and near infrared spectrum in the same chip.

## 3.2 Device design and the fabrication design of the spectrometer

Fig.3.1 shows the detailed structure of the spectrometer and the optical image of the finished spectrometer, which is composed of silicon handling substrate, the silver light reflector, $Al_2O_3$ optical spacer layer, silicon and germanium membrane photon sensing pixel and $Al_2O_3$ antireflective coatings. We employed the grayscale deposition to deposit the optical spacer layer with gradient thickness along the vertical direction (shown as the red dashed line). Therefore, along the vertical direction, every photon sensing pixel has its unique photon response over the spectrum (400 nm – 1600 nm).

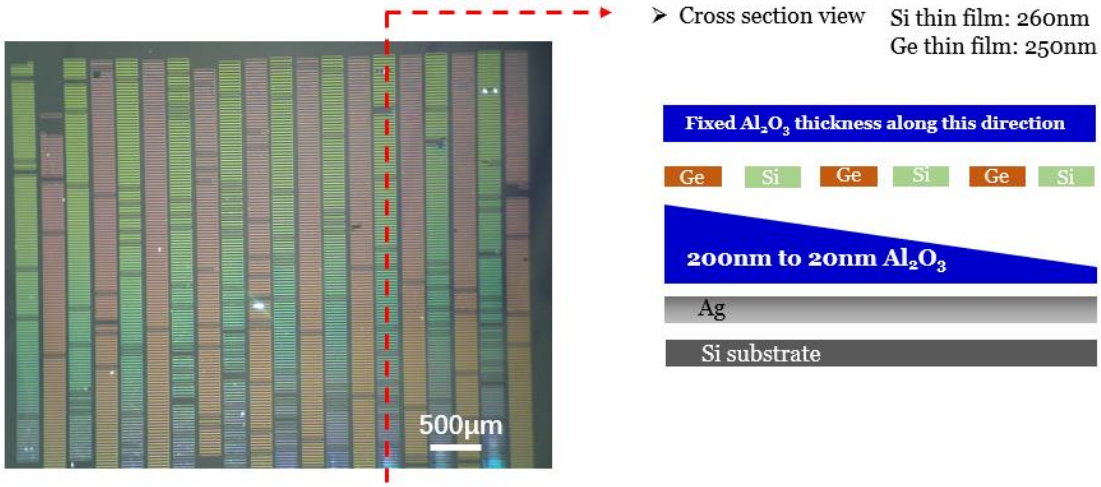


**Figure 3.1:** Optical image of fabricated spectrometer and its cross-section view along the vertical direction.

We further designed the anti-reflective coatings to be a gradient layer. Fig.3.1 shows the detailed structure of the spectrometer. Along the horizontal direction shown in the figure, the anti-reflective coating layer is designed to be grayscale, which means the spectrum photo response of the pixel along horizontal direction is also different. To conclude, our design makes the spectrum response of each pixel on the cavity be unique.

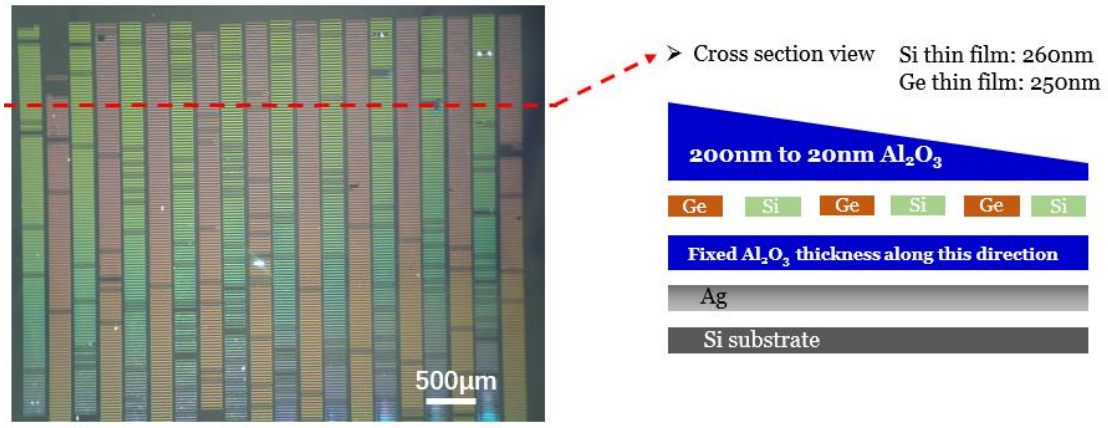


**Figure 3.2:** Optical image of fabricated spectrometer and its cross-section view along the horizontal direction.

## 3.3 Fabrication process of the spectrometer

The fabrication method used in this work is termed as grayscale deposition. Similar demonstration has been shown previously by Kats et al[72]. We used the dielectric

evaporator as the tool to do the grayscale deposition, other deposition tool such as magnetron sputter or chemical vapor deposition also can be used for the grayscale deposition. Fig.3.3 shows the schematic view of this deposition method. Between the depositing source and the sample, a shadow mask is designed, in order to block part line-of-sight of the evaporated materials. Therefore, the partially blocked area has different deposition rate, and this deposition rate changes gradually from the center part of the sample to the rim part of the sample.

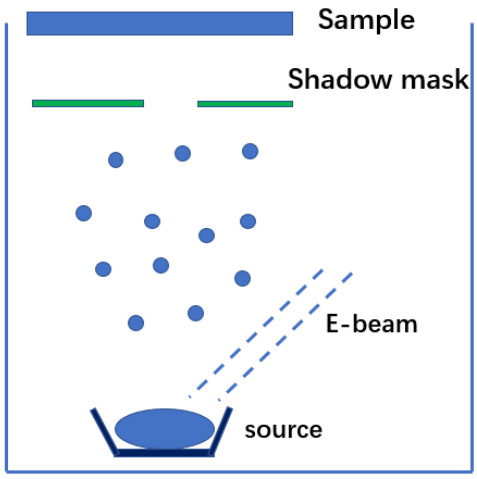


**Figure 3.3:** Schematic diagram of the grayscale deposition method.

By using this fabrication method, we can fabricate the dielectric thin film with gradient thickness. To demonstrate the gradient thickness, we use the germanium as the source material and deposit the germanium thin film onto the pre-designed cavity. Fig.3.4 shows the deposited result. By changing the distance between shadow mask and the deposited sample, the gradient region can be tuned.

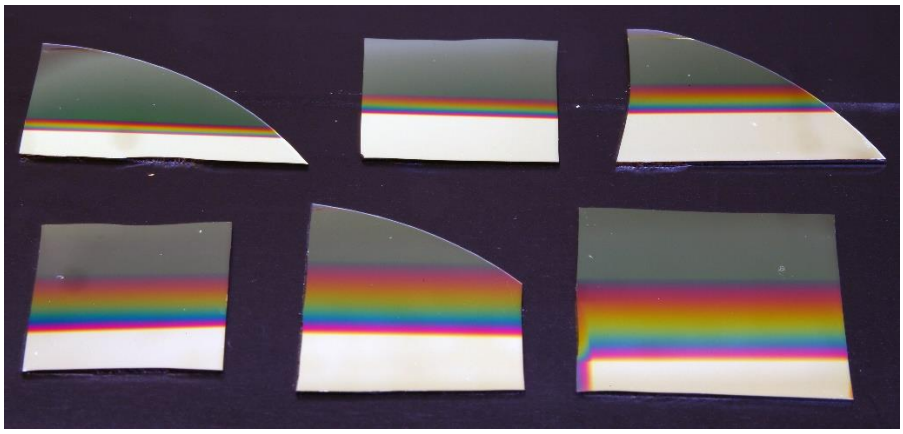

**Figure 3.4:** Photo image of the gradient germanium thin film on pre-designed optical cavity

## 3.4 Optoelectronic characterization of the spectrometer

The characterization results of the silicon and germanium pixel are shown in Fig.3.5 – 3.7. The characterization includes photo responsivity and spectrum responses. Because of the optical cavity design, every pixel has different photo response peak in different wavelength region and shows very weak photo responses if the light signal does not contain the corresponding wavelength.

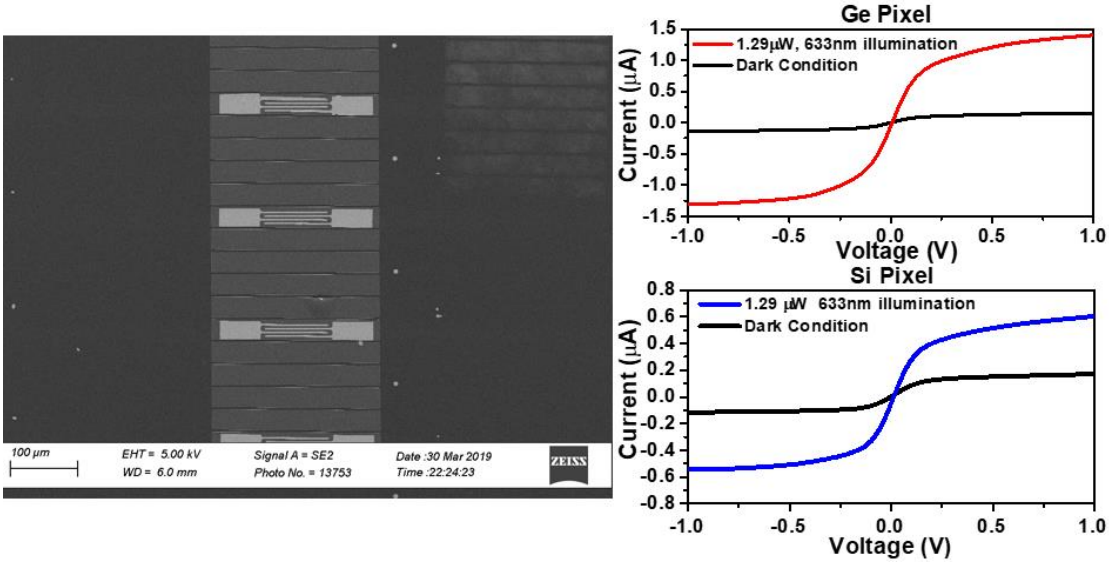


**Figure 3.5:** SEM image of the sample pixel on optical cavity and the current-voltage performance under both dark condition and the light condition.

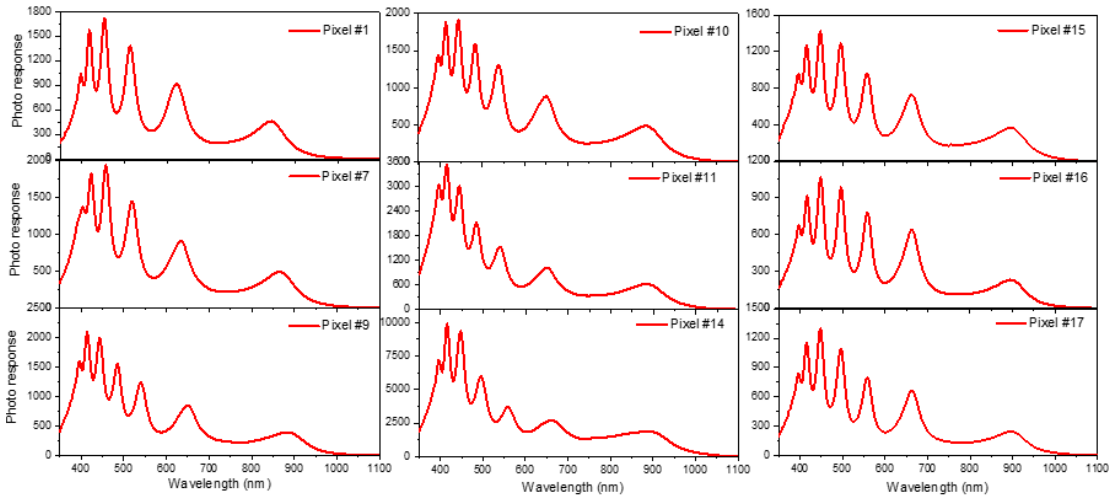


**Figure 3.6:** Spectrum response of nine silicon pixels.

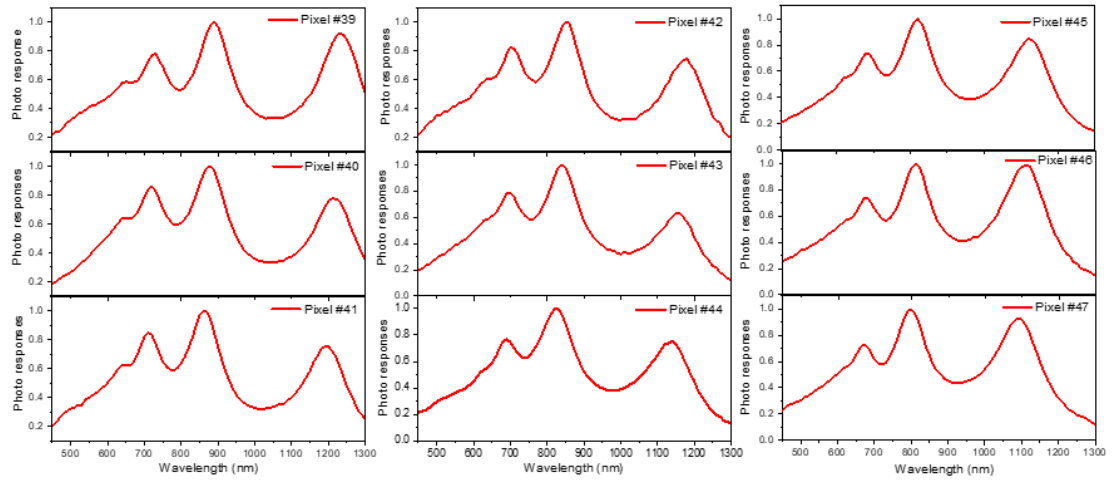


**Figure 3.7:** Spectrum response of nine germanium pixel.

## 3.5 Detailed spectrometer performance characterization

After the pixel characterization, the spectrometer can be used for the signal spectrum recovery. Fig.3.8 shows the spectrum recovery results of our spectrometer. As arbitrary light signal incident on the spectrometer, each pixel has its own photo responses. The photo responses can be collected by the read-out circuit and analyzed by the spectrum recovery algorithm. As shown in Fig.3.8, when the photo current from more pixels is collected, higher resolution of the spectrum recovery can be achieved.

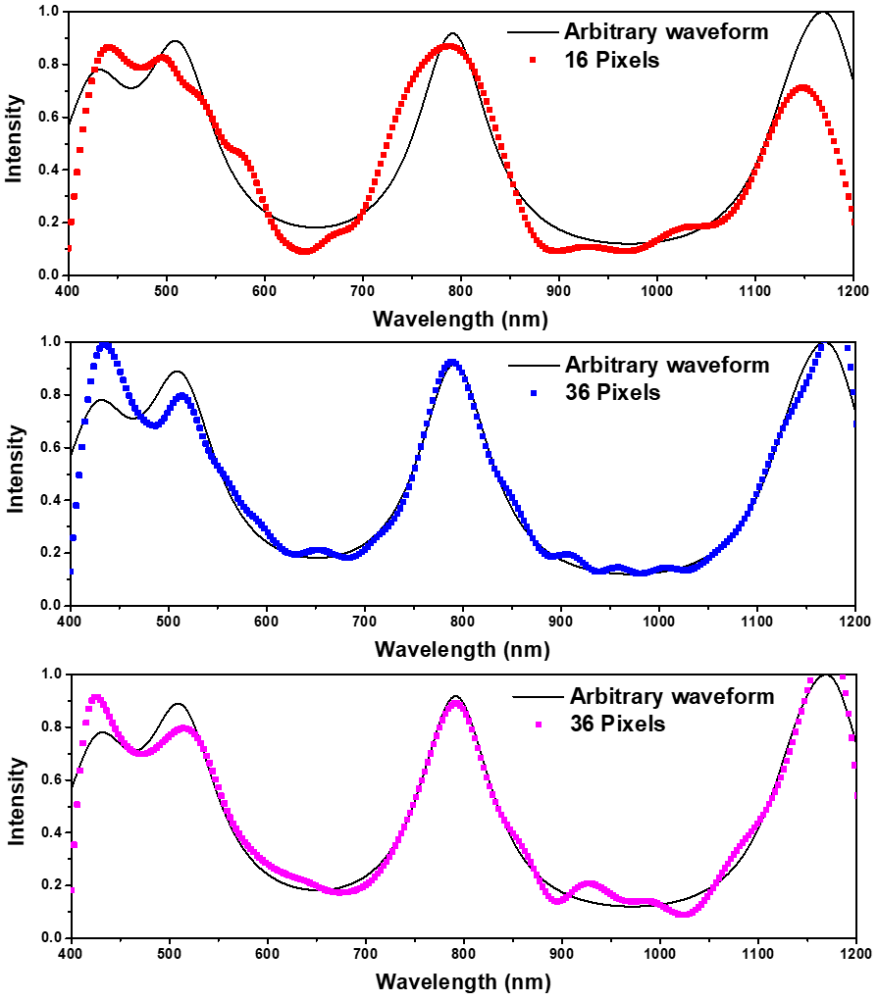


**Figure 3.8:** Spectrum recovery results of an arbitrary waveform

## 3.6 Conclusion

The existing spectrometer is bulky, expensive and heavy (our lab spectrometer is over 45lbs in Prof. Zongfu Yu's lab, equipment cost is over $5000), since it is based on traditional geometric optics. Our invention is based on the light-matter interaction at nanometer scale, and the device can be fabricated using CMOS compatible method. Therefore, our invention has the advantage of light weight, portable and very cost competitive compared to the traditional spectrometer. Our portable spectrometer can also read the signal and the recover the signal spectrum

in the timing order of several seconds, while the traditional spectrometer is very slow (in about 5 minutes from 400nm to 1600nm). To conclude, the spectrometer we invented can outperform the traditional one and offer a big cost advantage.

# 4 High performance flexible ultra-violet/visible single photon detector based on epitaxial single crystalline silicon membrane

## 4.1 Introduction

Ultra-violet (UV) photodetectors have broad applications in many areas such as scintillator light detection[73–76], time correlated photo detection[77–79], ultra-fast fluorescent microscopy detection[80,81] and ultra-dense spatial imaging[82,83]. Particularly, photodiodes with close to unity internal quantum efficiencies (IQE) are highly desired[24,84]. However, there exists various challenges in the current fabrication process to develop such a device. The penetration depth of UV light is typically only a few nanometers. As a result, the doping profile and the electric field in the few nanometer ranges of photo detection devices become very critical. Traditional UV photodetectors usually adopt a constant doping profile near the semiconductor surface, resulting in a negligible electric field, which limits the photo-generated carrier collection efficiency of the photodetector. Ion implantation becomes incapable of precisely controlling the doping profile within such a thickness range. An alternative doping technique is spin-on-doping. However, this technique leads to so-called “dead regions” at the surface of the photodiode since the p-n junction formed by this method is still too thick and the built-in electric field near the surface is negligible, thus making the transit time of the photo-generated carriers extremely large. One interesting solution is to use an induced junction to make the surface electric field very large (close to $1\times10^5$ V/cm at the

surface[24]. However, the stability of photodiode using the induced junction method is a critical issue, as UV radiation could break bonds at the oxide/Si interface, increasing the surface state density and thus neutralize the inversion-based electric field layer. Therefore, in order to enhance UV light detection efficiency, a special doping design is required to enhance carrier collection efficiency within the tens of nanometers of surface depth where the majority of UV light is absorbed.

In this section, we present our study on the development of boron gradient doping during epi-growth of crystalline silicon. The boron gradient doping technique can also be applied to the thin film based devices by replacing the bulk silicon material with the SOI wafer. By using a combination of gases ($SiH_4/PH_3/H_2$ and $SiH_4/B_2H_6/H_2$), we were able to directly grow high quality p+-i-n junctions without any subsequent doping process. By adopting the gradient doping method, a built-in electric field near the surface can be generated, which facilitates carrier separation and drift into the p and n regions for holes and electrons, respectively. The p+-i-n junction is characterized with different methods including secondary ion mass spectroscopy (SIMS), current-voltage (I-V) measurements, and capacitance-voltage (CV) measurements. By further measuring the spectral responsivity of the devices, we showed that the responsivity of the device can be improved by optimization of the gradient doping method. We further demonstrate that the photodiode can be used in avalanche mode with a gain of about 2800 under the reverse bias of -10.6 V. Also, the sub-pico-farad junction capacitance provides the avalanche photodiode potential as a single photon detector with an ultra-

small timing jitter.

## 4.2 Device design and fabrication process

The grown samples were fabricated into diodes. Fig.4.1(a)-(e) illustrates the photodiode fabrication process flow, where a mesa process was used. Fig.4.1(f) shows the tilted scanning electron microscope (SEM) image of the fabricated photodiode. In this work, we focused mainly on the design of the top ultrathin p-type region of the device (Fig.4.1(g)), because the penetration depth of UV light (200 nm to 300 nm) is only about 10 nm[85]. The design was aimed to generate a strong built-in electric field in this region. Previously, others have demonstrated $B_2H_6$-based chemical vapor deposition (CVD) capable of controlling the boron doping thickness down to 2 nm[86]. However, much of the work was performed using low temperature growth (i.e. below 700°C), and the composition of the epi-layer was too complicated to be analyzed, since the $B_2H_6$ gas would decompose and form an α-boron layer. The metallic-like α-boron layer becomes very difficult to remove[87], jeopardizing the subsequent fabrication process of the photodiode. Therefore, we improved the recipe by increasing the growth temperature to 900°C. Several publications[88–90] showed that, under such a high temperature, $B_2H_6$ gas is thermodynamically unstable and would decompose to $BH_3$, which acts as a precursor to react with the hydrogen bonded silicon surface (H-Si) by chemisorption. The $BH_3$ and H-Si can form $H_2B$-Si in this process. After the chemisorption process, the hydrogen will be released as gas and the boron can diffuse into silicon as an active dopant. The other two parameters affecting the doping profile

are the concentration of $B_2H_6$ gas and the doping time. Previous work by Kiyota et al[91] showed that if the $B_2H_6$ gas concentration exceeded 1 parts per million (ppm), the boron segregated on the surface and became electrically inactive, causing α-boron residue formation after epi-growth. Thus, we kept the $B_2H_6$ gas concentration at 1ppm. In our previous work, we have reported that under such a low $B_2H_6$ gas concentration condition, the control of doping time affects the boron doping profile more than the control of the doping gas concentration. Thus, we maintained the boron doping temperature at 900°C and directed our focus toward the control of the doping time (from seconds to minutes). In conclusion of the doping recipe, we controlled the CVD furnace at a temperature of 900°C and a pressure of 100 Torr. The $H_2$ gas flow was 30 slm (standard liter per minute). The $B_2H_6/H_2$ gas flow rate was 205 sccm (standard cubic centimeters per minute), in which the $B_2H_6$ flow rate was diluted down to 0.05 sccm, the rest were H2 carrier gas. We fabricated three types of samples that were grown under a doping time of 15 seconds, 30 seconds, and 60 seconds, respectively.

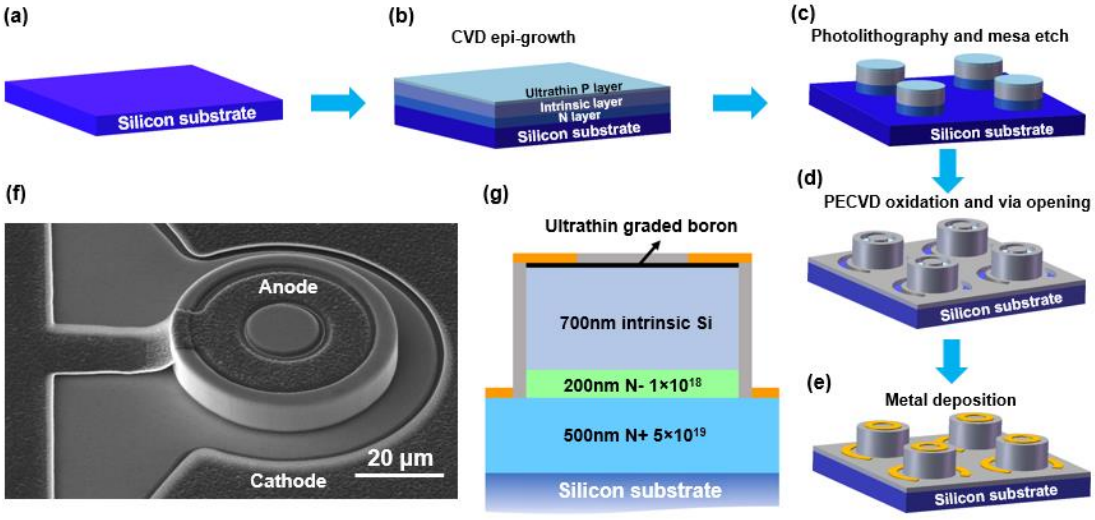


**Figure 4.1:** Fabrication flow of the p+-i-n photodiode with mesa-defined process. (a) Beginning with a

silicon substrate. (b) Growth of the boron gradient doping epitaxial layer using chemical vapor deposition. (c) Photolithography patterning and mesa etching to define active devices. (d) Plasma enhanced chemical vapor deposition (PECVD) oxidation for passivation and via opening, the SiO2 layer has a thickness of 127nm. (e) Metallization to complete device fabrication. The metal contacts are 70 nm Al/70 nm Au formed by electron beam evaporation. (f) A titled SEM image of the fabricated photodiode sample. (g) Schematic illustration of the p+-i-n photodiode vertical structure with the doping concentrations and thicknesses of each layer.

## 4.3 Ultrathin gradient doping for enhanced ultra-violet photon detection

Fig.4.2 (a) and (b) show a comparison of the electronic band diagrams between with gradient doping (Fig.4.2(b)) and without gradient doping (Fig.4.2(a)). As clearly seen, gradient doping can induce a built-in electric field near the surface and improve the collection efficiency of the photo-generated carriers. We used SIMS to characterize the boron concentration of our sample for different doping times (*i.e.*, 15, 30, and 60 seconds). Fig.4.2(c) shows the doping profile results as expected, which exhibits a dopant concentration with an exponential gradient coefficient of 1.2, since the boron atoms were expected to diffuse into the silicon as they reach the silicon substrate. In order to quantitatively review the gradient-doping-enhanced electric field, we performed the Silvaco$^{TM}$ simulations on the built-in electric field. We reconstructed the device doping profile and metal layout using the simulation code. All simulations were carried out under zero volts bias, since the built-in electric field is the main focus. Fig.4.3 (b) shows the simulated electric field based on the doping profile of Fig.4.2(a). One can clearly see that the electric field of the 15-sec doping sample showed a maximum of $5.88\times10^4$ V/cm, and the 60-sec doping sample showed a minimum of 3600 V/cm at the surface. The enhancement of the electric field for the 15-sec doping time

compared to the 60-sec doping time can be attributed to the elongated Debye length and the gradient doping in the former case. We then investigated the electrical and optical properties of all the photodiodes of the three gradient doping profiles in the following context. All the devices were fabricated using the identical process (as shown in Fig..4.1(a)-(e)) in order to perform head-to-head comparisons in terms of electrical and optical properties.

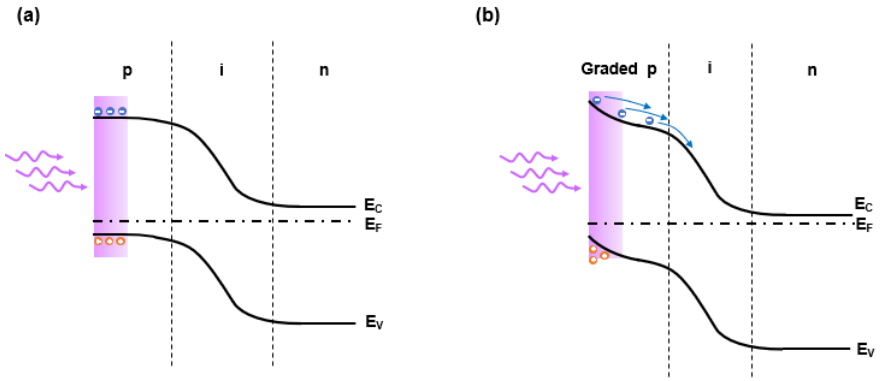


**Figure 4.2:** (a) Electronic band diagram of conventional photodiode without using a gradient doping profile. (b) Electronic band diagram of a photodiode with gradient doping profile (this work).

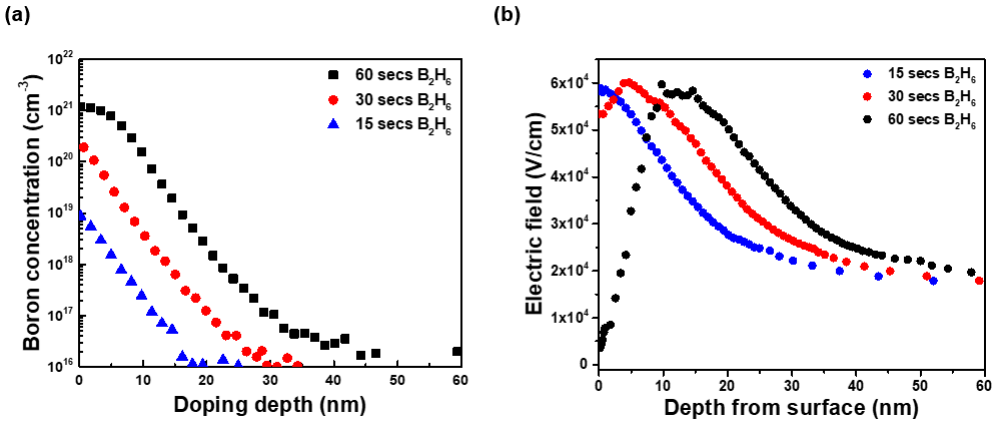


**Figure 4.3:** (a) Boron doping profile of the gradient doping sample characterized by SIMS. (b) Simulated electric field distribution according to the gradient doping profile.

The current-voltage (I-V) curves (shown in Fig 4.4(a)) of these photodiodes all show rectifying characteristics with similar dark current values. Based on the I-V curves, we calculated the ideality factor of the three photodiodes. The ideality factor is defined

as follows: $I = I_0 \exp(\frac{qV}{nkT})$, where the $I_0$ represents the current at zero voltage, $q$ is the elementary charge, $V$ is the voltage value, $k$ is the Boltzmann constant, $T$ is the temperature and $n$ is the ideality factor. When the ideality factor is more close to unity value, the semiconductor junction has lower recombination rate in the junction. The ideality factor can reach ~1.35 when the voltage is at 0.45 V (Fig 4.4(b)), indicating that the diffusion current slightly dominates the Shockley-Read-Hall (SRH) current in the device intrinsic region. As the forward voltage was increased to 1 V, the forward current showed different behaviors in the different diodes. The different behaviors of the diodes can be understood by considering series resistance at higher current levels in the p-n diode. Since the doping conditions are different, the series resistance values of the p+ region vary in the three samples, leading to varied values of the diode forward current. In the case of the 60-sec doping time, it has the highest doping concentration, the smallest series resistance, and thus the highest forward current. It is observed from the I-V curves that a dark current as low as 0.1 nA to 1 nA was obtained at the reverse bias of -8 V. The low dark current indicated that the diode sidewall was well-passivated by the $SiO_2$ layer. We then used an LCR meter to measure the capacitance of the photodiode at 1 MHz frequency. As shown in Fig.4.4(c), at a bias voltage of -8 V, the capacitance of these samples was less than 1pF. Particularly, one can see that the minimum capacitance is about 0.129 pF for the 15-sec $B_2H_6$ doped sample. The low capacitance indicates that the device would operate at a higher speed than the other two devices. The low capacitance is also critical for single-photon detectors, as suggested by Ma et

al[92] that for a low timing jitter (~10 pico-sec) single photon detector, the diode capacitance should be at the sub-pico-farad level.

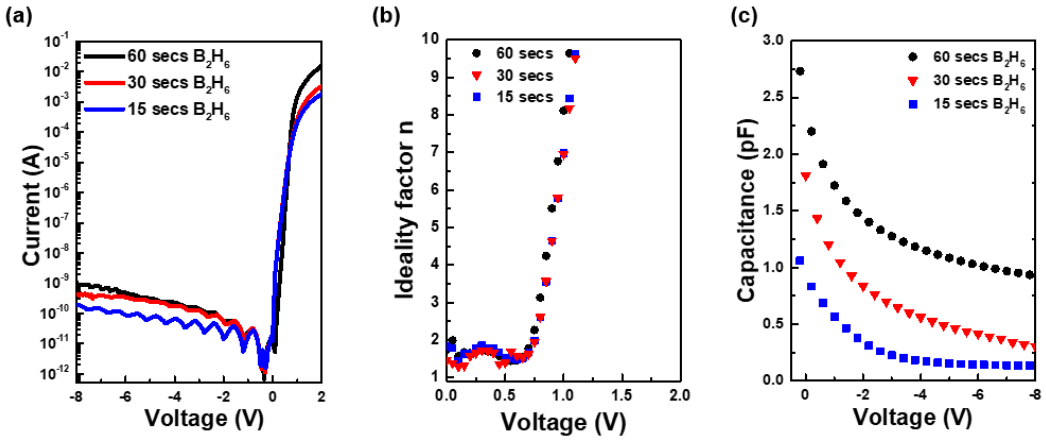


**Figure 4.4:** Electrical characterization of three samples with different doping times. (a) Current-voltage (I-V) characteristics of the photodiode with different growth/doping times. (b) Calculated ideality factor of the photodiode according to the I-V curves from (a). (c) Capacitance-Voltage (CV) characteristics of the photodiode. The measuring frequency was at 1 MHz. All three samples have the same device parameter, the junction diameter is 50μm, the anode contact area is calculated to be 400μm2, and the cathode contact area is calculated to be 926 $\mu m^2$.

We measured the spectral response of the three diodes. The spectral response of the photodiode was performed under zero bias voltage. We used an ASB-XE-175 as the broadband light source and a DK480 1/2 Meter Monochromator to select the corresponding wavelength signal. Fig.4.5 shows the responsivity of the photodiodes with 15-sec, 30-sec, and 60-sec doping. The fundamental responsivity limit of our device was also calculated as shown in Fig.4.5. In our calculation for the fundamental limit of our device, we assumed unity for the devices' internal quantum efficiency (IQE), *i.e.*, all of the absorbed photons that were converted into electron-hole pairs. Then we calculated the absorption spectrum of our devices, which is composed of 127 nm $SiO_2$/300 μm silicon. With the absorption data and a unity IQE, the fundamental responsivity limit (as shown in Fig.4.5) of our photodiode can be calculated using the

equation:

$$R = Absorption \times \eta \times \frac{\lambda_{(\mu m)}}{1.23985(\mu m \times W/A)}$$

Where $R$ represents the photodiode responsivity (A/W), $\eta$ is the IQE (one in the case of fundamental limit), and $\lambda_{(\mu m)}$ is the wavelength of interest.

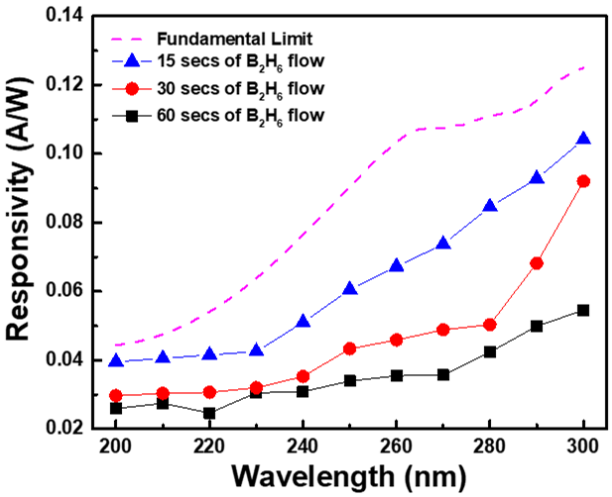


**Figure 4.5:** Measured spectral responsivity of the photodiode with different doping times along with the plot of the fundamental limit of responsivity.

As shown in Fig.4.5, the 15-sec doping sample reached a maximum photo responsivity of 0.1 A/W at the wavelength of 300 nm. Fig.4.5 also shows that the responsivity of the 60-sec doping sample is the lowest among the three devices. Two major reasons were considered that directly attribute to the different responsivities. The first one is that the surface built-in potentials of the three samples vary. As we see from Fig.4.2(b), the surface electric field of the 60-sec doping sample is negligible compared to the other two samples. The close-to-zero electric field contributed no drift velocity of the photocarriers generated at the surface, which can be expressed as $v_{drift} = \pm\mu_{carrier} \times E$, where $v_{drift}$ is the carrier drift velocity; a positive sign (+) is for hole

carriers and a negative sign (-) is for electron carriers; $\mu_{carrier}$ is the carrier mobility, which is a fixed parameter in the given material; and $E$ is the built-in electric field. The small carrier drift velocity increased the carrier transit time, increasing the carrier recombination chance in the drift process. The other reason, as we analyzed, is believed to be from the boron-silicon precipitants on the silicon surface of the two samples (30-sec and 60-sec). Since at the temperature of 900°C, the maximum boron solubility in silicon is believed to be $1\times10^{20}$ $cm^{-3}$, according to the work done by Inada et al[93]. These boron-silicon precipitants can act as surface recombination centers and cause carrier loss when the carriers are in the process of diffusion and collected by the metal electrodes.

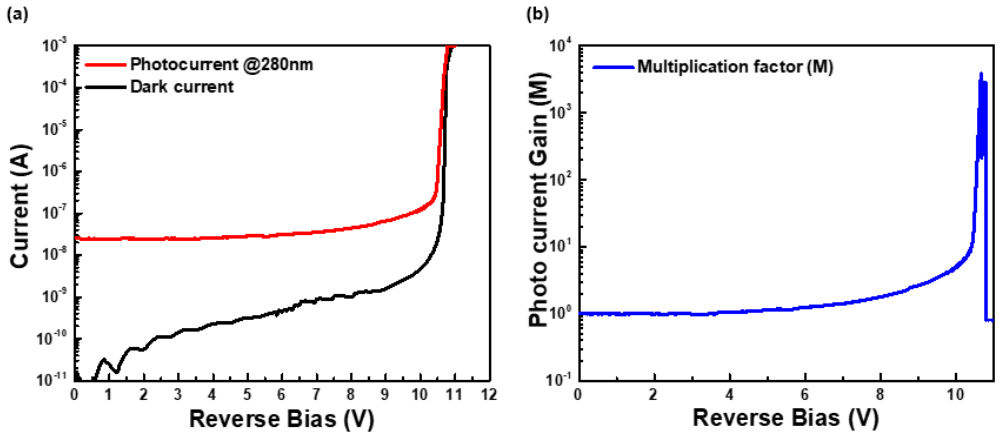


**Figure 4.6:** (a) Measured photocurrent and dark current of the 15-sec doping sample. (b) Calculated multiplication factor (M) of the 15-sec doping sample based on (a).

It is noted that an alternative approach to UV enhanced photodetection by overcoming the issues associated with surface recombination losses was proposed by Kim *et al*. In that approach, a graphene-oxide-silicon (GOS) capacitor structure provides better confinement of photocarriers in a potential well, which is well-passivated by thermally grown $SiO_2$, and is therefore less prone to surface

recombination. The perpendicular configuration for photocarrier separation and transport directions in Si of the GOS structure also allows for wider (thicker) depletion region formation, which would benefit photocarrier generation/separation without compromising the carrier transport and collection efficiency.

In our work, to reduce the surface recombination, we reduced the boron doping time to 15-sec. The SIMS data indicated the boron concentration was reduced down to $8.6\times10^{18}/cm^3$. At this concentration, the boron-silicon precipitants are believed to be reduced greatly compared to the 30-sec and 60-sec doping samples. Consequently, the responsivity of the 15s sample was greatly enhanced, confirming that the optimized gradient doping method can enhance the collection efficiency of the photo-generated carriers. Further enhancements could be made, for example, by using multiple layers of anti-reflection coatings.

Because the 15-sec doping sample proved to be optimal, we specifically chose it to test the avalanche properties of the photodiode. As shown in the Fig.4.4(a), the I-V measurements in the dark and under UV light (280 nm) conditions were performed. When a voltage of -10.6 V was applied, a photo current avalanche gain was observed, as shown in Fig.4.6. The photo-current gain of the sample reached about 2800 at a reverse voltage of -10.8 V. After that, the photo-current gain was no longer a good indicator for avalanche gain as the maximum current was limited to 1 mA due to the measurement setup. This avalanche effect can serve as an avalanche photodiode to detect and amplify the light signal, in which the gain is fixed. Or, the device can also

be combined with an active quenching circuit to work in the Geiger mode as a single photon detector.

## 4.4 Flexible single photon detector fabrication process

From the above discussions, we can conclude that the ultrathin gradient doping could enhance the silicon p-i-n photodiode detection efficiency in the ultra-violet wavelength range. The above devices are fabricated in the bulky silicon substrate. To make the device into a flexible one, we change the substrate from bulk silicon substrate to silicon-on-insulator substrate for releasing the device from the substrate. The flexible single photon detector has many applications including biomedical imaging or implantable bio-fluorescence sensing. However, flexible devices are thin film based, and the devices area are directly exposed to outer environment, which can be affected by the outer temperature changes easily. One known drawback underlying both avalanche photodiode (APD) and SPAD is that the breakdown voltage of the devices has a strong dependence on temperature, which is related to phonon scattering during photo-generated-carriers acceleration/multiplication[94]. The drawback hinders the applications of flexible SPADs where temperature change is inevitable, such as temperature fluctuations of living body/tissues. Therefore, reducing the temperature-induced breakdown voltage fluctuation becomes an important issue for flexible SPADs to function under temperature-varying environments.

In this work, we report Si SPADs with reduced temperature sensitivity of avalanche breakdown voltage by employing a very thin intrinsic region thickness (120

nm) in the SPADs. With the thin intrinsic region, photo-generated carriers in our SPADs would experience less phonon scattering during the process of carrier acceleration/multiplication in comparison to SPADs with a junction thickness on the order of tens of micron-meters[94]. For direct comparison, a temperature coefficient $C_{bd}$, defined as the ratio between breakdown voltage change and temperature change, is used to quantify the temperature sensitivity of avalanche breakdown voltage of SPADs. Our SPADs show a $C_{bd}$ of 2.8 mV/K, which is lower than the lowest reported value of $C_{bd}$ of 5.7 mV/K[95] measured from a Si-based SPAD. We also characterized single photon detection efficiency (PDE) of our SPADs under different temperatures. By operating the flexible SPADs in the Geiger mode, our flexible SPAD shows less temperature dependence of PDE in comparison to the rigid Si based SPAD having a thicker intrinsic region[29].

Beginning with a silicon-on-insulator (SOI) wafer, which consists of a 500 μm thick Si handling substrate, a 250 nm thick buried oxide (BOX, $SiO_2$) layer, and a 200 nm thick p- silicon template layer, low-temperature chemical vapor deposition (LPCVD) was used to grow the p-i-n structure on the SOI substrate. The finished layer structure, including the epitaxy and the SOI layers, is shown in Fig 4.7(a). During the epitaxy growth, diborane ($B_2H_6$) and phosphorene ($PH_3$) were used for p-type dopant and n-type dopant, respectively. In order to achieve high photon detection sensitivity in the UV wavelength range, an ultrathin boron-doped layer (20 nm) with a graded doping concentration was employed during the material growth process, following the same

method that was shown in our previous work[96]. To realize low temperature sensitivity of avalanche breakdown voltage, we designed the intrinsic layer to be around 120 nm (Fig.4.7(a)).

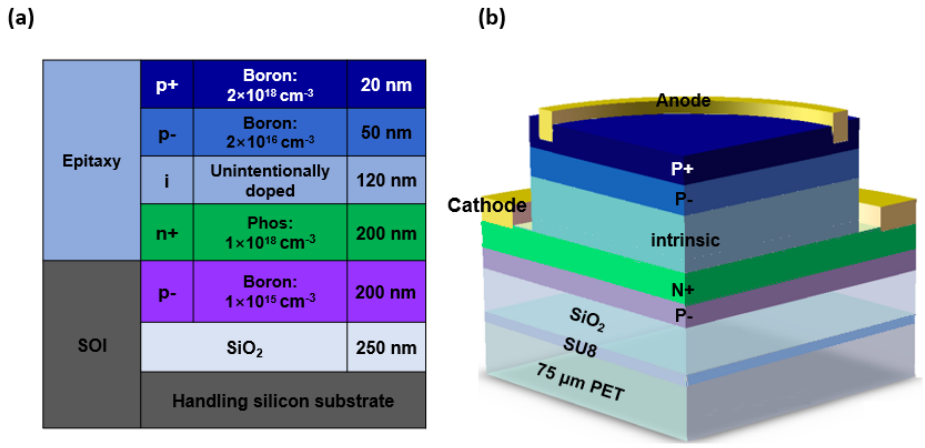


**Figure 4.7:** (a) Illustration of epitaxially grown SPAD layer structure on SOI. (b) A schematic view of fabricated SPAD on a flexible PET substrate.

The p-i-n structure was fabricated into diode array on the SOI substrate first. The finished diodes array was then released by under cutting the BOX using hydrofluoric acid and transferred to a flexible polyethylene terephthalate (PET) substrate. The schematics of the final flexible SPAD sitting on the PET substrate is shown in Fig.4.7(b). It is noted that the sidewall etching of the SPADs with minimum surface damage is critical in realizing low leakage current under reverse bias for SPADs. To minimize sidewall damage, cryogenic inductively coupled plasma (ICP) etching (Applied Materials Precision 5000 Etcher) with NF3/O2 gas was used for SPAD mesa definition[97]. Fig.4.8(c) show a scanning electron microscopic image of the sidewall of the SPADs realized by the etching. After finishing the dry etching, thermal oxidation to form 120 nm thick $SiO_2$ was followed for device surface passivation. Via holes were opened on the thermal oxide and magnetron sputtering (Ti/Al) was used for forming

metal electrodes.

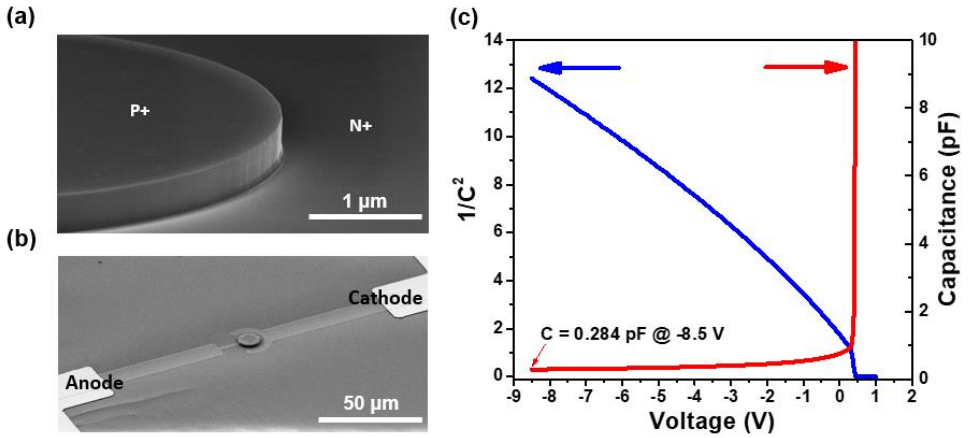


**Figure 4.8:** (a) A scanning electron microscope (SEM) image of the sidewall of a mesa-type SPAD formed by cryogenic dry etching. (b) A tilted SEM image of an SPAD on a PET substrate. (c) Measured capacitance-voltage (C-V) characteristics of the SPAD p-i-n junction.

To release the rigid SPAD array, the fabricated SPAD array on SOI was protected by wax and mounted top side down on a polydimethylsiloxane (PDMS) stamp. Most of the silicon handling substrate was removed by mechanical grinding (about 450 µm thick) and the remaining substrate material (about 50 µm thick Si) was removed by $XeF_2$ etching. The $XeF_2$ etching rate was about 5 µm/min and the etching stopped at the BOX layer. To transfer the released SPAD array, a PET substrate of 3 mils thick was treated in an oven under 390 K for three hours to obtain uniform thermal expansion. The backside of the SPAD array was first spin-coated with SU-8 2025. Then the SPAD array was transferred to the thermally treated flexible PET substrate. The SU-8 was cured using soft baking, UV light exposure and finally a hard baking. After the curing process was complete, the device was put into an acetone solution to remove the wax so that the device can be demounted from PDMS. Figure 1(d) shows an SEM image of a flexible SPAD sitting on a PET substrate. The mesa diameter of the device shown in the

figure is 20 μm. Capacitance-voltage (CV) measurements were performed on the SPAD and the results are shown in Fig.4.2 (c). By reverse biasing the device to 8.5 V, close to the breakdown voltage (Vbr = -8.75V), the junction capacitance was measured to be 0.278 pF. From this capacitance value, we estimated the intrinsic layer thickness of the SPADs during operation to be around 115 nm.

The thin thickness of the intrinsic region is critical in order to make the SPAD operate with less sensitivity to temperature variation as mentioned above. With a thin intrinsic region, phonon-scattering is reduced[25]. Therefore, less charge carrier scattering will occur during the carrier acceleration inside the junction. However, the thickness reduction of the intrinsic region has a limit. As the thickness becomes too thin (less than 100 nm), band-to-band tunneling effect starts to dominate in junction breakdown[98], resulting in substantially increased SPAD noise. In this paper, we designed the intrinsic layer thickness of SPAD to be around 120 nm. However, considering the gradual, instead of an abrupt change of doping concentrations from the heavily doped regions to the intrinsic region, the exact thickness of the intrinsic region is difficult to define. Under such a situation, simulations may help design the overall doping profiles of the SPAD in order to obtain optimized device performances.

A finished 5×8 SPAD array on a flexible PET substrate is shown in Fig.4.2(a). The inset of Fig.4.2(a) shows an optical microscopy image of a single SPAD on PET substrate. Fig.4.2(b) shows an optical image of a bent flexible SPAD array under current-voltage measurements. The bending curvature is about 10 mm. To confirm that

our flexible SPADs can operate under bending condition, we measured the current-voltage (I-V) characteristics of the devices under both flat and bent conditions (curvature of 10 mm) under both dark and ambient lighting. Fig.4.9(c) shows the measured dark and photo current characteristics, as well as breakdown characteristics of a SPAD with an anode area of 314 μm$^2$ under flat and bent conditions, respectively. It is observed that the mechanical bending has improved the photo current with slight improvement on the dark current. The photocurrent improvement may be related to the closer distance between the device and the light source (a mounted flashlight with fixed height). While the mechanism of improvement under bending may require detailed studies, the diode is expected to function well for avalanche operation mode as the sharp breakdown characteristics are not changed by bending. As shown, the breakdown voltages under the two conditions remain the same, which is important for the operation of SPADs.

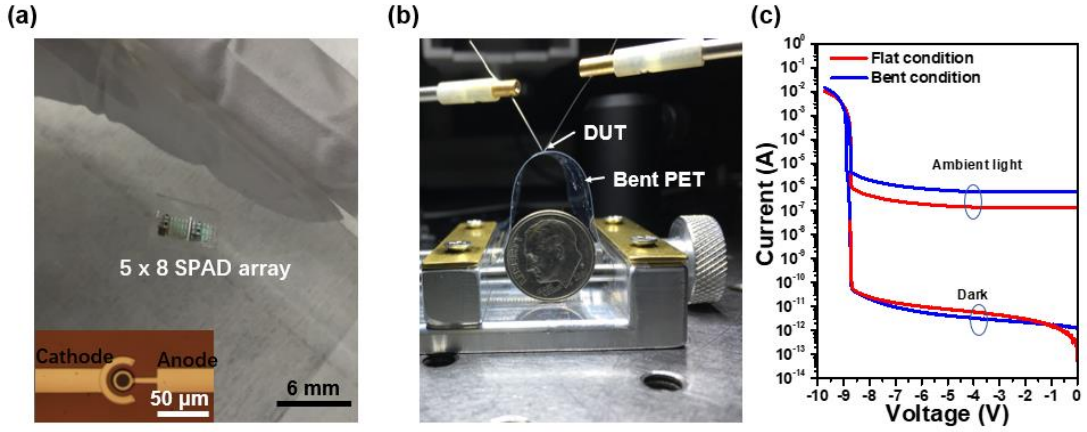


**Figure 4.9:** (a) A photograph of bent 8×5 SPAD array on flexible PET substrate. (b) An optical image of a flexible SPAD array with a bending curvature of 4.5 mm. (c) Measured current-voltage characteristics in dark and ambient light of a flexible SPAD under flat condition and bent condition with a bending curvature of 10 mm. The device's anode area is 314 μm$^2$.

## 4.4 Single photon detection performance characterization

A flexible SPAD with 20 µm diameter anode mesa was used for breakdown voltage measurements at different temperatures ranging from 290 K to 390 K. The breakdown voltage was taken when the reverse current levels reached 90% of the maximum current[95]. Fig 4.10(a) shows the measured current-voltage (I-V) curves under reverse bias. All the I-V curves showed abrupt junction breakdown behavior, with a dark current in the range of 0.1 nA to 10 nA before breakdown occurs. The results indicate that no surface breakdown occurred during the measurements, which is ascribed to the low-damage sidewall etching and thermal oxide passivation. The increasing breakdown voltage with temperature increase (see the inset of Fig 4.10(b)) indicated that the junction breakdown does not originate from the band-to-band tunneling mechanism but from junction avalanche breakdown[99]. From the measured breakdown voltages, $C_{bd} = \Delta V_{bd}/\Delta T$, the ratio between breakdown voltage change ($\Delta V_{bd}$) with temperature change[95] ($\Delta T$), was extracted. The Cbd of our flexible SPAD was calculated to be 2.8 mV/K.

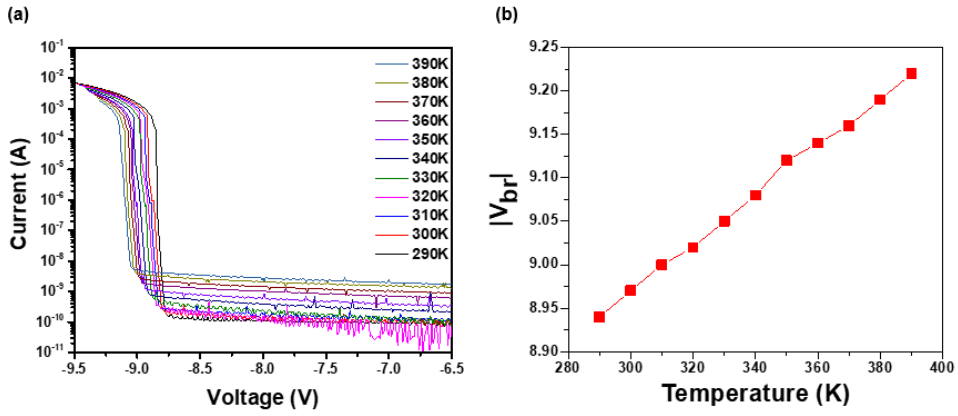


**Figure 4.10:** (a) Measured current-voltage (reverse and breakdown) characteristics of a typical SPAD

under different temperatures. (b) The breakdown voltage values as a function of temperature.

Fig.4.11 shows the comparison of the $C_{bd}$ and dark current density of this work with those of other reported APDs. In order to make a fair comparison, only devices with the similar intrinsic region thicknesses (100 nm to 200 nm) are used for comparison. As shown in Fig.4.11, the best reported GaAs APD[100] shows similar dark current to that of our work. The higher $C_{bd}$ of the GaAs APD than this work is perhaps due to the thick cladding layer (1μm for both and p and n cladding layer) used in the diodes, which inevitably increased the intrinsic region thickness under reverse bias. The reported InAlAs APD25 has the lowest $C_{bd}$, however, with a dark current density five orders of magnitude higher than our device due to the challenge of surface passivation of InAlAs in comparison to Si. In comparison to the $C_{bd}$ (5.7 mV/K) of the latest Si APD counterparts[95], the $C_{bd}$ of our SPAD is lower, along with a lower dark current density than the reported one by two orders of magnitude. The low dark current density of our SPADs is mainly attributed to optimized device mesa etching and surface passivation.

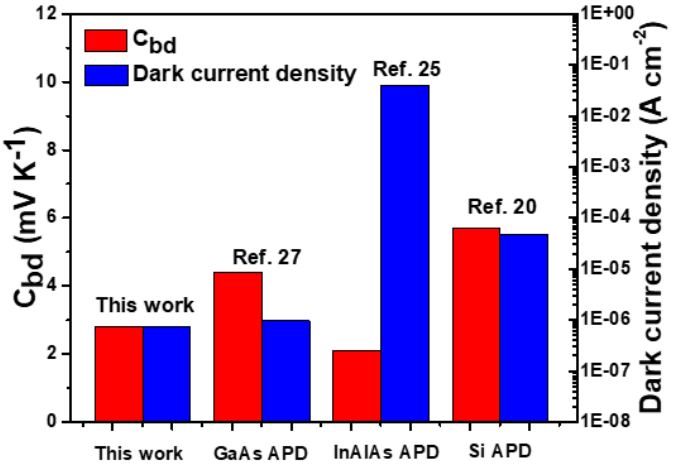


**Figure 4.11:** Comparisons of Cbd and dark current density between this work and previously reported

avalanche photodetectors' performance.

The PDE of the flexible SPADs was further characterized. A photograph of the setup for PDE characterizations is shown in Fig.4.12. In the setup, a laser light with a wavelength of 515 nm from pulsed laser diode was fiber coupled to an integrating sphere. A light splitter was installed inside the integration sphere. To calibrate the output optical power strength from the laser diode, a Keysight 81634B optical power sensor, which is mounted to the integration sphere, was used with a sensitivity of about -110 dBm. The power sensor receives half of the light from the beam splitter. The other half of light from the integration sphere was free space coupled to our testing SPAD. Between the integrating sphere and the testing SPAD, an optical density (OD) filter was used to attenuate the laser light intensity to the single-photon level. The testing SPAD with an anode mesa area of 314 $\mu m^2$ was attached to a home-made printed circuit board (PCB) and wire bonding was used to connect the electrodes of the SPAD to the PCB. During the single photon measurements, the setup was shielded in a dark box. During the measurements, the SPAD was reverse biased to operate in the Geiger mode using a voltage supplier. Since the breakdown voltage of our flexible SPAD is -8.75 V, the DC bias was set at -10 V, or with an excess DC voltage of -1.25V. As shown previously[101–103], higher excess voltage leads to higher single photon PDE, but with a higher dark count. The excess voltage of -1.25 V was set as a trade-off between PDE and dark count.

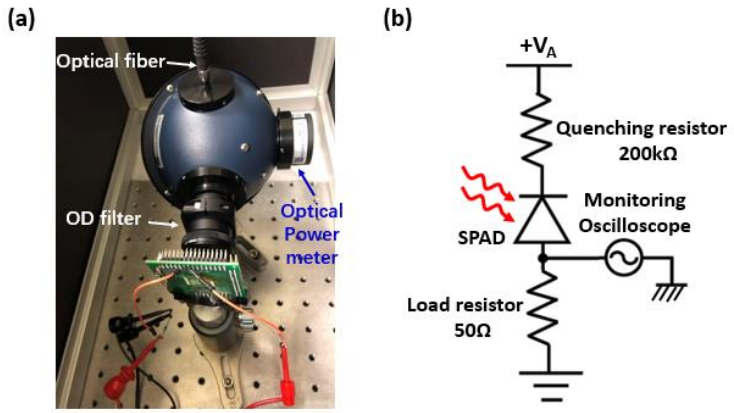


**Figure 4.12:** (a) A photograph of the setup for single-photon detection efficiency measurements. (b) Illustration of the passive quenching circuit used for SPAD measurements.

Fig.4.12(b) shows the passive quenching circuit to reset the flexible SPAD after every triggered event[104]. The quenching circuit (Fig.4.12(b)) is composed of a 200 kΩ quenching resistor and a 50 Ω load resistor. An Agilent DSO91204A oscilloscope was used to monitor the triggered avalanche events. The triggered avalanche pulses were captured and recorded in the oscilloscope, as shown in Fig.4.7(a). In order to record the avalanche pulses triggered by the pulsed laser diode rather than the dark count noise, the pulsed laser diode and oscilloscope were synchronized by an external trigger from the signal generator. The photon detection efficiency (PDE) can then be calculated using PDE = number of triggered events/number of photons, where the number of photons is calculated by the calibrated single photon optical power-meter.

## 4.5 Temperature insensitive on detection efficiency performance characterization and comparison

Fig 4.7(b) shows the measured PDE results of our flexible SPADs at the wavelength of 515 nm at different temperatures. The reason to choose this wavelength is the flexible SPAD has the peak PDE at this wavelength. Since our SPADs have a low

$C_{bd}$, the bias voltage was set a constant value during the measurements at different temperatures. Fig 4.7(b) also shows the PDE of a rigid Si based SPAD at the wavelength of 515 nm with an intrinsic junction thickness around 1 μm (according to the device design) for comparison. Fig 4.7(b) clearly shows the PDE of our flexible Si SPAD has less temperature dependence compared with the thick junction SPAD. The differences between the two SPADs, as shown in Fig.4.13(b), indicate that our SPAD has less breakdown voltage change with the increase of temperature than that in Ref.[29], enabling a less temperature dependent PDE.

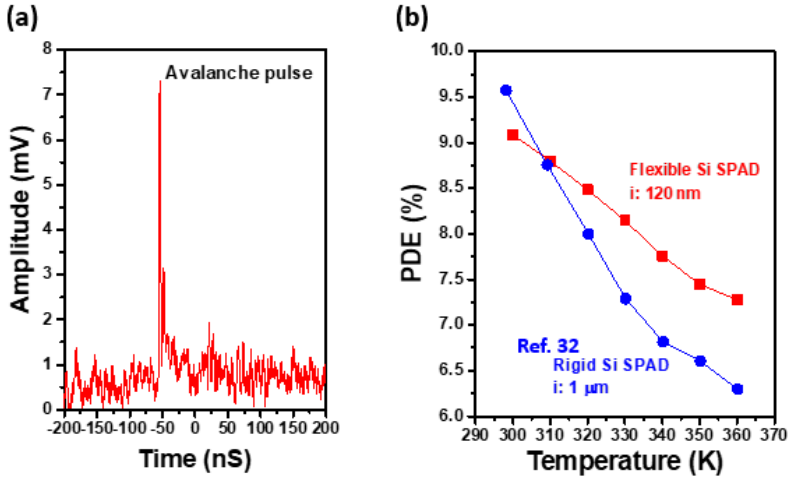


**Figure 4.13:** (a) An avalanche pulse shown in the monitoring oscilloscope. (b) Comparison of PDE results with previous work over the temperature from 290K to 360K.

## 4.6 Conclusion

In summary, we demonstrated a Si SPAD on a flexible substrate. The SPAD exhibits a low fluctuation of avalanche breakdown voltage in response to environment temperature changes due to the implementation of a carefully designed, thin intrinsic avalanche region of the diodes. The flexible SPAD also shows very low dark current density, which is realized with cryogenic dry etching for diode mesa formation and

thermal oxidation for high-quality passivation. Single photon detection efficiency results show that our SPAD has less temperature dependence than a rigid counterpart with a thicker intrinsic region.

# 5 Flexible single photon detector with enhanced near-infrared detection efficiency

## 5.1 Introduction

Flexible photodetectors have become essential parts for many applications, such as implantable fluorescence endoscopes[101,105–107], bio-inspired electronic eye systems[108–110] and retinal prosthese[111,112]. By lifting off thin photodetector layers from the bulk substrate, mechanical constraints from the substrate are eliminated. Thin photodetector layers can be designed and arranged in a three-dimensional geometry to achieve aberration-free imaging[110,113], or can be transferred to flexible substrates to realize biomedical sensing in a living body[107,114,115]. In previous work, photodetectors fabricated from single-crystalline semiconductor membranes have become the most popular choice[116,117]. Compared to the flexible organic material counterparts[118,119], crystalline semiconductor membranes have advantages of higher carrier mobilities and CMOS compatible fabrication process flows, which enable better bandwidth performance and higher production yield[120,121]. However, some organic material like mammalian rod photoreceptor cells have the photon detection sensitivity up to single photon level[122], which promises an alternative to crystalline semiconductor membrane photodetectors. But one inevitable problem from organic single photon detector device is the photo response speed remains low, which is about orders of seconds level. For advanced biomedical sensing techniques such as the time-correlated single photon counting (TCSPC) method[80,123], detecting a single-photon level of light with

picosecond time resolution is necessary for a given detector. Therefore, a thin film based, flexible SPADs with high photon detection efficiency and small timing jitter need to be developed.

This work presents a flexible SPAD with enhanced detection efficiency. To enhance the detection efficiency, we fabricated light-trapping, inverted-pyramid structures on the mesa-type SPADs, which boost the absorption and the EQE over the 750 ~ 1050 nm wavelength range. The EQE enhancement is equivalent to single-pass light EQE through 20 μm of silicon. Compared with the 20 μm diameter SPAD on the SOI rigid substrate we reported in previous work[124], the flexible SPAD under BSI detection method shows enhanced detection efficiency due to higher fill factor. To test the effect of light-trapping nanostructure on the timing jitter performance, various diameters of flexible SPAD was fabricated and tested, ranging from 20 μm to 200 μm. It is found with the light-trapping nanostructure, the flexible SPAD with 20 μm diameter mesa has the best timing jitter performance, which is 85 ps. Finally, we demonstrated that our flexible SPAD can work normally when the device is under the bending curvature of 2.5 mm. Strain simulations of an SPAD device array shows the silicon thin film would not reach the fracture strain value when the flexible SPAD array is bent with a radius of 2.5 mm. Our results show the flexible SPAD exhibits enhanced SPDE compared to the SOI-based one and extends applications to a large range of possible areas, including implantable, photon-counting devices for time-resolved biomedical sensing or bio-inspired imaging designs.

## 5.2 Device design and fabrication process

The flexible SPAD was realized by first growing an n-i-p layer on a silicon-on-insulator (SOI) substrate; the insulator ($SiO_2$) can act as a etch-stop layer in the following fabrication. A reduced-pressure chemical vapor deposition (RPCVD) reactor was used to grow the epitaxial layer, and phosphine ($PH_3$) and diborane ($B_2H_6$) are used as the n-type and p-type dopant, respectively. Detailed growing parameters and after-growth characterization (secondary ion mass spectroscopy) can be found in the supporting information. The schematic fabrication process for the flexible SPAD is shown in Fig.5.1(a) and involves a two-step transfer process.

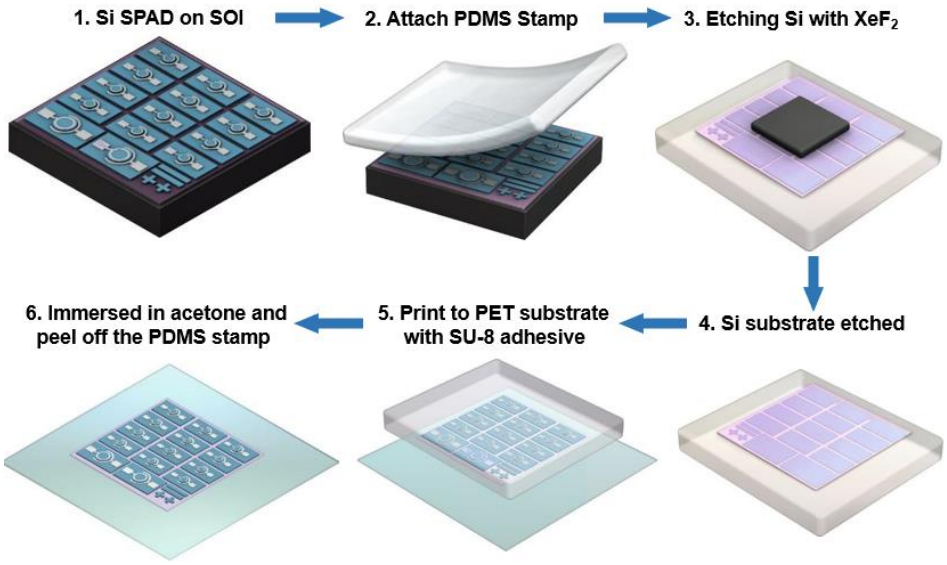


**Figure 5.1:** Schematic fabrication flow of flexible SPAD array, from growing silicon epitaxial layer to device substrate removal for the transfer printing process

| | | | |
|---|---|---|---|
| As grown Silicon | N+ | Phos: $2\times10^{19}$ $cm^{-3}$ | 600 nm |
| | N- | Phos: $1\times10^{18}$ $cm^{-3}$ | 300 nm |
| | i | Unintentionally doped | 700 nm |
| | P- | Boron: $1\times10^{18}$ $cm^{-3}$ | 200 nm |
| | P+ | Boron: $2\times10^{19}$ $cm^{-3}$ | 500 nm |
| SOI substrate | p- | Boron: $1\times10^{15}$ $cm^{-3}$ | 200 nm |
| | $SiO_2$ etch stop layer | | 250 nm |
| | Handling silicon substrate | | |

**Figure 5.2:** Detailed growing parameters for RPCVD chamber

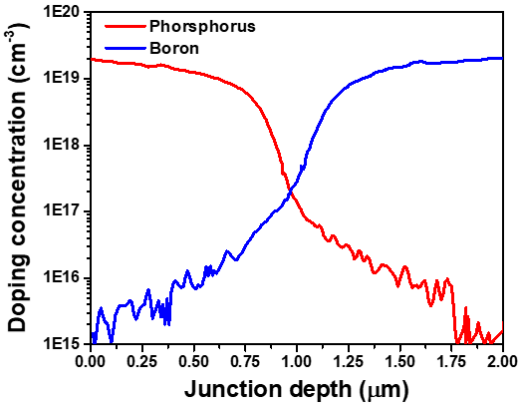


**Figure 5.3:** Secondary ion mass spectroscopy (SIMS) results

The purpose of first transfer process is to remove the rigid silicon substrate and offer protective coatings for SPAD device layer during substrate removal. The second step is to transfer the SPAD device layer to a flexible foreign substrate and remove the protective coating on the SPAD. After the epitaxial growth on silicon-on-insulator (SOI), standard nanofabrication procedures were used to fabricate mesa-defined single photon avalanche photodetectors (SPAD). The round shape of the mesa can offer better estimation on the photo sensing area and is easier for optical alignment, since the light source is also collimated and focused into a round shape, as observed by a microscope. The image of the focused light spot and the device under measurement can be seen in

the supporting information. After the SPAD fabrication is finished, the device area is protected by spin coating poly (methyl methacrylate), abbreviated as PMMA and mounted upside down on the grinding tool with wax to remove most of the silicon substrate by grinding. About 450 μm of the silicon substrate can be removed, and the remaining substrate thickness is about 50 μm. After the grinding process, the device was rinsed by acetone and DI water. It was then spin coated with PMMA again and carefully mounted on the polydimethylsiloxane (PDMS) stamp. We then use a $XeF_2$ etch recipe to remove the remaining silicon substrate. The etch rate of silicon substrate in $XeF_2$ is about 5 μm/min. It takes about 10 minutes to remove all the silicon substrate, and the $XeF_2$ etch stops at the $SiO_2$ layer. After the etching, the sample is coated by SU8-2025 and attached to a flexible polyethylene terephthalate (PET) substrate. Subsequent processing includes soft baking for 3 minutes, UV exposure for 45 seconds and hard baking for 3 minutes to cure the SU8-2025 layer. Finally, the device was immersed into acetone to remove the PDMS stamp and the protective PMMA. The device was then rinsed with isopropyl alcohol (IPA) and DI water to remove the residue particles on the sample.

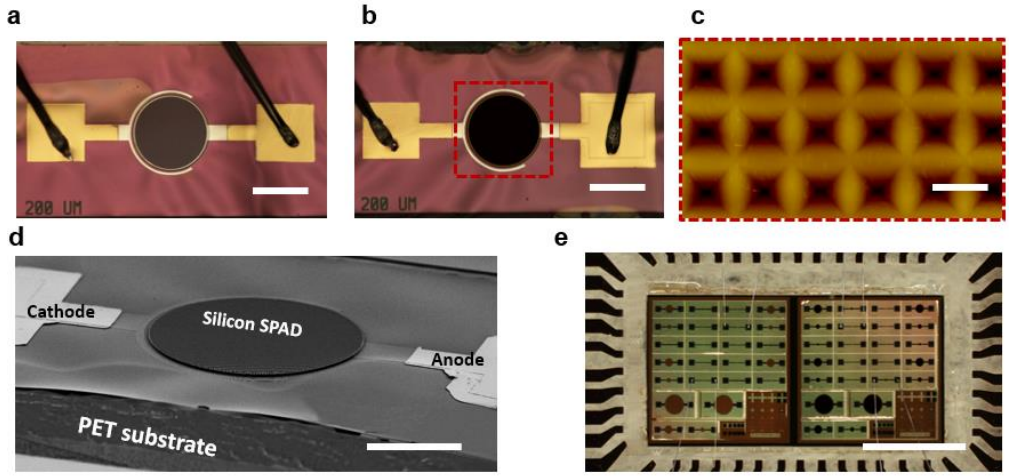


**Figure 5.4:** (a) Optical microscope image of the flexible SPAD without the light-trapping inverted pyramid; scale bar is 200 μm, the aluminum wire bonding shown in the image is used for connection to external circuit for SPAD characterization. (b) Optical microscope image of the flexible SPAD with the light-trapping inverted pyramid; scale bar is 200 μm. (c) Atomic force microscope (AFM) image of the light-trapping structure on SPAD; the scale bar is 1μm. (d) Scanning electron microscope (SEM) angled view of the single flexible SPAD with light-trapping structure; the scale bar is 25 μm. (e) Optical microscope image of the flexible SPAD array, which includes 15 devices without light trapping structure (left side) and 15 devices with light trapping structure (right side); scale bar is 1.5 mm.

Fig.5.4 (a) and (b) show optical microscopy images of the flexible SPAD without and with the light-trapping structure. The light-trapping structure allows more light to be absorbed in the device photo sensing area, therefore, the device photon sensing area appears darker (Fig.5.4(b)) compared with the one without the light-trapping structure (Fig.5.4(a)). Fig.5.4(c) shows an atomic force microscope (AFM) image of the light-trapping structure fabricated on the top surface of the SPAD. The dimension of the light-trapping, inverted-pyramid structure is optimized to have an 850 nm periods, and is 600 nm in depth in order to enhance the target wavelength (750 nm – 1050 nm) range we are interested in, as we reported in earlier work[124]. The angled view of the flexible SPAD reveals the details of both device and substrate thicknesses, as shown in Fig.5.4(d). The fabricated flexible SPAD array is shown in Fig.5.4(e). Each single

device is separated into an SPAD island by dry etching to allow the SPAD array to be bent, as will be shown later in the discussion session. To demonstrate that the entire fabrication process does not affect the optoelectronic performance of the SPAD, both the flexible SPAD and the original SOI-based SPAD are characterized by the current-voltage response and EQE response and compared. The measurement condition is the same for both types of device. The comparison (see Fig.5.5 – 5.7) shows the that flexible SPAD is not degraded by the fabrication process. We focus our analyses on the flexible SPAD in the remaining part of the paper and use the SOI-based SPAD as the control sample.

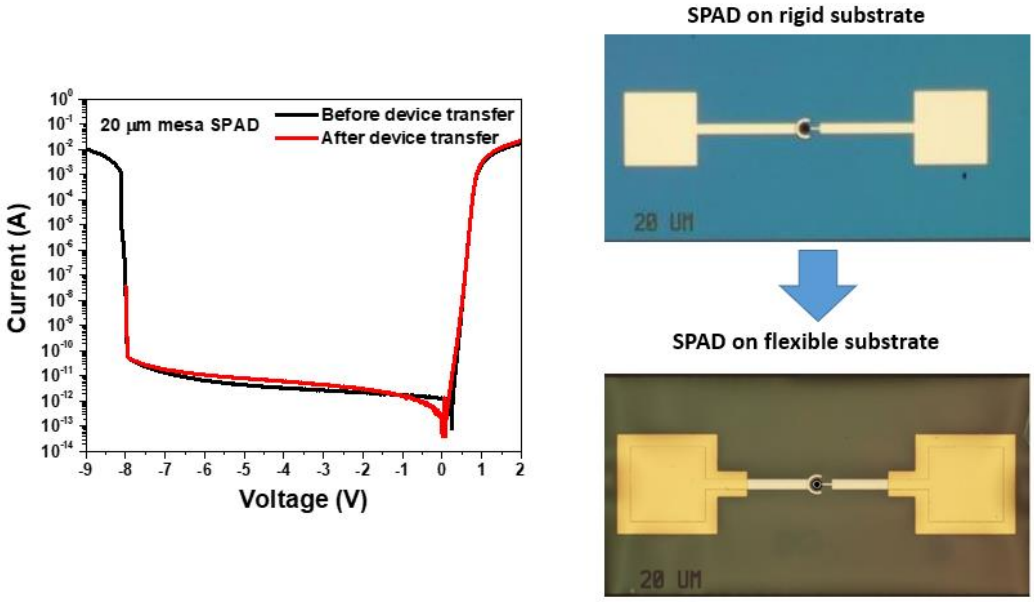


**Figure 5.5:** Performance test on a SPAD with 20 µm diameter mesa

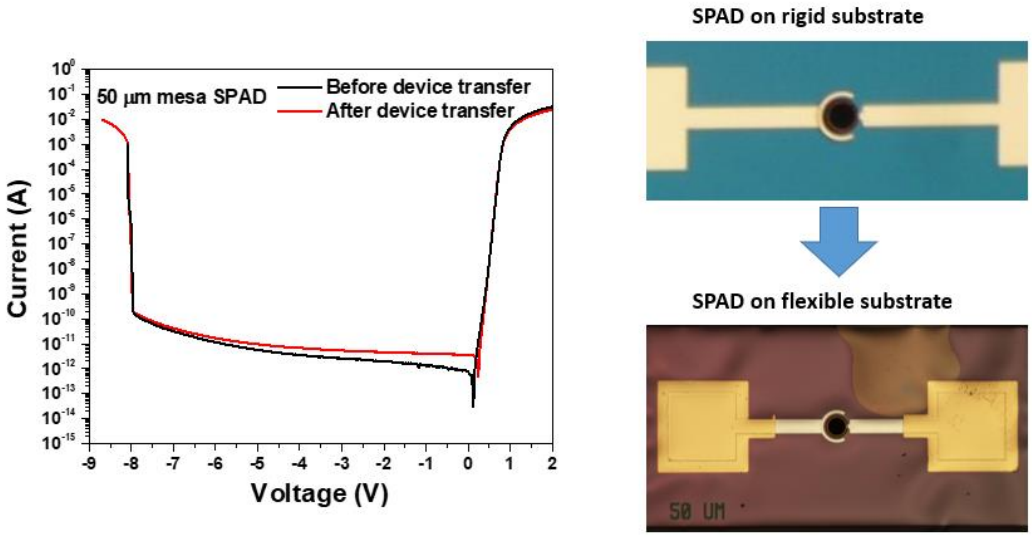


**Figure 5.6:** Performance test on a SPAD with 50 µm diameter mesa

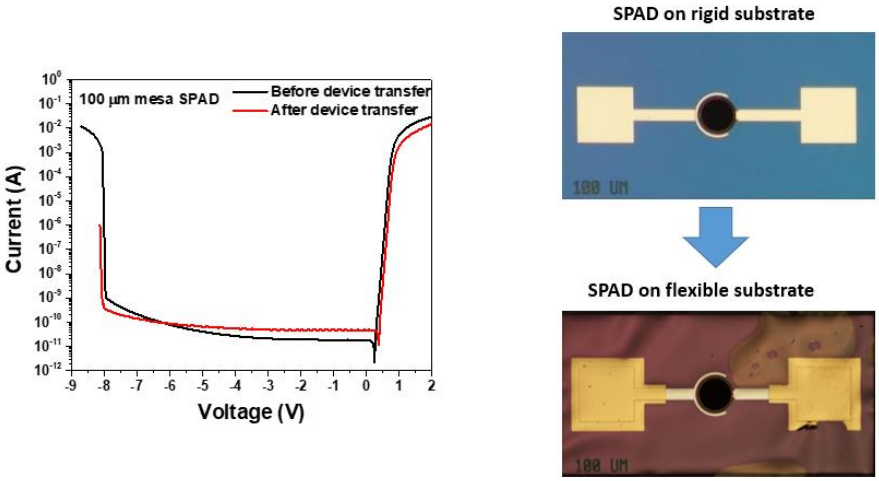


**Figure 5.7:** Performance test on a SPAD with 100 µm diameter mesa

## 5.3 Absorption and quantum efficiency enhancement

To enhance the absorption, the inverted-pyramid light-trapping structure is an efficient method for anti-reflection and light trapping in the device[11,125]. As light propagates from the air to the device, the light trapping structure serves as a structure with graded refractive index[125], which reduces the reflection in comparison with an abrupt flat surface between air and device. The light-trapping structure also traps light in the device by diffraction. The diffraction makes light travel with both vertical and

horizontal wavevectors inside the device, thus increasing the light path length. To maximize the antireflection and light-trapping effects, the dimensions of each single light-trapping inverted-pyramid structure should be close to the target wavelength scale. In our case, we chose 850 nm as the period and 600 nm as the depth since we focus on absorption enhancement in the near infrared light spectrum (750 nm to 1050 nm). Fig.5.8(a) and (c) show the finite-differential time-domain (FDTD) simulations of the absorption distribution of the light-trapping device and the flat surface device. Both simulations are conducted at the wavelength of 850 nm. Fig.5.8(a) shows the absorption distribution of flexible SPAD without the light-trapping structure; the standing wave effect across the silicon thin film mainly contributes the absorption. However, due to low absorption coefficient and limited optical path length, absorption is still weak. With the light-trapping structure, the absorption over the junction region is much enhanced, as shown by Fig.5.8(c). To confirm the absorption enhancement is broadband, we further simulated the absorption over the target wavelength (750 nm to 1050 nm) we are interested in. The simulation is also conducted on the flexible SPAD. Fig.5.8(b) and (d) show the simulated absorption spectra of the flexible SPAD with a flat surface and with light-trapping structure. This absorption comparison shows that the light-trapping structure enhances the absorption over the target near-infrared wavelength range.

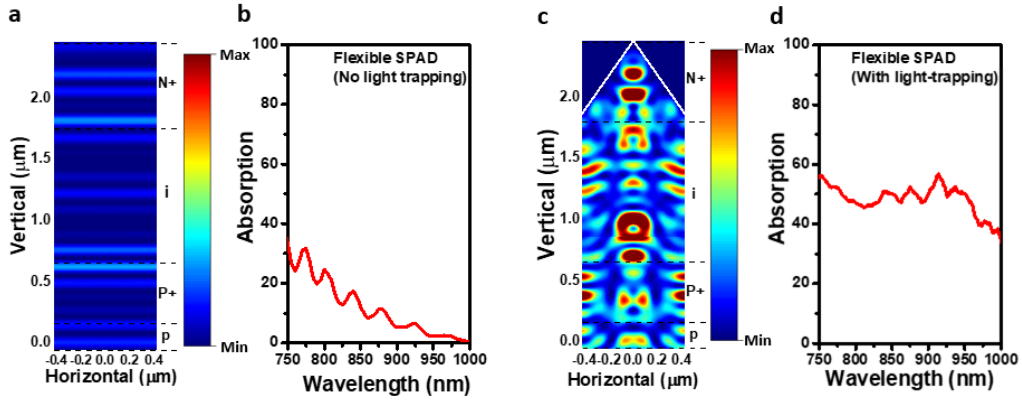


**Figure 5.8:** (a) Spatial distribution of absorption at 850 nm of SPAD without the light-trapping structure. (b) Simulated absorption spectrum of SPAD without the light-trapping structure. (c) Spatial distribution of absorption of SPAD with the light-trapping structure. (d) Simulated absorption spectrum of SPAD with the light-trapping structure.

After the analysis of the absorption enhancement due to light-trapping nanostructure, the experimental optoelectronic performance is the next performance we focused on. A typical parameter termed the external quantum efficiency (EQE) is used to quantify how much photo current is generated and collected by the external circuit[99]. The EQE can be described by the following equation: $\eta$ = (carriers/sec)/(photons/sec) = $(I_{ph}/e)/(\lambda \times P_{inc}/hc) = 1.24\times(I_{ph}/Pinc)/\lambda$, where $P_{inc}$ is the light power incident on the photo sensing area, which can be measured by a calibrated photodiode and $\lambda$ is the wavelength of interest. We measured the photo current $I_{ph}$ corresponding to different wavelengths and calculated the EQE. Fig.5.9(a) shows the EQE with the 3 μm thick, flat-surface device. The EQE follows the same trend as the absorption spectrum in Fig.5.8(b). Without the light-trapping structure, the value of EQE follows the theoretical EQE of the 3 μm flat-surface silicon. In contrast, the light-trapping structure produces broadband EQE enhancement. As shown in Fig.5.9(b), the EQE enhancement makes the 3 μm thick device performance equivalent to an 11 μm thick flat-surface device in

the wavelength range from 750 nm to 800 nm and equivalent to a 20 μm flat device in the wavelength range from 875nm to 1050nm. Further measurement of the angle-dependent photo response, at the detection angle of 70 degrees, shows that the light-trapping structure can enhance the EQE from 5% of the flat-surface device to 42.5% for the light-trapping device, proving that the light-trapping effect is angle insensitive in the flexible SPAD.

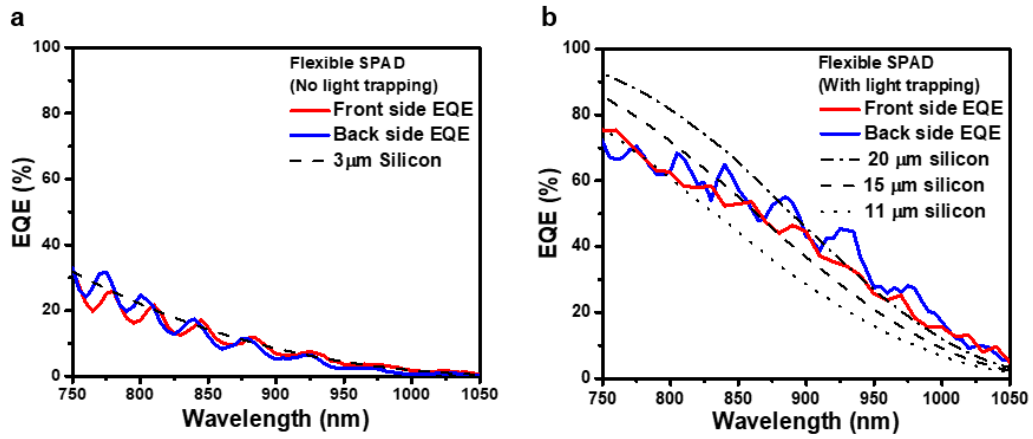


**Figure 5.9:** (a) Measured external quantum efficiency comparison of SPAD without the light-trapping structure. (b) Measured external quantum efficiency comparison of SPAD with the light-trapping structure.

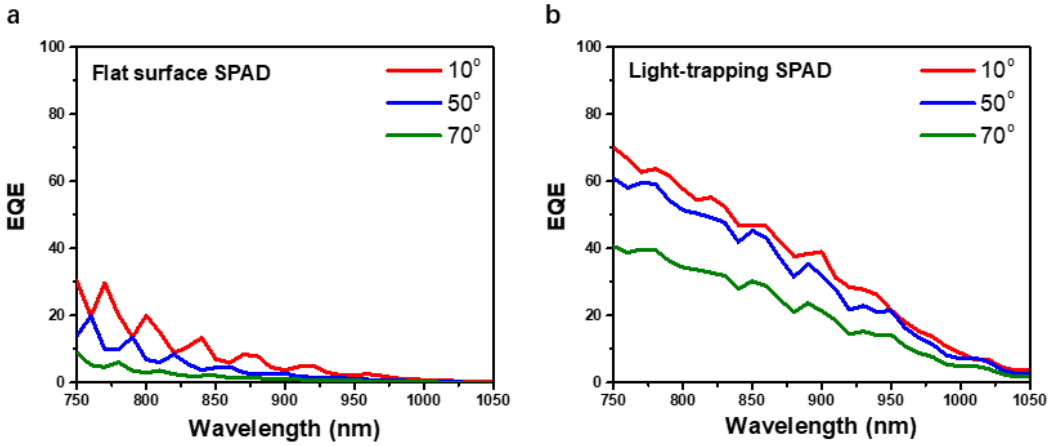


**Figure 5.10:** Angular dependence EQE results with flexible flat surface SPAD and flexible light trapping SPAD

## 5.4 Near infrared single photon detection efficiency enhancement

Based on the above discussion, we can conclude that the light-trapping structure

allows more light absorption, resulting in higher EQE. However, two more factors can influence the value of the SPDE, as indicated by the equation[126]: SPDE= FF × EQE × $\varepsilon_{trigger}$, where FF is the device photo sensing area fill factor, EQE is the detector quantum efficiency, and $\varepsilon_{trigger}$ is the probability of the simultaneous presence of an electron and a hole to trigger the avalanche process. Since the electrical properties of the flexible SPAD do not change after the substrate removal and the device transfer print process, the value of εtrigger should be the same in the flexible SPAD and control SPAD. Therefore, the fill factor is an important parameter which can decide the value of the SPDE. (Fill factor: photo sensing area/the device area) Fig.5.11(a) and (b) show the flexible SPAD with front side and back side, respectively.

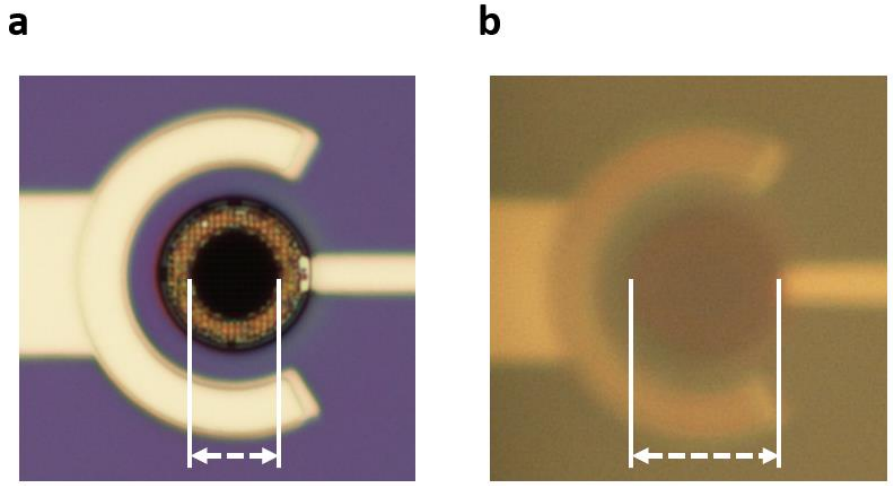


**Figure 5.11:** (a) Front surface image of flexible SPAD. (b) Back surface image of flexible SPAD; photo sensing area is enhanced compared with the front surface device.

As can be seen from these two figures, the fill factor of the flexible SPAD from back side is larger than that from the front side, since there is no metal electrode blocking the light from the back side. We then utilized the gated Geiger mode with a passive quenching circuit to measure the SPDE of both flexible SPAD and control

SPAD. The measuring circuit can be seen in Fig.5.12.

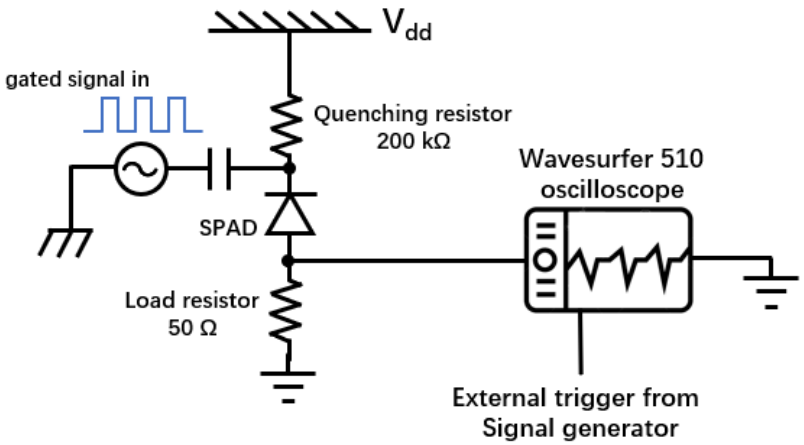


**Figure 5.12:** Measuring circuits for single photon detector testing

The SPAD is DC biased below breakdown voltage and fed with a gated voltage source by a signal generator to work in the Geiger mode. The light source and device are synchronized by the signal generator internal trigger (5ns window length with 1 kHz duty cycle). The light source is attenuated through an optical density filter and integrating sphere, and calibrated by reference optical power meter, device is DC reverse biased at 7.5 V and gated voltage pulse is 2.5 V. An oscilloscope is used to record all the avalanche events triggered by the device during measurement.

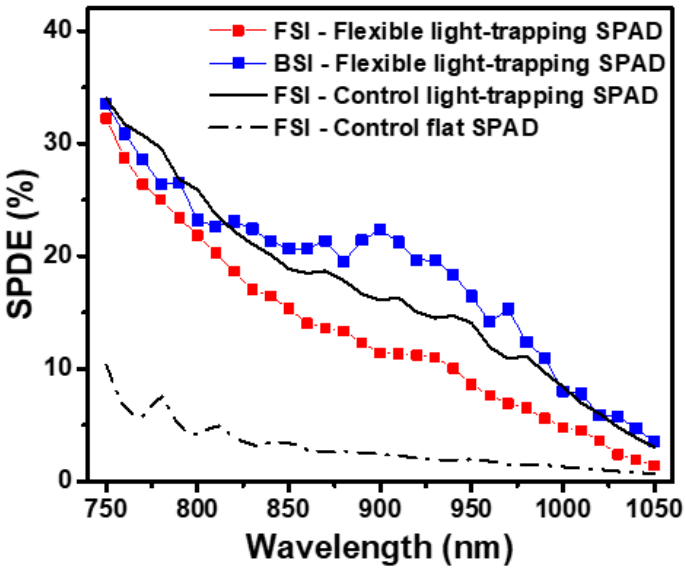


**Figure 5.13:** SPDE (single-photon detection efficiency) comparison of control SPAD (single-photon avalanche photodetector) under FSI (front-side illumination) and flexible SPAD under FSI and BSI (back-side illumination) mode.

Fig.5.13 shows the SPDE result of both flexible SPAD and control SPAD. The SPDE comparison in Fig.5.13 shows that the FSI-flexible SPAD has lower detection efficiency than the FSI-control SPAD. The detection efficiency decrease of the FSI-flexible SPAD can be mainly attributed to the absence of the silicon substrate, which can act as a reflector in the near-infrared wavelength region. The light reflection from the SiO2/Si interface is calculated to be 18.9% at the wavelength of 850 nm, by using the Fresnel equation. On the other hand, the substrate of the flexible SPAD is SiO2 and low refractive index SU-8/PET (about 1.58 and 1.53 at the wavelength of 850 nm27,28), which does not form an efficient reflector compared to the combination of SiO2 and silicon substrate. The reflection from the SiO2/SU-8 interface is calculated to be only 0.3% at the wavelength of 850 nm. However, the lack of reflector associated with the flexible SPAD can be solved by using back surface illumination (BSI). When the flexible SPAD works in the BSI mode, both the light-trapping structure and the anode

metal electrode can serve as the reflector. We further measured the flexible SPAD under the BSI mode. As shown in Fig.5.13, the SPDE of the BSI mode is similar or even higher than that of the control SPAD. Compared with the control SPAD, in which 36.2% of the photo sensing area has been blocked by the anode metal electrode. The blocking area can be calculated from the Fig.5.12(a). The flexible SPAD working under the BSI mode gives higher fill factor due to the absence of the metal electrode blocking layer. Therefore, in terms of SPDE enhancement, the combination of the light-trapping structure and the higher fill factor gives the flexible SPAD better performance than the control SPAD.

## 5.5 Detector timing jitter characterization

Another important figure of merit for an SPAD is timing jitter, which describes the uncertainty time distribution of the photo generated carriers reach the depletion region and are collected. Small timing jitter such as lower than 100 ps is required, where the SPAD is used to detect and reconstruct the decay light signal which has fast decay time in the order of few nano-seconds[80,123] or in the order of sub nano-seconds from ultrafast scintillators[127,128] and fluorescence components[129]. Due to the micron-meter thin of our flexible SPAD, the full-width at half maximum (FWHM) timing jitter of our flexible SPAD is designed to be sub-100ps level. To measure the timing jitter, we employed the time-correlated single-photon counting (TCSPC) technique[130], with the 850nm pico-second laser (Hamamatsu PLP-10). The laser and the device are synchronized by the signal generator. An ultrafast oscilloscope (Wavesurfer 510) with bandwidth of 1GHz

is used to monitor the avalanche pulses from the device. Since the flexible SPAD has its best detection efficiency under BSI mode, we characterize the timing jitter letting the flexible SPAD work under the BSI mode and compare the performance with the control sample.

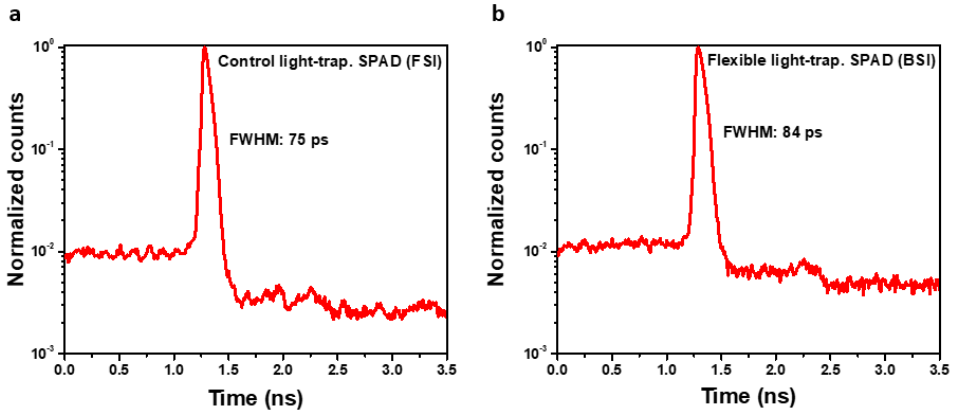


**Figure 5.14:** Timing jitter characteristics of flexible and control SPADs (a) Timing jitter performance of control SPAD under FSI mode, with 75 ps FWHM timing jitter. (b) Timing jitter performance of flexible SPAD under BSI mode, with 84 ps FWHM timing jitter.

Fig.5.14 show the timing jitter comparison, where the FWHM timing jitter of BSI-flexible SPAD is 84 ps and the control SPAD is 75 ps. The FSI-flexible SPAD timing jitter (also shown in Fig.5.14) is the same as the control SPAD. This timing jitter, as far as we trace the literature[131,132], is the best performance among the flexible SPAD work. The increase of BSI-flexible SPAD timing jitter may come from the more lateral collection of photon-generated carriers, since the fill factor of BSI-flexible SPAD is higher than the FSI-control SPAD.

## 5.6 Single photon detector performance under flexure

The mechanical bending properties of the flexible SPAD is the final performance metrics we focus on. To satisfy the bending properties, each SPAD is isolated to form a single device island (880 μm in length and 440 μm in width) by the dry etching method.

Fig.5.15 shows the photo image of flexible SPAD wrapped around a glass rod which has a radius of 2.5 mm.

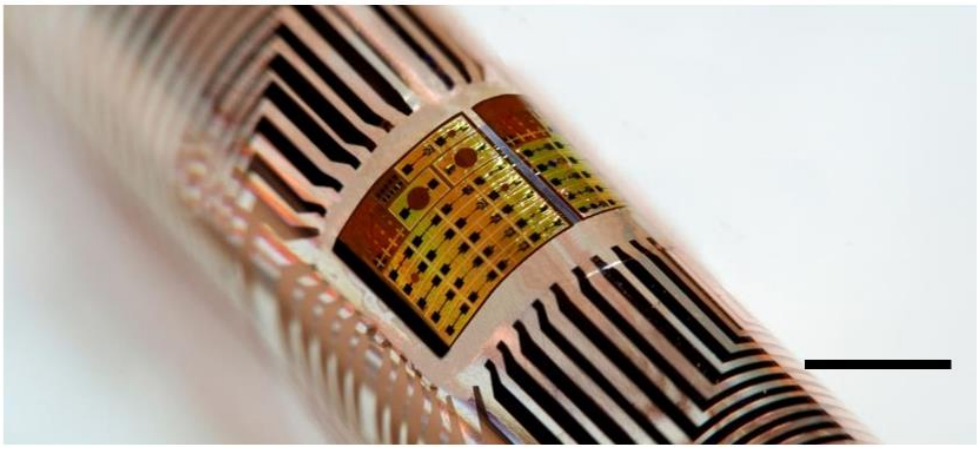

**Figure 5.15:** Photo image of flexible SPAD wrapped around a glass rod whose radius of curvature is 2.5 mm

To demonstrate that the device can work properly under the bending condition, the bent flexible SPAD was used to measure the dark count rate (DCR) and compare it with the control sample. A probe station was used for the DCR measurement. As shown in Fig.5.16, the waveform captured from the oscilloscope shows that the device dark count electrical performance remains consistency among the flexible SPAD and the control SPAD. The typical DCR of flexible SPAD and control SPAD is 400kHz and, maximum DCR is about 600kHz. The high DCR mainly results from the lack of a guard ring structure, which can be added using a CMOS-compatible fabrication process. Further measurements of timing jitter show the flexible device can also work normally under when bent to the radius of 2.5 mm (76 ps FWHM under FSI; the control SPAD has 75 ps FWHM, see the supporting information for the data under bent condition), which suggests our device can be wrapped around small object and used for optical tomography35.

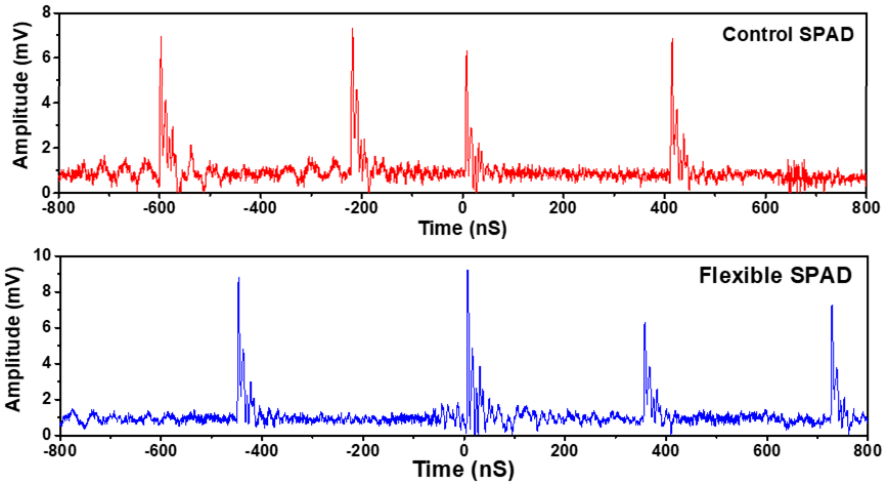


**Figure 5.16:** Dark count rate comparison of control SPAD and flexible SPAD

Finally, we conduct a finite element strain analyses (FEA) by modeling the entire device in ABAQUS software. The simulation results (Fig.5.17) show that the maximum strain is located at the boundary of the device. When the radius of curvature reaches 2.5 mm, as experimentally used in our case, the maximum strain in the silicon across the entire device is ~ 1.0 %, which is below the silicon fracture limit (1.81%). Both the experiments and the simulations show that the flexible SPAD can work normally under moderate bending deformation.

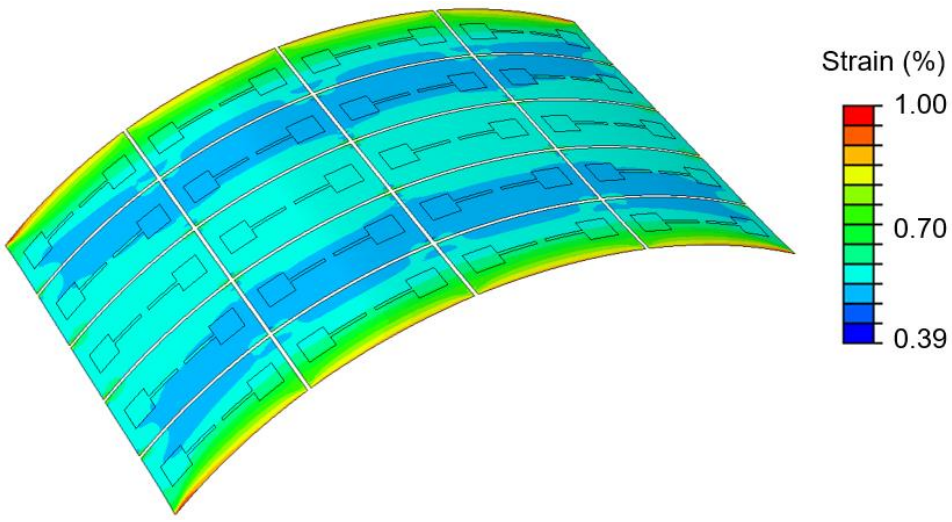


**Figure 5.17:** Strain simulations of flexible SPAD under the bending radius of 2.5 mm. The maximum

strain over the device is 1.0 % on the boundary of the device.

## 5.7 Conclusion

To conclude, we report a flexible SPAD with enhanced single photon detection efficiency compared with the control SPAD. With the light-trapping nano structure and higher fill factor due to the detection method of BSI, the flexible SPAD reaches higher SPDE than the control SPAD one from the wavelength range of 820 nm to 980nm. The timing jitter of the flexible SPAD remains below 100 ps, which is consistent with the control SPAD. This consistency indicates the fabrication process we developed for the flexible SPAD does not damage the performance of SPAD. The final characterization of the bent flexible SPAD proves our device can work normally under the bending curvature of 2.5mm. This flexible SPAD we have developed can be a strong candidate for implantable biomedical imaging/sensing purposes, high sensitivity bionic eyes for enhancing human vision, or the realization of three-dimensional, single-photon optical tomography for small biological structures.

# 6 Conclusions

In this thesis, several types of photo detector devices are demonstrated, including metal-semiconductor-metal photo conductors, metal-semiconductor-metal Schottky photodiodes, p-i-n photodiodes and avalanche photodiodes working in Geiger mode. All the detectors are based on the semiconductor thin films, the thickness varies from 3 μm to 5 nm. These thin film-based detectors show very unique performance such as very low dark current, mechanically flexible as well as wavelength selective due to thin film interference effect. Thanks to our unique fabrication technique, the semiconductor thin film can be transferred to various substrate to achieve different sensing purposes. In the first work, we show by transferring the ultrathin germanium film on the pre-designed optical cavity, the detector can show strong wavelength selective photo response behavior. Since the interference effect is based on both the value of refractive index and the extinction ratio, the wavelength selective photo sensing purpose can be achieved by slightly changing the thickness of the germanium thin film, from 100 nm to 5 nm. Also, the dark current is greatly suppressed by reducing the thickness of the germanium thin film. In the second work, we continue to exploit the first work and utilize it to achieve a broadband, high resolution spectrometer. The design for the spectrometer is we transfer print two types of semiconductor thin films (silicon and germanium) on the designed cavity. The designed cavity has a grayscale $Al_2O_3$ spacer layer, therefore, each silicon or germanium photon sensing pixel has its own photo response spectrum fingerprint. This device proves by combing the semiconductor thin

film and the grayscale optical cavity structure, our device can replace the conventional, bulky newton light prism to achieve high resolution hyper-spectral imaging.

We continue our work to explore more possibilities to utilize the semiconductor thin film for photo detection purposes. The above work is focused on wavelength selective photodetection work. In the following work, we explore the possibilities of using semiconductor thin film as the single-photon detector. We used the chemical vapor deposition method to grow the p-i-n doping profile on the semiconductor thin film, after the material deposition, standard nanofabrication method is used to fabricate a mesa-type single-photon detector. In order to enhance the detecting efficiency, inverted nano-pyramid structure was fabricated on the single-photon detector. After the thin film-based device is fabricated, the device was transferred to flexible substrates to test the single photon responses. The result shows that photon detection efficiency was enhanced because of the inverted, nano-pyramid structure and the detection method of back side illumination. Further work can be investigated by using this flexible single-photon detector. For example, this device can be implanted into live body to detect bio-information or can be used as a basic component for retina protheses. At last, we investigate the relationship of detection efficiency with the temperature change. By this investigation, we conclude that the p-i-n photodiode's single photon detection efficiency with ultrathin intrinsic layer is less sensitive to temperature change. This conclusion is helpful when developing a flexible single photon detector for a complicated biomedical detection.

To make a final conclusion, the semiconductor thin film-based photo detector is a strong candidate for high efficiency detection. And various types of photo detector can be achieved, especially in the area of single-photon detection, wavelength selective detection for hyper-spectral imaging as well as implantable single-photon level biomedical detection or retinal protheses.

# 7 Future work

We have discussed three types of photo detection devices in this thesis, which includes ultrathin semiconductor thin film-based photo conductors, thin film-based spectrometers and flexible single photon detectors. All of these three types of detectors are still being further developed in lab to achieve more competitive performance and we are seeking to commercialize these devices.

So far, the photo conductor we have developed has very small photo sensing area (about 50 μm×100 μm). However, the current photo conductor in the market are usually required very large area (about 10 mm×10 mm), since large area photo conductor have much higher chance to detect the light signal from all the directions. Therefore, the development of large area, ultrathin semiconductor thin film is the remained work to be done. In this work, the membrane transfer method is used to fabricate the device. In future work, we would use the substrate removal method to obtain large area, uniform ultrathin semiconductor membrane and transfer the membrane to foreign optical cavity.

The spectrometer we have developed is still under calibration. To develop a spectrometer which can recover the electromagnetism spectrum precisely, the number of photon sensing pixel should be as many as possible. However, the metal interconnect becomes an issue when the pixel number is designed to be 320. In this case, double layer metal interconnect should be designed. This design is just recently developed and needs further experimental work. After the experimental work is finished, the spectrometer needs to be recalibrated.

The flexible single-photon avalanche photodetector needs denser and more pixels in one chip for future use. In order to achieve this, the tape-out for IC circuit is needed in this case. Device needs to be re-designed in software in computer-aided design software like Cadence™, the device needs to fit well into the IC fabrication process flow by using the silicon-on-insulator substrate and then do the device layer release to the flexible substrate. Issues with the flexible device such as device isolation and performance under bent condition needs to be recalibrated.

# Appendix – Publications of PhD work

1. **Z. Xia**, H. Song, M. Kim, M. Zhou, T.-H. Chang, D. Liu, Y. Xin, K. Xiong, H. Mi, X. Wang, F. Xia, Z. Yu, Z. Ma and Q. Gan, "Single-crystalline germanium nanomembrane photodetectors on a foreign substrate," **Science Advances**, 3, e1602783 (2017).
2. **Z. Xia**, K. Zang, D. Liu, M. Zhou, T.-J. Kim, H. Zhang, M. Xue, J. Park, M. Morea, J. H. Ryu, T.-H. Chang, J. Kim, S. Gong, T. I. Kamins, Z. Yu, Z. Wang, J. S. Harris and Z. Ma, "High-sensitivity silicon ultraviolet p+-i-n avalanche photodiode by using ultra-shallow boron gradient doping," **Applied Physics Letters**, 111, 081109 (2017).
3. **Z. Xia**, K. Zang, T. Chang, M Zhou, J. Salman, M. Kats, Z. Yu, Z. Wang, J. Harris and Z. Ma, "An ultrathin flexible single photon detector," manuscript submitted to Applied Physics Letters.
4. K. Xiong, H. Mi, T. Chang, D. Liu, **Z. Xia**, M-Y. Wu, X. Yin, S. Gong, W. Zhou, J. Shin, X. Li, M. Arnold, X. Wang, H-C. Yuan, Z. Ma, "AlGaAs/Si dual junction tandem solar cells by epitaxial lift off and print transfer assisted direct bonding," **Energy Science & Engineering,** 6, 47 (2018).
5. K. Zhang, Y. Jung, S. Mikael, J. Seo, M. Kim, H. Mi, H. Zhou, **Z. Xia,** W. Zhou, S. Gong, Z. Ma, "Origami silicon optoelectronics for hemispherical electronic eye systems," **Nature Communications**. 8, 1782 (2017).

6. T.-H. Chang, W Fan, S. Liu, D. Liu, **Z. Xia**, L. Menon, H. Yang, J. Berggren, M. Hammar, Z. Ma, "Selective release of InP heterostructures from InP substrates," **Journal of Vacuum Science and Technology B** 34, 041229 (2016).
7. K. Zang, X. Jiang, Y. Huo, X. Ding, M. Morea, X. Chen, C.-Y. Lu, J. Ma, M. Zhou, **Z. Xia**, Z. Yu, T.I. Kamins, Q. Zhang and J. S. Harris, "Silicon single-photon avalanche diodes with nano-structured light trapping," **Nature Communications**. **8**, 628 (2017).
8. M. Zhou, H. Song, X. Xu, A. Shahsafi, **Z. Xia**, Z. Ma, M. Kats, J. Zhu, B.S. Ooi, Q. Gan and Z. Yu, "Accelerating vapor condensation with daytime radiative cooling," arXiv preprint arXiv:1804.10736 (2018). (Nature Sustainability sent to reviewers)
9. **Z. Xia**, H. Song, M. Kim, M. Zhou, T.-H. Chang, D. Liu, K. Xiong, Z. Yu, Z. Ma, and Q. Gan, "Photodetecting MOSFET based on ultrathin single-crystal germanium nanomembrane," in Conference on Lasers and Electro-Optics, OSA Conference Papers (Optical Society of America, 2016), paper STh4E.
10. D. Liu, **Z. Xia**, S. J. Cho, D. Zhao, H. Zhang, T.-H. Chang, X. Yin, M. Kim, J. -H. Seo, J. Lee, X. Wang, W. Zhou, Z. Ma, "Cavity enhanced 1.5μm LED with silicon as a hole injector," in 9767, 97670Y (International Society for Optics and Photonics, 2016)

# Reference


1. Xia, F., Mueller, T., Lin, Y., Valdes-Garcia, A. & Avouris, P. Ultrafast graphene photodetector. *Nat. Nanotechnol.* **4**, 839–843 (2009).
2. Mueller, T., Xia, F. & Avouris, P. Graphene photodetectors for high-speed optical communications. *Nat. Photonics* **4**, 297–301 (2010).
3. Liu, L. *et al.* An ultra-small, low-power, all-optical flip-flop memory on a silicon chip. *Nat. Photonics* **4**, 182–187 (2010).
4. Virot, L. *et al.* Germanium avalanche receiver for low power interconnects. *Nat. Commun.* **5**, (2014).
5. Rivera, M., Velázquez, R., Aldalbahi, A., Zhou, A. F. & Feng, P. High Operating Temperature and Low Power Consumption Boron Nitride Nanosheets Based Broadband UV Photodetector. *Sci. Rep.* **7**, (2017).
6. Lopez-Sanchez, O., Dumcenco, D., Charbon, E. & Kis, A. Avalanche photodiodes based on MoS2/Si heterojunctions. (2014).
7. Janisch, C. *et al.* MoS $_2$ monolayers on nanocavities: enhancement in light–matter interaction. *2D Mater.* **3**, 025017 (2016).
8. Song, H. *et al.* Nanocavity absorption enhancement for two-dimensional material monolayer systems. *Opt. Express* **23**, 7120 (2015).
9. Lopez-Sanchez, O., Lembke, D., Kayci, M., Radenovic, A. & Kis, A. Ultrasensitive photodetectors based on monolayer MoS2. *Nat. Nanotechnol.* **8**, 497–501 (2013).

10. Trauzettel, B., Bulaev, D. V., Loss, D. & Burkard, G. Spin qubits in graphene quantum dots. *Nat. Phys.* **3**, 192–196 (2007).

11. Wang, K. X., Yu, Z., Liu, V., Cui, Y. & Fan, S. Absorption Enhancement in Ultrathin Crystalline Silicon Solar Cells with Antireflection and Light-Trapping Nanocone Gratings. *Nano Lett.* **12**, 1616–1619 (2012).

12. Kashani, H., Ito, Y., Han, J., Liu, P. & Chen, M. Extraordinary tensile strength and ductility of scalable nanoporous graphene. *Sci. Adv.* **5**, eaat6951 (2019).

13. Tao, L. *et al.* Silicene field-effect transistors operating at room temperature. *Nat. Nanotechnol.* **10**, 227–231 (2015).

14. Acun, A. *et al.* Germanene: the germanium analogue of graphene. *J. Phys. Condens. Matter* **27**, 443002 (2015).

15. Quhe, R. G., Wang, Y. Y. & Lü, J. Silicene transistors - A review. *Chinese Physics B* **24**, (2015).

16. Vali, M., Dideban, D. & Moezi, N. Silicene field effect transistor with high on/off current ratio and good current saturation. *J. Comput. Electron.* **15**, 138–143 (2016).

17. Le Lay, G. 2D materials: Silicene transistors. *Nature Nanotechnology* **10**, 202–203 (2015).

18. Xu, T., Wu, Y.-K., Luo, X. & Guo, L. J. Plasmonic nanoresonators for high-resolution colour filtering and spectral imaging. *Nat. Commun.* **1**, 59 (2010).

19. Wang, S. *et al.* Large-Area Free-Standing Ultrathin Single-Crystal Silicon as

Processable Materials. *Nano Lett.* **13**, 4393–4398 (2013).

20. Steenhoff, V., Theuring, M., Vehse, M., von Maydell, K. & Agert, C. Ultrathin Resonant-Cavity-Enhanced Solar Cells with Amorphous Germanium Absorbers. *Adv. Opt. Mater.* **3**, 182–186 (2015).

21. Kats, M. A., Blanchard, R., Genevet, P. & Capasso, F. Nanometre optical coatings based on strong interference effects in highly absorbing media. *Nat. Mater.* **12**, 20–24 (2013).

22. Kats, M. A. & Capasso, F. Optical absorbers based on strong interference in ultra-thin films. *Laser Photon. Rev.* **10**, 735–749 (2016).

23. Song, H. *et al.* Nanocavity Enhancement for Ultra-Thin Film Optical Absorber. *Adv. Mater.* **26**, 2737–2743 (2014).

24. Juntunen, M. A. *et al.* Near-unity quantum efficiency of broadband black silicon photodiodes with an induced junction. *Nat. Photonics* **10**, 777–781 (2016).

25. Capasso, F. Chapter 1 Physics of Avalanche Photodiodes. *Semicond. Semimetals* **22**, 1–172 (1985).

26. Martinez, N. J. D. *et al.* Single photon detection in a waveguide-coupled Ge-on-Si lateral avalanche photodiode. *Opt. Express* **25**, 16130 (2017).

27. Xie, S. *et al.* InGaAs/AlGaAsSb avalanche photodiode with high gain-bandwidth product. *Opt. Express* **24**, 24242 (2016).

28. Bellis, S., Jackson, J. C. & Mathewson, A. Towards a disposable in vivo miniature implantable fluorescence detector. in (ed. Gannot, I.) **6083**, 60830N

(International Society for Optics and Photonics, 2006).

29. Norian, H., Field, R. M., Kymissis, I. & Shepard, K. L. An integrated CMOS quantitative-polymerase-chain-reaction lab-on-chip for point-of-care diagnostics. *Lab Chip* **14**, 4076–4084 (2014).

30. Schaart, D. R., Charbon, E., Frach, T. & Schulz, V. Advances in digital SiPMs and their application in biomedical imaging. *Nucl. Instruments Methods Phys. Res. Sect. A Accel. Spectrometers, Detect. Assoc. Equip.* **809**, (2016).

31. Cova, S., Ghioni, M., Lacaita, A., Samori, C. & Zappa, F. Avalanche photodiodes and quenching circuits for single-photon detection. *Appl. Opt.* **35**, 1956 (1996).

32. Straub, M. & Hell, S. W. Fluorescence lifetime three-dimensional microscopy with picosecond precision using a multifocal multiphoton microscope. *Appl. Phys. Lett.* **73**, 1769–1771 (1998).

33. Sanzaro, M. *et al.* Single-Photon Avalanche Diodes in a 0.16 μm BCD Technology With Sharp Timing Response and Red-Enhanced Sensitivity. *IEEE J. Sel. Top. Quantum Electron.* **24**, (2018).

34. Liu, X. *et al.* Non-line-of-sight imaging using phasor-field virtual wave optics. *Nature* 1–4 (2019). doi:10.1038/s41586-019-1461-3

35. Furchi, M. *et al.* Microcavity-Integrated Graphene Photodetector. *Nano Lett.* **12**, 2773–2777 (2012).

36. Zang, K. *et al.* Silicon single-photon avalanche diodes with nano-structured light trapping. *Nat. Commun.* **8**, (2017).

37. Gao, Y. *et al.* Photon-trapping microstructures enable high-speed high-efficiency silicon photodiodes. *Nat. Photonics* **11**, 301–308 (2017).

38. Kim, D.-H. *et al.* Epidermal electronics. *Science* **333**, 838–43 (2011).

39. Ko, H. *et al.* Ultrathin compound semiconductor on insulator layers for high-performance nanoscale transistors. *Nature* **468**, 286–289 (2010).

40. Liu, X. *et al.* Strong light–matter coupling in two-dimensional atomic crystals. *Nat. Photonics* **9**, 30–34 (2015).

41. Yuan, H. *et al.* Polarization-sensitive broadband photodetector using a black phosphorus vertical p–n junction. *Nat. Nanotechnol.* **10**, 707–713 (2015).

42. Chen, X. *et al.* Widely tunable black phosphorus mid-infrared photodetector. *Nat. Commun.* **8**, 1672 (2017).

43. Sigle, D. O., Zhang, L., Ithurria, S., Dubertret, B. & Baumberg, J. J. Ultrathin CdSe in Plasmonic Nanogaps for Enhanced Photocatalytic Water Splitting. *J. Phys. Chem. Lett.* **6**, 1099–1103 (2015).

44. Xin, Y. *et al.* Gold–palladium bimetallic nanoalloy decorated ultrathin 2D $TiO_2$ nanosheets as efficient photocatalysts with high hydrogen evolution activity. *J. Mater. Chem. A* **3**, 8659–8666 (2015).

45. Kim, S. J. *et al.* Superabsorbing, Artificial Metal Films Constructed from Semiconductor Nanoantennas. *Nano Lett.* **16**, 3801–3808 (2016).

46. Going, R. W., Loo, J., Tsu-Jae King Liu & Wu, M. C. Germanium Gate PhotoMOSFET Integrated to Silicon Photonics. *IEEE J. Sel. Top. Quantum*

*Electron.* **20**, 1–7 (2014).

47. Assefa, S., Xia, F. & Vlasov, Y. A. Reinventing germanium avalanche photodetector for nanophotonic on-chip optical interconnects. *Nature* **464**, 80–84 (2010).

48. Liang, D. & Bowers, J. E. Recent progress in lasers on silicon. *Nat. Photonics* **4**, 511–517 (2010).

49. Kazazis, D. *et al.* Tunneling field-effect transistor with epitaxial junction in thin germanium-on-insulator. *Appl. Phys. Lett.* **94**, 263508 (2009).

50. Rogers, J. A., Lagally, M. G. & Nuzzo, R. G. Synthesis, assembly and applications of semiconductor nanomembranes. *Nature* **477**, 45–53 (2011).

51. Bruel, M. *et al.* 'Smart cut': a promising new SOI material technology. in *1995 IEEE International SOI Conference Proceedings* 178–179 (IEEE). doi:10.1109/SOI.1995.526518

52. Meitl, M. A. *et al.* Transfer printing by kinetic control of adhesion to an elastomeric stamp. *Nat. Mater.* **5**, 33–38 (2006).

53. Sorianello, V. *et al.* Low-temperature germanium thin films on silicon. *Opt. Mater. Express* **1**, 856 (2011).

54. Masini, G., Colace, L., Galluzzi, F. & Assanto, G. Advances in the field of poly-Ge on Si near infrared photodetectors. *Mater. Sci. Eng. B* **69**–**70**, 257–260 (2000).

55. Nam, D. *et al.* Strained germanium thin film membrane on silicon substrate for optoelectronics. *Opt. Express* **19**, 25866 (2011).

56. Bermejo, D. & Cardona, M. Raman scattering in pure and hydrogenated amorphous germanium and silicon. *J. Non. Cryst. Solids* **32**, 405–419 (1979).

57. Chi On Chui, Okyay, A. K. & Saraswat, K. C. Effective dark current suppression with asymmetric MSM photodetectors in Group IV semiconductors. *IEEE Photonics Technol. Lett.* **15**, 1585–1587 (2003).

58. Xia, Z. *et al.* Photodetecting MOSFET based on ultrathin single-crystal germanium nanomembrane. in *2016 Conference on Lasers and Electro-Optics, CLEO 2016* (2016).

59. Shamala, K. S., Murthy, L. C. S. & Narasimha Rao, K. Studies on optical and dielectric properties of Al2O3 thin films prepared by electron beam evaporation and spray pyrolysis method. *Mater. Sci. Eng. B* **106**, 269–274 (2004).

60. Schmidt, H. *et al.* Transport Properties of Monolayer $MoS_2$ Grown by Chemical Vapor Deposition. *Nano Lett.* **14**, 1909–1913 (2014).

61. Pradhan, N. R. *et al.* Field-Effect Transistors Based on Few-Layered α-$MoTe_2$. *ACS Nano* **8**, 5911–5920 (2014).

62. Kumar, J., Kuroda, M. A., Bellus, M. Z., Han, S.-J. & Chiu, H.-Y. Full-range electrical characteristics of $WS_2$ transistors. *Appl. Phys. Lett.* **106**, 123508 (2015).

63. Yang, R., Wang, Z. & Feng, P. X. L. Electrical breakdown of multilayer MoS2 field-effect transistors with thickness-dependent mobility. *Nanoscale* **6**, 12383–12390 (2014).

64. C. Soci, † *et al.* ZnO Nanowire UV Photodetectors with High Internal Gain. (2007). doi:10.1021/NL070111X

65. Konstantatos, G. *et al.* Hybrid graphene–quantum dot phototransistors with ultrahigh gain. *Nat. Nanotechnol.* **7**, 363–368 (2012).

66. Guo, Q. *et al.* Black Phosphorus Mid-Infrared Photodetectors with High Gain. *Nano Lett.* **16**, 4648–4655 (2016).

67. Takanashi, Y., Takahata, K. & Muramoto, Y. Characteristics of InAlAs/InGaAs high-electron-mobility transistors under illumination with modulated light. *IEEE Trans. Electron Devices* **46**, 2271–2277 (1999).

68. Furchi, M. M., Polyushkin, D. K., Pospischil, A. & Mueller, T. Mechanisms of Photoconductivity in Atomically Thin $MoS_2$. *Nano Lett.* **14**, 6165–6170 (2014).

69. Zhou, H. *et al.* Large Area Growth and Electrical Properties of p-Type $WSe_2$ Atomic Layers. *Nano Lett.* **15**, 709–713 (2015).

70. Kim, M., Seo, J. H., Yu, Z., Zhou, W. & Ma, Z. Flexible germanium nanomembrane metal-semiconductor-metal photodiodes. *Appl. Phys. Lett.* **109**, (2016).

71. Yuan, H. C. *et al.* Flexible photodetectors on plastic substrates by use of printing transferred single-crystal germanium membranes. *Appl. Phys. Lett.* **94**, (2009).

72. Kats, M. A. *et al.* Enhancement of absorption and color contrast in ultra-thin highly absorbing optical coatings. *Appl. Phys. Lett.* **103**, 101104 (2013).

73. Moszyński, M., Kapusta, M., Balcerzyk, M., Szawlowski, M. & Wolski, D.

Large Area Avalanche Photodiodes in X-rays and scintillation detection. *Nucl. Instruments Methods Phys. Res. Sect. A Accel. Spectrometers, Detect. Assoc. Equip.* **442**, 230–237 (2000).

74. Renker, D. & Lorenz, E. Advances in solid state photon detectors. *J. Instrum.* **4**, P04004–P04004 (2009).

75. Moszynski, M. *et al.* Comparative study of avalanche photodiodes with different structures in scintillation detection. *IEEE Trans. Nucl. Sci.* **48**, 1205–1210 (2001).

76. Allier, C. . *et al.* Readout of a LaCl3(Ce3+) scintillation crystal with a large area avalanche photodiode. *Nucl. Instruments Methods Phys. Res. Sect. A Accel. Spectrometers, Detect. Assoc. Equip.* **485**, 547–550 (2002).

77. O'Connor, D. V. & Phillips, D. (David). *Time-correlated single photon counting*. (Academic Press, 1984).

78. Gompf, B., Günther, R., Nick, G., Pecha, R. & Eisenmenger, W. Resolving Sonoluminescence Pulse Width with Time-Correlated Single Photon Counting. *Phys. Rev. Lett.* **79**, 1405–1408 (1997).

79. Liu, J., Sun, Y., Qi, J. & Marcu, L. A novel method for fast and robust estimation of fluorescence decay dynamics using constrained least-squares deconvolution with Laguerre expansion. *Phys. Med. Biol.* **57**, 843–865 (2012).

80. Becker, W. *et al.* Fluorescence lifetime images and correlation spectra obtained by multidimensional time-correlated single photon counting. *Microsc. Res. Tech.* **69**, 186–195 (2006).

81. Brooks Shera, E., Seitzinger, N. K., Davis, L. M., Keller, R. A. & Soper, S. A. Detection of single fluorescent molecules. *Chem. Phys. Lett.* **174**, 553–557 (1990).

82. Yu, W.-K. *et al.* Single-photon compressive imaging with some performance benefits over raster scanning. *Phys. Lett. A* **378**, 3406–3411 (2014).

83. Mata Pavia, J., Charbon, E. & Wolf, M. 3D near-infrared imaging based on a single-photon avalanche diode array sensor. in (eds. Hielscher, A. H. & Taroni, P.) **8088**, 808811 (International Society for Optics and Photonics, 2011).

84. Zalewski, E. F. & Duda, C. R. Silicon photodiode device with 100% external quantum efficiency. *Appl. Opt.* **22**, 2867 (1983).

85. Popović, R. S., Solt, K., Falk, U. & Stoessel, Z. A silicon ultraviolet detector. *Sensors Actuators A Phys.* **22**, 553–558 (1990).

86. Sarubbi, F., Scholtes, T. L. M. & Nanver, L. K. Chemical Vapor Deposition of α-Boron Layers on Silicon for Controlled Nanometer-Deep p + n Junction Formation. *J. Electron. Mater.* **39**, 162–173 (2010).

87. Sarubbi, F., Nanver, L. K. & Scholtes, T. L. CVD Delta-Doped Boron Surface Layers for Ultra-Shallow Junction Formation. in *ECS Transactions* **3**, 35–44 (ECS, 2006).

88. Mohammadi, V., de Boer, W. B. & Nanver, L. K. Temperature dependence of chemical-vapor deposition of pure boron layers from diborane. *Appl. Phys. Lett.* **101**, 111906 (2012).

89. Fehlner, T. P. & Koski, W. S. Direct Detection of the Borane Molecule and the Boryl Radical by Mass Spectrometry. *J. Am. Chem. Soc.* **86**, 2733–2734 (1964).

90. Baylis, A. B., Pressley, G. A. & Stafford, F. E. Mass Spectrometric Investigation of the Pyrolysis of Boranes. IV. Diborane $^{1}$. *J. Am. Chem. Soc.* **88**, 2428–2433 (1966).

91. Kiyota, Y., Nakamura, T., Muraki, K., Niwayama, H. & TarohInada, T. Behavior of Active and Inactive Boron in Si Produced by Vapor-Phase Doping during Subsequent Hydrogen Annealing. *Jpn. J. Appl. Phys.* **34**, 2981–2985 (1995).

92. Ma, J. *et al.* Simulation of a high-efficiency and low-jitter nanostructured silicon single-photon avalanche diode. *Optica* **2**, 974 (2015).

93. Inada, T. *et al.* Formation of ultrashallow $p^+$ layers in silicon by thermal diffusion of boron and by subsequent rapid thermal annealing. *Appl. Phys. Lett.* **58**, 1748–1750 (1991).

94. Maes, W., De Meyer, K. & Van Overstraeten, R. Impact ionization in silicon: A review and update. *Solid. State. Electron.* **33**, 705–718 (1990).

95. Massey, D. J., David, J. P. R. & Rees, G. J. Temperature Dependence of Impact Ionization in Submicrometer Silicon Devices. *IEEE Trans. Electron Devices* **53**, 2328–2334 (2006).

96. Xia, Z. *et al.* High-sensitivity silicon ultraviolet p+-i-n avalanche photodiode using ultra-shallow boron gradient doping. *Appl. Phys. Lett.* **111**, (2017).

97. Murakami, K., Wakabayashi, Y., Minami, K. & Esashi, M. Cryogenic dry etching

for high aspect ratio microstructures. in *[1993] Proceedings IEEE Micro Electro Mechanical Systems* 65–70 (IEEE). doi:10.1109/MEMSYS.1993.296953

98. Henderson, R. K., Richardson, J. & Grant, L. *Reduction of Band-to-band Tunneling in Deep-submicron CMOS Single Photon Avalanche Photodiodes*.

99. Sze, S. M. & Ng, K. K. *Physics of semiconductor devices*. (Wiley-Interscience, 2007).

100. David, J. P. R., Ghin, R., Plimmer, S. A., Rees, G. J. & Grey, R. Temperature dependence of avalanche breakdown in GaAs p-i-n diodes. in *HITEN 99. Third European Conference on High Temperature Electronics. (IEEE Cat. No.99EX372)* 187–190 (AEA Technol). doi:10.1109/HITEN.1999.827492

101. Schwartz, D. E., Charbon, E. & Shepard, K. L. A Single-Photon Avalanche Diode Array for Fluorescence Lifetime Imaging Microscopy. *IEEE J. Solid-State Circuits* **43**, 2546–2557 (2008).

102. Gulinatti, A. *et al.* Modeling photon detection efficiency and temporal response of single photon avalanche diodes. in (eds. Prochazka, I., Sobolewski, R. & Dusek, M.) **7355**, 73550X (International Society for Optics and Photonics, 2009).

103. Lee, M.-J., Sun, P. & Charbon, E. A first single-photon avalanche diode fabricated in standard SOI CMOS technology with a full characterization of the device. *Opt. Express* **23**, 13200 (2015).

104. Cova, S., Ghioni, M., Lacaita, A., Samori, C. & Zappa, F. Avalanche photodiodes and quenching circuits for single-photon detection. *Appl. Opt.* **35**, 1956 (1996).

105. Sun, P., Ishihara, R. & Charbon, E. Flexible Single-Photon Image Sensors. in *CMOS Circuits for Biological Sensing and Processing* 47–75 (Springer International Publishing, 2018). doi:10.1007/978-3-319-67723-1_3

106. Ohta, J., Tokuda, T., Sasagawa, K. & Noda, T. Implantable CMOS Biomedical Devices. *Sensors (Basel).* **9**, 9073–93 (2009).

107. Ohta, J. Implantable CMOS imaging devices for bio-medical applications. in *2011 IEEE 54th International Midwest Symposium on Circuits and Systems (MWSCAS)* 1–4 (IEEE, 2011). doi:10.1109/MWSCAS.2011.6026492

108. Ko, H. C. *et al.* A hemispherical electronic eye camera based on compressible silicon optoelectronics. *Nature* **454**, 748–753 (2008).

109. Zhang, K. *et al.* Origami silicon optoelectronics for hemispherical electronic eye systems. *Nat. Commun.* **8**, (2017).

110. Song, Y. M. *et al.* Digital cameras with designs inspired by the arthropod eye. *Nature* **497**, 95–99 (2013).

111. Palanker, D. *et al.* High-Resolution Opto-Electronic Retinal Prosthesis: Physical Limitations and Design. in *Artificial Sight* 255–277 (Springer New York). doi:10.1007/978-0-387-49331-2_14

112. Mathieson, K. *et al.* Photovoltaic retinal prosthesis with high pixel density. *Nat. Photonics* **6**, 391–397 (2012).

113. Jung, I. *et al.* Dynamically tunable hemispherical electronic eye camera system with adjustable zoom capability. *Proc. Natl. Acad. Sci. U. S. A.* **108**, 1788–93

(2011).

114. Ng, D. C. *et al.* Real time in vivo imaging and measurement of serine protease activity in the mouse hippocampus using a dedicated complementary metal-oxide semiconductor imaging device. *J. Neurosci. Methods* **156**, 23–30 (2006).

115. Wise, K. D. & Najafi, K. Microfabrication techniques for integrated sensors and microsystems. *Science* **254**, 1335–42 (1991).

116. Yoon, J. *et al.* Heterogeneously Integrated Optoelectronic Devices Enabled by Micro-Transfer Printing. *Adv. Opt. Mater.* **3**, 1313–1335 (2015).

117. Park, G. *et al.* Immunologic and Tissue Biocompatibility of Flexible/Stretchable Electronics and Optoelectronics. *Adv. Healthc. Mater.* **3**, 515–525 (2014).

118. Etienne Menard, † *et al.* Micro- and Nanopatterning Techniques for Organic Electronic and Optoelectronic Systems. (2007). doi:10.1021/CR050139Y

119. Peumans, P., Yakimov, A. & Forrest, S. R. Small molecular weight organic thin-film photodetectors and solar cells. *J. Appl. Phys.* **93**, 3693–3723 (2003).

120. Kim, R.-H. *et al.* Waterproof AlInGaP optoelectronics on stretchable substrates with applications in biomedicine and robotics. *Nat. Mater.* **9**, 929–937 (2010).

121. Yoon, J. *et al.* GaAs photovoltaics and optoelectronics using releasable multilayer epitaxial assemblies. *Nature* **465**, 329–333 (2010).

122. Rieke, F. & Baylor, D. A. Single-photon detection by rod cells of the retina. *Rev. Mod. Phys.* **70**, 1027–1036 (1998).

123. Becker, W., Bergmann, A., Biscotti, G. L. & Rueck, A. Advanced time-correlated

single photon counting techniques for spectroscopy and imaging in biomedical systems. in (eds. Neev, J., Schaffer, C. B. & Ostendorf, A.) **5340**, 104 (International Society for Optics and Photonics, 2004).

124. Zang, K. *et al.* Silicon single-photon avalanche diodes with nano-structured light trapping. *Nat. Commun.* **8**, 628 (2017).

125. Zhu, J. *et al.* Optical Absorption Enhancement in Amorphous Silicon Nanowire and Nanocone Arrays. *Nano Lett.* **9**, 279–282 (2009).

126. Ma, J. *et al.* Simulation of a high-efficiency and low-jitter nanostructured silicon single-photon avalanche diode. *Optica* **2**, 974 (2015).

127. Wang, Z. *et al.* Thin scintillators for ultrafast hard X-ray imaging. in (eds. Prochazka, I., Sobolewski, R. & James, R. B.) **9504**, 95040N (International Society for Optics and Photonics, 2015).

128. Kwon, S. Il *et al.* Development of small-animal PET prototype using silicon photomultiplier (SiPM): initial results of phantom and animal imaging studies. *J. Nucl. Med.* **52**, 572–9 (2011).

129. Becker, W. *et al.* <title>FRET measurements by TCSPC laser scanning microscopy</title> in (eds. Andersson-Engels, S. & Kaschke, M. F.) **4431**, 94–98 (International Society for Optics and Photonics, 2001).

130. Cova, S., Longoni, A., Andreoni, A. & Cubeddu, R. A semiconductor detector for measuring ultraweak fluorescence decays with 70 ps FWHM resolution. *IEEE J. Quantum Electron.* **19**, 630–634 (1983).

131. Pengfei Sun, Charbon, E. & Ishihara, R. A Flexible Ultrathin-Body Single-Photon Avalanche Diode With Dual-Side Illumination. *IEEE J. Sel. Top. Quantum Electron.* **20**, 276–283 (2014).

132. Sun, P., Ishihara, R. & Charbon, E. Flexible ultrathin-body single-photon avalanche diode sensors and CMOS integration. *Opt. Express* **24**, 3734 (2016).